Structural dynamics of solvated metal complexes with anisotropy-enhanced X-ray scattering

Biasin, Elisa

Publication date:
2016

Document Version
Publisher's PDF, also known as Version of record

Technical
University of
Denmark

Structural dynamics of solvated metal complexes with anisotropy-enhanced X-ray scattering

Elisa Biasin

PhD Thesis
October 2016

Academic Advisors:
Martin Meedom Nielsen
Kristoffer Haldrup

DTU Physics
Department of Physics

Technical University of Denmark
Department of Physics
Fysikvej, building 307,
2800 Kongens Lyngby, Denmark

Abstract

Transition metal complexes undergo photochemical and photophysical processes that can be exploited in applications such as solar energy conversion, catalysis, and water splitting. Understanding such processes involves the investigation of the photoinduced dynamics at the fundamental time scale of atomic motions. This thesis describes the use of time-resolved X-ray scattering at X-ray free electron lasers to study the photoinduced structural dynamics of solvated transition metal complexes at the femtosecond time scale.

First, the thesis describes the formalism necessary for the analysis of asymmetric scattering patterns arising from an aligned ensemble of molecules. The scattering signal is expanded in a sum of the zero-order (isotropic) and second-order (anisotropic) Legendre polynomials. Secondly, the thesis describes and applies methods to: correct raw measured anisotropic scattering patterns, especially from artefacts dependent on the X-ray source; extract isotropic and anisotropic difference scattering curves from the scattering patterns; quantitatively analyse the isotropic and anisotropic signals. Focus is given to the information gained from the anisotropic signal.

The first application of these methods gives insight into the ultrafast (< 3 ps) electronic and structural dynamics of $[Co(terpy)_2]^{2+}$ in water upon photoinduced spin state transition. Density Functional Theory calculations and Molecular Dynamics simulations are used to interpret the ultrafast elongation of the Co-N bonds, the vibrational coherences arising from Co-N stretching and decaying on a sub-picosecond time scale, the population kinetics, and the changes in the first solvation shell. From the anisotropic component of the signal, the transient response of the water molecules to the linearly polarized laser field is observed and provides an accurate estimate of the Instrument Response Func-

tion of the experiment.

As a second application of the aforementioned methods, the ultrafast (< 5 ps) ground state dynamics of $Pt_2(P_2O_5H_2)_4^{4-}$ (PtPOP) in water is investigated through side-by-side analysis of the isotropic and anisotropic scattering signals. Anisotropy-enhanced information facilitate the disentanglement of the different electronic and nuclear (inter- and intra-molecular) degrees of freedom involved in the dynamics of PtPOP.

Resumé

Overgangsmetalkomplekser gennemgår fotokemiske og fotofysiske processer der kan bruges til at konvertere solenergi, udføre katalyse og til vandsplitning. For at forstå disse processer kræver det at man studerer den fotoinducerede dynamik på atomar tidsskala. Denne afhandling beskriver brugen af tidsopløst Røntgenspredning, ved fri-elektron Røntgenlaserkilder, til at studere den fotoinducerede strukturelle dynamik af overgangsmetalkomplekser i opløsning, på femtosekundstidsskala.

Først og fremmest beskriver afhandlingen den formalisme der er nødvendig til at analysere asymmetriske spredningsmønstre der opstår fra molekyler med udvalgt orientering. Spredningssignalet ekspanderes i en sum af nulteordens (isotrop) og i andenordens (anisotrop) Legendrepolynomier. Dernæst beskriver afhandlingen de metoder der er blevet anvendt for: at korrigere de rå, målte, anisotrope spredningssignaler, især artefakter fra Røntgenkilden; at ekstraherede isotrope og anisotrope differenssignaler fra spredningsbillederne; kvantitativt at kunne analysere de isotrope og anisotrope signaler. Fokus lægger på den information der indeholdt i det anisotrope signal.

Den første anvendelse af disse metoder giver os en indsigt i den ultrahurtige (< 3 ps) elektroniske og strukturelle dynamik af vandopløst $[Co(terpy)_2]^{2+}$ efter en fotoinduceret spinovergang. Simuleringer med Density Functional Theory og Molecular Dynamics bliver brugt til at fortolke ultrahurtig forlængelse af Co-N bindingen, den vibrationelle kohærens der opstår som følge af Co-N strækket og det efterfølgende henfald på subpicosekundtidsskala, populationskinetik samt ændringer i første solvatiseringsskal. Fra den anisotrope komponent af signalet kan vi observere interaktionen mellem den lineært polariserede laser og den forbigående reaktion af vandmolekylerne hvilket giver os et nøjagtigt estimat af

eksperimentets Instrument Response Function.

Den anden anvendelse af ovennævnte metoder hat været at undersøge den ultrahurtige (< 5 ps) grundtilstandsdynamik af vandopløst $Pt_2(P_2O_5H_2)_4^{4-}$ (PtPOP) hvor det isotrope og anisotrope spredningssignal bliver analyseret side om side. Anisotro- piforstærket information gør det muligt at adskille de forskellige bidrag fra de elektroniske og nukleare frihedsgrader der lægger til grund for PtPOPs dynamik.

Acknowledgements

My PhD has been one of the most valuable experiences of my life. Throughout it, I have grown both professionally and personally, for the most part due to the wonderful people I met along the way.

I would first like to thank my supervisor, Martin M. Nielsen, for this PhD, the opportunities it gave me to conduct my research, and for being an exemplary and inspiring leader. Martin, I have always admired the clarity with which you communicate your immense knowledge and your judicious advice has always come when I most needed it. I would also like to thank my co-supervisor, Kristoffer Haldrup, for teaching me almost all I know about X-ray solution scattering, for guiding me patiently through my research, and while writing my first article. Thank you, Kreuff, also for your guidance in organizational and personal matters, and for your perseverance in promoting discussions, meetings, and the group atmosphere.

There are not enough words I can use to thank Tim B. van Driel, Kasper S. Kjær, Tobias Harlang and Asmus O. Dohn, who, by preceding me with their PhDs, have been excellent role models. Thank you for the knowledge and the time you have shared with me, and for the contagious passion you all have for your work. In particular: Tim, for dispensing your skills and your precious scripts. Kasper, for the scientific discussions and for teaching me experimental work at the beamline. Tobias, for proofreading and for your admirable work behaviour; for your friendship and for your multiple introductions to danish lifestyle. Asmus, for teaching me how to do MD simulations and how to eat with chopsticks, for discussions on solvation effects and on techno music, for being an amazing colleague and an amazing friend.

I would like to thank all the colleagues I have spent office hours and beam time with-it was hard work but also a lot of fun. I am grateful to Mads Laursen, for the support in stressful periods, and Frederik Beyer, for the proofreading and related discussions. I would also like to thank Morten Christensen, who made the PtPOP experiment possible, and probably my PhD by replying to that my first e-mail to the group fours years ago. Thank you for being the first one to believe in me. I am grateful to my colleagues at NEXMAP and the staff at DTU Physics, for providing an amazing environment for science and for the fun time we had together.

The collaboration with DTU Chemistry was greatly beneficial for my PhD. I would like to thank Klaus B. Møller and Niels E. Henriksen, for the insights on anisotropy and for the patience to answer my very basic questions. I would like to thank Mátyás Pápai, for the calculations on CoTERPY, and Gianluca Levi for those on PtPOP.

My gratitude goes to Kelly G. Gaffney and his group at the Pulse Institute, where I was lucky enough to spend five months of my PhD. Thank you, Kelly, for the opportunity to join your team, for your insight into photochemistry, for your suggestions on my projects and for always being the source of brilliant and inspiring conversations. A special thank you to Robert Hartsock, for sharing his knowledge, for his endless help in the chemical lab, for discussions over coffees about science and life. I would also like to thank Marco Reinhard and Zheng Sun for the transient absorption measurements and the IR measurements on CoTERPY. Eventhough they are not part of this thesis, they helped my understanding of the dynamics of the complex. Thank you to all the other friendly colleagues I met at Pulse, such as Adi Natan, and the people who helped my stay dealing with bureaucracy or giving me access to the lab and research facilities.

I would also like to thank collaborators from Lund, Budapest and Hamburg. In particular, I would like to thank György Vankó, for his insightful comments and encouragement with respect to the article, and Sophie E. Canton, for the CoTERPY experiment and for the scientific discussions we had together. Finally, this project would have not been possible without all the people that work at the facilities where we perform experiments. I would like to thank all of them and, in particular, the beamline scientists at XPP.

I would have not gone through this PhD without all the friends I met during these three years in Denmark, that have been essential for my personal serenity and balance. In particular I would like to thank Marijana, Elisa and Rasmus. A special thanks goes to you, Kristjan, for your support and your understanding and for the happy moments and the peace of mind you gave me in this last year of my PhD.

Finally, I would like to thank my italian friends and family. Allow me some words for them.
Vorrei ringraziare tutti gli amici italiani che ancora mi scrivono e mi vogliono bene, nonstante la mia decisione di trasferirmi nel freddo Nord. Il vostro supporto, anche se lontano, mi ha dato forza nei momenti difficili. Vorrei ringraziare la mia famiglia, in particolare i miei genitori, per aver appoggiato il mio PhD in Danimarca e sostenuto le mie aspirazioni. In particolare, il mio grazie speciale e la mia dedica vanno a te, mamma, perché hai sempre creduto nelle mie capacità e mi hai insegnato a non mollare mai.

Publications Included in This Work

Paper I

On the calculation of x-ray scattering signals from pairwise radial distribution functions
Asmus O. Dohn, Elisa Biasin, Kristoffer Haldrup, Martin M. Nielsen, Niels E. Henriksen and Klaus B. Møller
Journal of Physics B: Atomic, Molecular and Optical Physics **48** 244010 (2015)

Paper II

Disentangling detector data in XFEL studies of temporally resolved solution state chemistry
Tim Brandt van Driel, Kasper S. Kjær, Elisa Biasin, Kristoffer Haldrup, Henrik T. Lemke and Martin M. Nielsen
Faraday Discussions **177** 443-465 (2015)

Paper III

Femtosecond X-Ray Scattering Study of Ultrafast Photoinduced Structural Dynamics in Solvated [Co(terpy)2]2+
Elisa Biasin, Tim Brandt van Driel, Kasper S. Kjær, Asmus O. Dohn, Morten Christensen, Tobias Harlang, Pavel Chabera, Yizhu Liu, Jens Uhlig, Mátyás Pápai, Zoltán Németh, Robert Hartsock, Winnie Liang, Jianxin Zhang, Roberto Alonso-Mori, Matthieu Chollet, James M. Glownia, Silke Nelson, Dimosthe-

nis Sokaras, Tadesse A. Assefa, Alexander Britz, Andreas Galler, Wojciech Gawelda, Christian Bressler, Kelly J. Gaffney, Henrik T. Lemke, Klaus B. Møller, Martin M. Nielsen, Villy Sundström, György Vankó, Kenneth Wärnmark, Sophie E. Canton, Kristoffer Haldrup
Physical Review Letters **117** 013002 (2016)

Contributions to Publications

Paper I Scientific discussions, commenting on paper, validation of the results.

Paper II Scientific discussions, commenting on paper, validation of the results.

Paper III Main writer of paper, XDS esperiment, XDS data analysis, MD simulations.

Contents

Chapter 1

Introduction

Femtochemistry is the study of chemical reactions and related process at the femtosecond time scale, which is the time scale of atomic motions. Experiments resolving such motions often uses a pump-probe scheme: a femtosecond laser pulse triggers a photoreaction in an ensemble of molecules and a subsequent pulse probes the excited state dynamics as a function of the time delay in between the two pulses. Since all the molecules react synchronously to the femtosecond pump, microscopic information can be extracted from an ensemble of molecules. The observation of each of the elementary steps constituting the process of a chemical reaction, such as branching and formation of intermediates, is of fundamental importance to understand the reactivity of chemical compounds and the mechanism driving the outcome of the reaction.

Ahmed Zewail is considered the founder of femtochemistry and was awarded the the Nobel price in 1999 for his studies of transient states in chemical reactions with femtoseconds spectroscopy. His pioneering works utilized optical spectroscopy to study bond-breakage in small molecules in gas phase [1, 2]. Since then, many experimental technique have been adapted and/or have developed for ultrafast pump-probe studies. While optical spectroscopy gives information of the kinetics and the changes in energies of the electronic states, X-ray or electron probe pulses can provide direct insight in the photo-induced structural dynamics, since they probe directly the nuclear positions. The development of each probing techniques is of importance since it can allow the design of exper-

iments with greater information content, selectivity and sensitivity. This will further allow the study of more complex systems, with a greater general relevance in chemistry and biology. In particular, the general context of this work is related to the development of ultrafast X-ray methods, that have recently become available with the realization of X-ray free electron lasers (XFELs) light sources, which can deliver femtosecond X-ray pulses with high intensity and tunable energy [3].

A large majority of chemical and biological processes takes place in the liquid phase, where the solute-solvent interactions can significantly affect the reactions dynamics. The systems of interest in this work are thus molecules in solution, and, specifically, transition metal complexes with unique photochemical and photophysical properties. Applications range from solar energy conversion [4, 5] and photocatalysis [6, 7] to biology and medicine [8, 9]. In the last two decades, the use of time-resolved X-ray techniques, such as X-ray absorption and scattering, has revealed the structure of light-generated transient species for a wide range of inorganic molecules in solution [10, 11, 12, 13, 14, 15, 16, 17], with time resolution limited (mostly) by the pulse length of the X-ray pulse. Information regarding the photoinduced changes in molecular geometries can facilitate the understanding of the structure/function relation and thus allow for more efficient design of photochemical system. In particular, X-ray scattering arises directly from the all the inter-atomic distances of the sample, and can then reveal direct structural information of both the solute and the solvent and thus shed light on the the solute-solvent interplay [18]. X-ray scattering from solutions is commonly called X-ray diffuse scattering (XDS) to distinguish it from scattering from crystalline materials.

Fig. 1.1 shows a typical setup for time-resolved X-ray scattering experiments on liquid samples. Laser pump and X-ray probe pulses are focused on a thin liquid sheet, which is produced by circulating the sample through a nozzle. The two pulses are separated in time by a tunable delay and fresh sample is ensured for every pump-probe event. The diffuse X-ray scattering is collected on an two dimensional (2D) detector placed after the sample on the plane perpendicular to the propagation direction of the X-ray beam. Images collected before the arrival of the excitation pulse at the sample are subtracted from the images detected after the excitation event. In this way the unchanged background, dominated by the signal arising from the solvent, is removed and the so obtained difference scattering images contain information on the photoinduced structural changes in the sample. A standard procedure has been established so that 2D images are corrected for artefacts and then azimuthally integrated to create one dimensional (1D) difference scattering curves, which are then further analysed to extract quantitative structural information [19, 20]. The formalism to evaluate (time-resolved) X-ray scattering signals from chemical system randomly oriented in solution has been in derived in Paper I and it is based on pair radial distribution

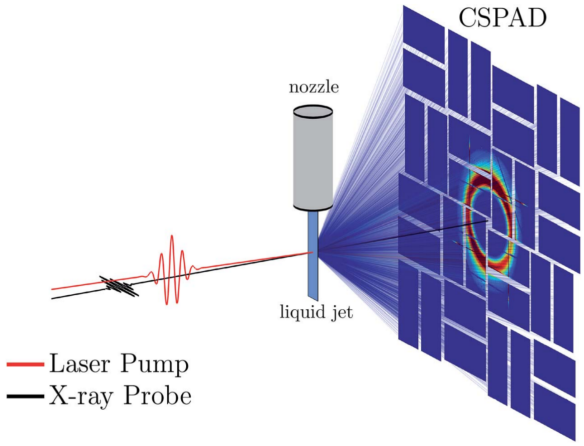

Figure 1.1: Setup for time-resolved XDS on liquid sample at the X-ray pump-probe (XPP) instrument at LCLS. Every X-ray pulse hitting the sample yields a scattering image on the the Cornell-SLAC pixel array detector (CSPAD). From Paper II.

functions (RDFs).

With the ultra-bright and ultra-short X-rays pulses available at XFELs, such as the Linac Coherent Light Source (LCLS) [21] in the USA or the SPring-8 Angstrom Compact free electron LAser (SACLA) [22] in Japan, time-resolved XDS can be utilized to monitor solute and solvent dynamics at the time scale of atomic motions. However, the implementation of time-resolved XDS at XFELs has not come without challenges. Only an handful of studies using this technique on liquid sample have been published [23, 16, 24, 25] since LCLS and SACLA became operational, in 2009 and 2011, respectively. One of the challenges is due to the stochastic nature of the Self-Amplified Spontaneous Emission (SASE) process characteristic of the XFEL sources [26], that leads to big pulse-to-pulse variations and over-time drifting. In this contest, Paper II describes how to correct for such fluctuations. Establishing a robust routine for the online and offline analysis of measurements at XFELs is an ongoing effort; and it is also important in view of the upcoming European XFEL and the SwissFEL, currently being built in Hamburg and in Switzerland, respectively. This work focuses on the analysis of time-resolved X-ray scattering data measured on solvated transition metal complexes at LCLS and discusses some of the challenges encountered in the data analysis. The obtained results prove that this technique at XFELs can be successfully used to track in real time the structural changes that occur during a (photo-induced) chemical reaction.

The improved time-resolution available at XFELs compared to synchrotron sources allows the observation of phenomena that have not previously been observed with time-resolved XDS. For instance, at synchrotron light sources, the $\sim$ 100 ps long X-ray pulses can monitor only thermally equilibrated molecular excited states. At XFELs, both vibrational and rotational molecular dynamics can be detected. With respect to the former, Paper III reports the observation, for the first time with time-resolved X-ray scattering, of femtoseconds coherent dynamics arising from the population of vibrationally hot electronic state after excitation of a solvated transition metal complex. With respect to the latter, 2D scattering patterns with an asymmetric intensity distribution can be observed on the time scale of the rotational correlation time of the solute [23, 27]. Such an effect is due a non-uniform distribution of orientations in the excited-state population because of the photoselection induced by the linearly polarized laser pulse. The theoretical foundations for understanding and interpreting such asymmetry-effects have been laid out in some detail over the past ten years [28, 29, 30]. However, only qualitative interpretation of anisotropic scattering data in solution state have been reported [31, 23]; in these studies the correlation time of the solute was extracted by looking at the decay of the asymmetry in the 2D scattering patterns. This thesis uses the formalism derived by Lorentz et al. [29] to extract the isotropic and anisotropic contribution from the 2D scattering patterns, as opposite of the standard azimuthal integration. Furthermore, it investigates whether the anisotropic difference scattering signal can deliver information beyond the orientation distribution of the molecular ensemble giving rise to the scattering signal.

1.1 Outline

Chapter 2 describes the formalism for the interpretation of anisotropic time-resolved X-ray scattering patterns from molecules in solution. The chapter further describes the transition metal complexes that have been investigated in this thesis and it introduces the observable of interest (which is the photoinduced dynamics of both solute and solvent).

Chapter 3 describes the process of correcting 2D scattering patterns from artefacts arising from the shot-to-shot fluctuations characteristic of XFEL sources. It describes the method for the extraction of both isotropic and anisotropic 1D difference scattering curves from the 2D patterns. Finally, it introduces the way to model such 1D signals.

Chapter 4 presents the analysis and the results of a time-resolved X-ray solution scattering experiment carried out at the LCLS facility. The experiment inves-

tigate the (photoinduced) femtosecond coherent dynamics of a Co complex in water. This chapter links to Paper III for additional details.

Chapter 5 presents the analysis of anisotropic scattering signals measured at LCLS upon photoexcitation of metal complexes in solution. The aim is to interpret such signals and extract quantitative information that can help the analysis of an XDS data set.

Chapter 6 collects the results and presents future goals and ambitions.

Chapter 2

Ultrafast time-resolved X-ray scattering on solvated molecules

This chapter provides the theoretical background for laser pump-X-ray probe experiments on molecules in solution and for the interpretation of the photoinduced dynamics in the sample.

2.1 Scattering from electrons, atoms, and molecules

The following section introduces some of the background theory of the interaction between X-rays and matter; in particular it describes how X-rays scatter with electrons, atoms and molecules. It is based on the classical picture given in [32].

X-ray beam

An X-ray beam can be described as a linearly polarised electromagnetic plane wave with an electric field having amplitude E_0, wavevector $\mathbf{k}$, angular frequency ω and a specific polarization. From a quantum mechanical point of view, the electromagnetic wave is quantized into photons, each having an energy $e_{ph} = \hbar\omega$ and momentum $\mathbf{p} = \hbar\mathbf{k}$, where $\hbar$ is the reduced Planck's constant.
The process exploited to investigate the structure of materials is the elastic scattering (Thomson scattering), in which the photon scatters in a random direction without altering its frequency or kinetic energy. It is described by the wavevector transfer $\mathbf{Q}$, usually expressed in units of Å^{-1},:

$$\mathbf{Q} = \mathbf{k} - \mathbf{k}' \tag{2.1}$$

where $\mathbf{k}$ and $\mathbf{k}'$ are the initial and final wavevectors of the photon respectively. Since $|\mathbf{k}| = |\mathbf{k}'|$, the difference between the two vectors results $|\mathbf{Q}| = 2|\mathbf{k}|\sin\theta$, where 2θ is usually referred to as the scattering angle.

Scattering from an electron

The Thomson scattering from a single electron can be visualized as an expanding spherical wave of photons oscillating in phase, with the electron at the origin. The modulus squared of the radiated field at a distant R from the source, and at an angle ψ with respect to the direction of propagation of the incident beam is:

$$|E_{rad}|^2 = \left(\frac{r_0^2}{R^2}\right)|E_0|^2 p(\psi) \tag{2.2}$$

where p depends on the polarization of the X-ray beam and r_0 is the Thomson scattering length (or alternatively the classical electron radius). The scattering signal is usually expressed as a differential cross-section $\frac{d\sigma}{d\Omega}$, i.e the number of photons arriving at the detector per second and per solid angle ($R^2 d\Omega$), normalized by the incident radiation flux ($\propto |E_0|^2$). In case of a single electron, it can be calculated from Eq. 2.2 as:

$$\frac{d\sigma}{d\Omega} = r_0^2 p(\psi) \tag{2.3}$$

An integrated over all possible directions leads to the Thomson scattering cross-section $\sigma_T = \frac{8\pi}{3} r_0^2$.

Scattering from an atom

If there are several electrons, the expanding spherical waves will interact causing constructive and destructive interference corresponding to the phase difference between the radiated fields. The atomic electrons can be viewed as a charge cloud surrounding the nucleus with a density $\rho(\mathbf{r})$. A volume element $d\mathbf{r}$ at $\mathbf{r}$ will contribute an amount $-r_0\rho(\mathbf{r})d\mathbf{r}$ with a phase factor $e^{i\mathbf{Qr}}$. The total scattering length of the atom can then be written as:

$$F_0(\mathbf{Q}) = -r_0 f_0(\mathbf{Q}) = -r_0 \int \rho(\mathbf{r}) e^{i\mathbf{Qr}} d\mathbf{r} \tag{2.4}$$

where f_0 is known as the atomic form factor. Thus the atomic from factor is connected to the density distribution of electrons in the sample through a Fourier transform. In the limit $\mathbf{Q} \to 0$ all of the different volume elements scatter in phase so that $f_0(\mathbf{Q} = 0) = Z$, the number of electrons in the atom. As $\mathbf{Q}$ increases from zero the different volume elements start to scatter out of phase and consequently $f_0(\mathbf{Q} \to \infty) = 0$. Since the intensity is proportional to the squared modulus of the radiated field, the intensity of the scattering of an atom is found as the absolute squared of the scattering amplitude: $I(\mathbf{Q}) = |F_0(\mathbf{Q})|^2$.

Scattering from a molecule

Following the same approach and assuming the Independent Atom Model (i.e. considering every atom as an isolated sphere of electron density), the coherent scattering from a molecule can then be found through:

$$F_{mol}(\mathbf{Q}) = -r_0 \sum_{\mathbf{r}_j} f_j(\mathbf{Q}) e^{i\mathbf{Qr}_j} \tag{2.5}$$

where the index j labels the different atoms in the molecule and f_j the atomic form factor of the j'th atom in the molecule. The squared molecular form factor specifies the signal for a molecular fixed geometry:

$$|F_{mol}(\mathbf{Q})|^2 = r_0^2 \sum_{i,j}^{N} f_i^*(\mathbf{Q}) f_j(\mathbf{Q}) e^{i\mathbf{Qr}_{ij}} \tag{2.6}$$

Scattering from an ensemble of molecules

With respect to X-ray liquid scattering, a thorough derivation of the differential-cross section can be found in [33]. Disregarding the finite duration and the

frequency distribution of the X-ray pulse, the scattering from an ensemble of molecules in solution can be expressed by weighting the scattering from a single molecule (Eq. 2.6) with the instantaneous distribution ρ of nuclear geometries, so that:

$$\frac{d\sigma}{d\Omega}(\mathbf{Q}) = \sigma_T \int d\mathbf{R}\rho(\mathbf{R})|F_{mol}(\mathbf{Q},\mathbf{R})|^2 \tag{2.7}$$

where $\mathbf{R}$ has dimensions $3N$ and describes the nuclear coordinates in the laboratory frame. $\rho(\mathbf{R})d\mathbf{R}$ expresses the probability of finding a molecule whose molecular geometry is in an infinitesimal volume $d\mathbf{R}$ around a nuclear geometry $\mathbf{R}$. Expressing $\rho(\mathbf{R})$ can be simplified by assuming uncoupling between the 3 translational, the 3 angular (rotational) and the ($3N$ - 6) internal (vibrational) degrees of freedom, as described further in the following section.

2.2 Anisotropic X-ray scattering

This section summarizes and expands the formalism derived by Lorentz *et al.* [29] on how to approach scattering patterns arising from an aligned ensemble of molecules. This was also based on work of Zewail *et al.* [34, 28] on electron diffraction. Exact solutions have been derived only under several (described below) assumptions and for specific molecular geometries.

2.2.1 Laser-induced alignment

In time-resolved X-ray scattering experiments, a linearly polarized laser pulse initiates some dynamics on the sample, which is subsequently recorded by an X-ray probe pulse arriving at different time delays after the pump event. If the laser pulse is ultra-short, the dynamic process is coherent among the millions of excited molecules in solution, and scattering can be used to retrieve structural changes occurring in the molecules after the excitation event. The molecules in solution are randomly oriented before the arrival of the laser pump. Since the laser pulse will preferentially excite the molecules with the transition dipole moment parallel to the laser polarization axis, the excited state population is created as an oriented ensemble. The anisotropy will then decay with the time scale of the rotational correlation time of the molecule in solution, that, for the inorganic molecules of interest, range in the 10-200 picoseconds interval [27, 23]. The photoselection process is illustrated in Fig. 2.1.

If the linearly polarized laser pulse interacts with a single transition dipole vector μ of the molecule, the distribution of the transition dipole vectors, immediately

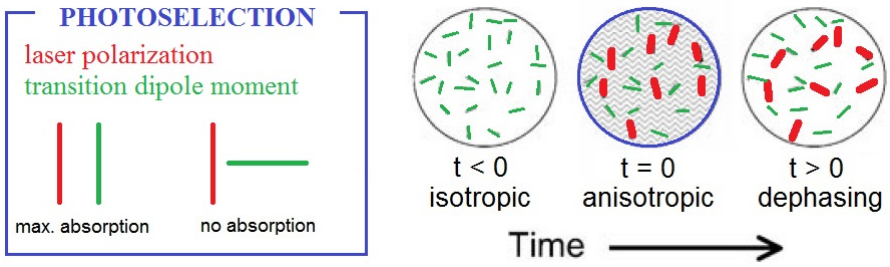

Figure 2.1: Illustration of the photoselection process. Before the arrival of the laser pump ($t < 0$), the molecules are randomly oriented in solution. The laser pulse excites preferentially the molecules with the transition dipole moments parallel to the laser polarization axis. Thus, at the excitation event ($t = 0$) the ensemble of excited state molecules is created with a cosine-square distribution with respect to the laser polarization axis. After the excitation event ($t > 0$) rotation of both the excited and unexcited populations causes dephasing of the alignment.

after the passage of the laser pulse, will display cylindrical symmetry about the direction of the laser polarization. This distribution can be expressed in an expansion of Legendre polynomials [28] in function only of the angle α between the laser polarization axis and the transition dipole moment:

$$D(\alpha, \eta) = \sum_{n=0}^{\infty} c_n P_n(\cos \alpha) \tag{2.8}$$

where α and η are spherical coordinates with respect to the laser polarization axis, P_n are Legendre polynomials and c_n are rotational coefficients.

This expression (Eq. 2.8) can be written in internal coordinates of the molecule and simplified by assuming that the molecule is a symmetric top with the transition dipole moment along the main axis of symmetry. As detailed in [34], the angular distribution of each inter-nuclear distance $\mathbf{r}_{ij}$ in the molecule with respect to the laser polarization axis can be expressed through the angle θ_{ij} between $\mathbf{r}_{ij}$ and the main axis of symmetry (i.e. the transition dipole moment) of the molecule. The different angles used in the formulae are illustrated in Fig. 2.2.

2.2.2 Scattering from an aligned ensemble of molecules

As seen in Eq. 2.7, the scattering from an ensemble of molecules in solution can be expressed by weighting the squared molecular form factor with the instantaneous distribution ρ of nuclear geometries. By assuming that rotational and vibrational degrees of freedom are uncoupled [29], the vibrational distribution can be disregarded (rigid-molecule limit) and the rotational part of the distribution expressed through $D(\alpha, \eta)$ in Eq. 2.8. If the integral in the ($3N$ - 6) vibrational degrees of freedom of the molecule is then neglected, the scattering from an ensemble of molecules aligned with respect to the laser polarization axis can be written as:

$$\frac{d\sigma}{d\Omega}(\mathbf{Q}) = \sigma_T \int_0^{2\pi} d\eta \int_0^{\pi} d\alpha \sin\alpha D(\alpha, \eta) |F_{mol}(\mathbf{Q}, \alpha, \eta)|^2. \tag{2.9}$$

As described by Lorentz et al. [29], the equation has an analytical solution of the form:

$$\frac{d\sigma}{d\Omega}(Q, \theta_q) = 2(2\pi)^2 \sigma_T \sum_n (-1)^{n/2} P_n(\cos\theta_q) S_n(Q) \tag{2.10}$$

where θ_q is the angle between the laser polarization axis and the Q vector (see Fig. 2.2), and

$$S_n(Q) = c_n \sum_{i,j}^{N} f_i(Q) f_j(Q) P_n(\cos\theta_{ij}) j_n(Q r_{ij}) \tag{2.11}$$

where j are the spherical Bessel functions. The rotational coefficients c_n describe the angular distribution and, if the angular distribution is unknown, they are additional fitting parameters or they have to be guessed. Note that Lorentz et al. [29] hide the c_n in the vibrational part of the density components.

By assuming one-photon absorption, the transition dipole moments will have a cosine-squared distribution about the laser polarization axis. Therefore, with respect to Eq. 2.8, the distribution will be proportional to $\cos^2\alpha$ and only the $n = 0$ and $n = 2$ terms contribute. The scattering signal (Eq. 2.10) is then:

$$\frac{d\sigma}{d\Omega}(Q, \cos\theta_q) \propto S_0(Q, t) - P_2(\cos\theta_q) S_2(Q, t) \tag{2.12}$$

where S_0 is recognized as the Debye formula for isotropic ensembles:

$$S_0(Q) = c_0 \sum_{i,j}^{N} f_i(Q) f_j(Q) \frac{sin(Q r_{ij})}{Q r_{ij}} \tag{2.13}$$

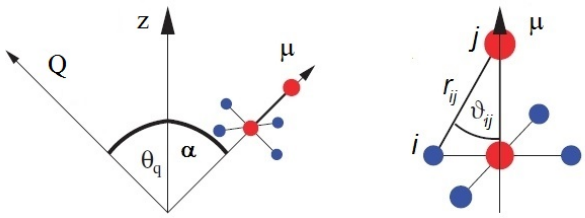

Figure 2.2: (left) Angles defined in the laboratory frame. θ_q is the angle between the laser polarization axis (z) and the scattering vector Q. α is the angle between z and the transition dipole of the molecule μ. (right) Angles in the molecular-fixed frame. θ_{ij} is the angle between the internuclear distance r_{ij} and the transition dipole of the molecule. Adapted from [29].

while S_2 contains information about the orientation of the single bonds r_{ij} with respect to the transition dipole moment of the molecule:

$$S_2(Q) = c_2 \sum_{i,j}^{N} f_i(Q) f_j(Q) P_2(\cos\theta_{ij}) j_2(Q r_{ij}). \tag{2.14}$$

While S_0 and S_2 depends only on internal coordinate of the molecule, $P_2(\cos\theta_q)$ in Eq. 2.12 depends on experimental parameters and it is responsible, as detailed in Section 2.4, for the anisotropic distribution of the scattering signal on the detector surface.

2.2.3 Rotational coefficients

A normalization on the unit sphere of the laser-induced distribution in Eq. 2.8 can be written as:

$$f^s = \frac{1}{4\pi} \int_0^{2\pi} \int_0^{\pi} D^s(\alpha, \eta) \sin\alpha d\alpha d\eta \tag{2.15}$$

where f^s is the fractional population of the oriented molecular species s immediately after the excitation event. If the ensemble is isotropic, only the $n = 0$ term will contribute:

$$f^s = \frac{1}{4\pi} \int_0^{2\pi} \int_0^{\pi} c_0^s P_0(\cos\alpha) \sin\alpha d\alpha d\eta. \tag{2.16}$$

Given that $P_0(x) = 1$, the solution of Eq. 2.16 yields $c_0^s = f^s$.

In case of a cosine-squared distribution:

$$f^s = \frac{1}{4\pi}\int_0^{2\pi}\int_0^{\pi}[c_0^s + c_2^s P_2(\cos\alpha)]\sin\alpha d\alpha d\eta. \tag{2.17}$$

Given that $P_2(x) = -\frac{1}{2}(1-3x^2)$, Eq. 2.17 is solved by $c_2^s = 2c_0^s = 2f^s$, as can be calculated considering $\int \cos^2 x \sin x = -\frac{1}{3}\cos^3 x + c$. The $c_2 = 2c_0$ relation is used throughout this thesis and defines the relative magnitude of the isotropic and anisotropic contributions immediately after the excitation event.

2.3 Difference scattering signal

In typical time-resolved X-ray scattering experiments, the concentration of the sample is typically 10-100 mM: there are thousands of solvent molecules per solute molecule and the scattering signal is dominated by the scattering from the solvent. Therefore, the analysis of static X-ray scattering measurements is challenging when investigating the structure of a dilute (poly-atomic) solute, especially if the accessible Q range is limited. However, the sensitivity to the solute is enhanced when constructing the difference scattering signal.

The difference scattering signal is constructed by subtracting patterns collected without photoexciting the sample from patterns collected after photoexcitation. Since the unchanging contribution (such as inelastic scattering) cancel out, the difference signal that arises from the changes in the solvent after laser excitation is typically of the same magnitude as the difference signal arising from the changes in the solute (1% - 0.1% of the total scattering signal) [10, 19]. Through analysis of the difference signal, time-resolved X-ray scattering has been successfully used to characterize the (photoinduced) structural dynamics of inorganic molecules in solution [12, 14, 15].

Starting from Eq. 2.12, the difference scattering signal can be calculated as [29]:

$$\Delta\frac{d\sigma}{d\Omega}(Q,\cos\theta_q) \propto \Delta S_0(Q) - P_2(\cos\theta_q)\Delta S_2(Q) \tag{2.18}$$

where $\Delta S_0(Q)$ and $\Delta S_2(Q)$ are the isotropic and anisotropic difference scattering signal, respectively.

As detailed in Appendix A, if only two species, the ground state (gs) and the excited state (es) of the molecule, contribute to the scattering signal, ΔS_0 can be calculated as:

$$\Delta S_0(Q) = S_0^{es}(Q) - S_0^{gs}(Q) \tag{2.19}$$

where S_0^{gs} and S_0^{es} are the isotropic scattering signals arising from the ground state and the excited state species, respectively, and can be calculated through Eq. 2.13. Similarly, ΔS_2 can be calculated as:

$$\Delta S_2(Q) = S_2^{es}(Q) - S_2^{gs}(Q) \tag{2.20}$$

while S_2^{gs} and S_2^{es} are the anisotropic scattering signals arising from the ground and the excited state species, respectively, and can be calculated through Eq. 2.14.

2.4 Anisotropic difference scattering patterns

This section utilizes the formalism introduced so far to project the isotropic and anisotropic scattering signal on the detector surface, given the standard experimental setup of time-resolved X-ray scattering experiments.

The formalism seen so far can be used to simulate the scattering from a fictitious diatomic platinum molecule. The transition dipole is set along the Pt-Pt axis and the molecule undergoes contraction of the Pt-Pt distance (d_{Pt-Pt}) when going from the ground state ($d_{Pt-Pt} = 3$ Å) to the excited state ($d_{Pt-Pt} = 2$ Å). Fig. 2.3(a) shows the calculated isotropic scattering S_0 (through Eq. 2.13) for both the ground-state and the excited-state and the difference between them: $\Delta S_0 = S_0^{es} - S_0^{gs}$. Similarly, Fig. 2.3(b) shows the calculated isotropic scattering S_2 (through Eq. 2.14) for both ground-state and excited-state and $\Delta S_2 = S_2^{es} - S_2^{gs}$. In the calculation, a cosine-squared distribution is assumed and, as detailed above, $c_2 = 2c_0$.

As introduced before, while both the S_0 and S_2 curves depends only on the internal coordinate of the molecule, $P_2(\cos\theta_q)$ in Eq. 2.18 depends on experimental parameters. The experimental setup needs then to be taken into account to project the scattering signal on the detector surface. $\cos\theta_q$, the angle between the Q vector and the laser polarization axis, can be expressed as a function of the angles δ, θ and ϕ, as they are defined in Fig. 2.4:

$$\cos\theta_q = \sin\theta\cos\delta - \cos\theta\cos\phi\sin\delta \tag{2.21}$$

As seen in chapter 1, in XDS experiments the scattered X-rays are collected by a 2D detector placed after the sample, perpendicular to the direction of propagation of the X-ray beam (x axis). The direction of propagation of the laser beam depends on the experimental setup and the available pathway, but, in liquid experiment, it is usually almost collinear to the X-ray beam, with the laser polarization axis being in the zy plane. In this configuration $\delta = 0$, and Eq. 2.21 simplifies as:

$$\cos\theta_q = -\cos\theta\cos\phi \tag{2.22}$$

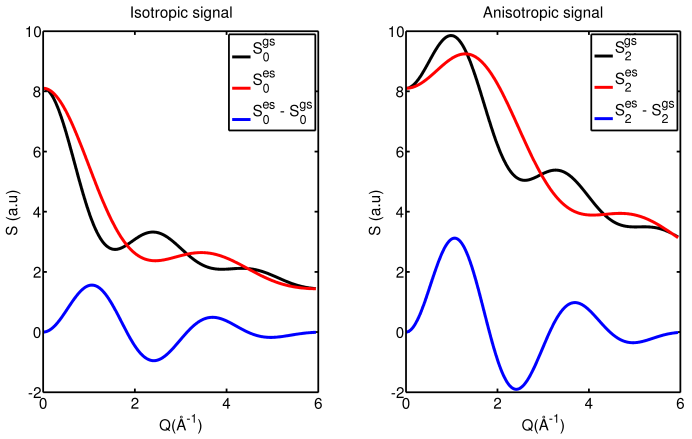

Figure 2.3: Calculated isotropic (left) and anisotropic (right) scattering curves for a Pt-Pt molecule with a cosine-square distribution of the Pt-Pt bond. In the ground-state species (gs, the black line) $d_{Pt-Pt} = 3$ Å while in excited-state species (es, the red line) $d_{Pt-Pt} = 2$ Å. The blue line shows the difference in between the scattering from the two species.

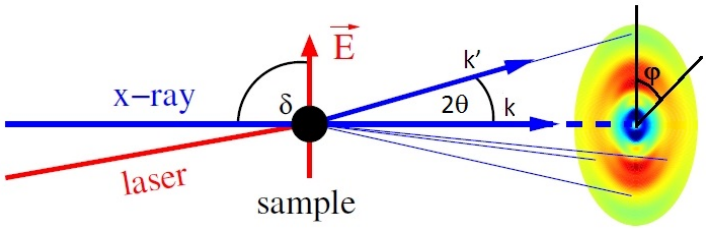

Figure 2.4: Experimental setup for a standard time-resolved XDS experiment. δ is the angle between the direction of propagation of the X-ray beam and the laser polarization axis $\vec{E}$; θ is half on the scattering angle; ϕ is the angle between the projection of the laser polarization and the Q vector on the detector surface.

where ϕ is the azimuthal angle on the detector, with $\phi = 0$ along the direction of the laser polarization axis, and θ is half of the scattering angle. If the laser is vertically polarized (thus $\phi = 0$ along the z axis), $P_2(\cos\theta_q)$ is mapped onto the detector surface as in Fig. 2.5(a).

Fig. 2.5(b) shows the difference scattering signal from a cosine-square distribution of Pt-Pt distances that contract 1 Å after excitation, as introduced before.

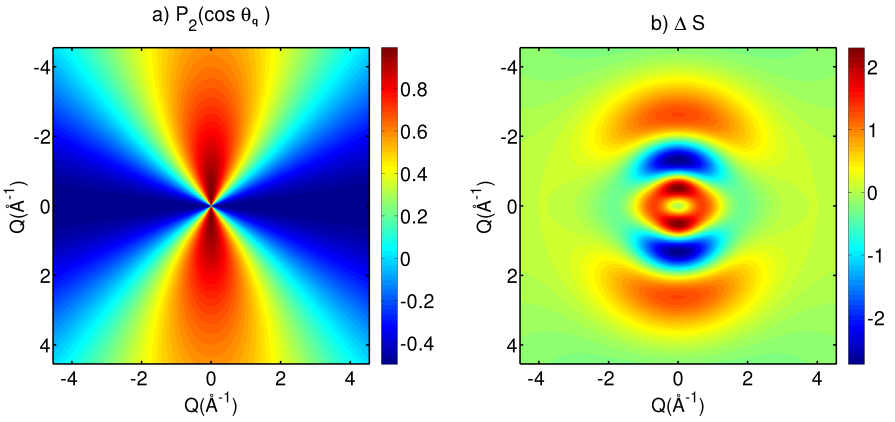

Figure 2.5: **(a)** P_2 mapped on the detector surface. $P_2(\cos\theta_q) = -\frac{1}{2}(3cos^2\theta_q - 1)$, with $\cos\theta_q$ as in Eq. 2.22. The laser polarization axis is along the vertical direction. **(b)** Anisotropic difference scattering pattern ($\Delta S_0 - P_2\Delta S_2$) from the contraction of a Pt-Pt molecule with a cosine-square distribution of Pt-Pt distances with respect to the direction of the laser polarization axis (vertical), as explained in the main text and in Fig. 2.3.

The total difference scattering signal ($\Delta S = \Delta S_0 + P_2\Delta S_2$) displays an asymmetric distribution on the detector surface due to the modulation given by the P_2 function (Fig. 2.5(a)).

The isotropic and anisotropic scattering signals can be extracted from measured anisotropic 2D patterns by exploiting the linear relation (Eq. 2.18) between the scattered intensity on the detector and P_2, for a given value of Q. This is the subject of Chapter 3.

As a final remark and as introduced in chapter 1, is is noted that anisotropic scattering patterns have been observed previously. At the Advanced Photon Source synchrotron, anisotropic X-ray scattering patterns were measured for transiently aligned protein molecules in solution and a $\sim$ 15 ns rotational time for myoglobin was extracted [31]. At SACLA, anisotropic femtosecond X-ray solution scattering was measured for a gold trimer complex in solution, and the rotational correlation time for the molecule was found $\sim$ 13 ps [23]. In these studies, the rotational correlation time of the solute has been extracted by looking at the decay of the difference between the signal recorded along two different cuts on the detector surface: one perpendicular and one parallel with respect to the laser polarization axis. Differently from these previous studies, one of the main goal of this thesis is the quantitative extraction and analysis of

the anisotropic scattering.

2.5 Solute and solvent dynamics

This section introduces the photoinduced dynamics for molecules in solution and the (structural and thermodynamic) changes in the sample that give rise to the difference scattering signal.

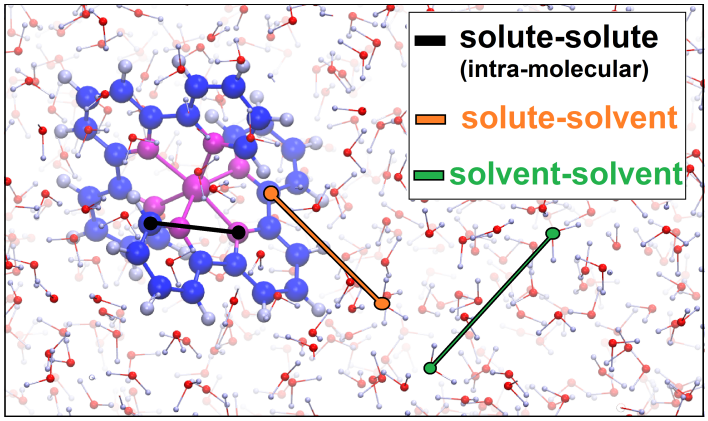

Figure 2.6: Illustration of the internuclear distances contributing to the global scattering signal arising from a low-concentrated solution. In the picture, the solute molecule is $[Co(terpy)_2]^{2+}$ and the solvent is water.

Scattering is a global probe, meaning that it returns information about the structure of the entire sample. All the internuclear distances of the sample contributing to the scattering signal are illustrated in Fig. 2.6. They can be divided in three groups:

- The solute-solute distances, as for a single molecule in gas phase. Given the low concentration (10-100 mM), the distance between different solute molecules is big enough to neglect the signal derived from the interference between them.
- The solute-solvent distances, the distribution of which describes the packing of the solvent molecules around the solute structure.
- The solvent-solvent distances, which describe the properties of the bulk solvent.

Following the above division of the sample internuclear distances, the difference scattering signal arises from three contributions: the changes in the structure of the solute, the changes in the solute-solvent distances (which lead to a scattering contribution which is referred to as cage term) and the changes in the solvent-solvent distances. The difference scattering signal at a specific time point can then be modelled as [19, 20, 10]:

$$\Delta S(Q) = \Delta S_{\text{solute}}(Q) + \Delta S_{\text{cage}}(Q) + \Delta S_{\text{solvent}}(Q). \tag{2.23}$$

How to model each of these contributions is described in chapter 3. In the following, a brief overview of the overall sample dynamics is presented.

Solute dynamics

Under the the Born-Oppenheimer approximation, which says that in a molecule the nuclei are essentially stationary compared to the electrons, the electronic configurations of a molecule can be represented as potential energy surfaces (PESs), where the potential energy is a function of the nuclear coordinates. Vibrational levels are associated with each electronic state. The electronic states of a molecule and the transitions between them can be illustrated through a Frank-Condon diagram, as in Fig. 2.7. According to the Franck- Condon principle, the configuration of the nuclei is practically frozen during the interaction with an optical field. The transitions that give rise to the absorption spectrum of a molecule take place between the ground electronic state of the molecule and an higher (excited) electronic state. After such a transition, which occurs in 10^{-15} s, internal conversion (a non-radiative transition between two electronic state of the same multiplicity) leads the excited molecule towards the lowest excited electronic state of the same multiplicity. From this state, the system can relax to the ground state through internal conversion or fluorescence (the latter being a radiative transition and usually more efficient than the former), or can undergo intersystem crossing (a non-radiative transition) to a state of different multiplicity. From such a state, the system can decay back to the ground state through radiative (phosphorescence) or non-radiative (the energy is transferred to the solvent) decay.

In Fig. 2.7(a) the ground state is labelled as a singlet, as for a molecule with full electron shells. If there are no unpaired electrons, the total spin S for the system is S=0 and the multiplicity of the system (the number of possible distinct values for the spin-angular momentum vector, calculated as 2S+1) is 1 (only one state exists). If the system has one unpaired electron: S = 1/2 and the multiplicity is 2 (doublet); if there are two unpaired electrons: S=1 and the multiplicity is 3 (triplet).

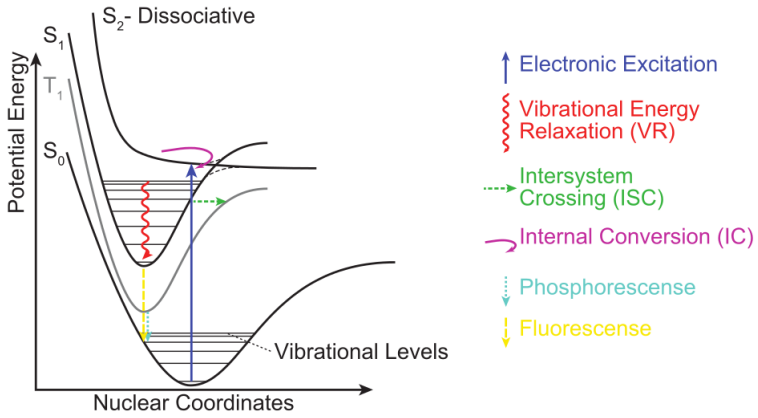

Figure 2.7: Diagram that illustrates, according to the Frank-Condon principle, some of the different electronic states of a molecule and the possible transitions between them. From [35].

After a transition, the system is usually on a vibrational level higher in energy than that at the minimum of the potential. The excess energy of the excitation is dissipated by non-radiative dynamic processes, such as: internal vibrational relaxation (IVR), when the energy dissipates to other intra-molecular degrees of freedom; and vibrational cooling (VC), when the energy is dissipated to the solvent. It has been reported that intermolecular energy transfer from the hot molecule to the surrounding solvent can start before IVR is completed [36, 37]. The time-scale of the vibrational relaxation usually ranges from 10^{-14} to 10^{-12}s, depending on the solvent properties [37]. The observation of vibrational coherences with X-ray scattering is therefore only possible at XFELs.

The rotational coherence for the molecules of interest in this work takes tens of picoseconds [23, 27]. Therefore, the anisotropy associated with the transient molecular alignment persists on time scale accessible at XFELs [23].

Solvent dynamics

Following the same Frank-Condon principle as above, the geometric arrangement and the orientation of the solvent molecules in the first solvation shell right after the excitation still correspond to the equilibrium configuration in the ground state. Following the attosecond-scale changes in the electron density dis-

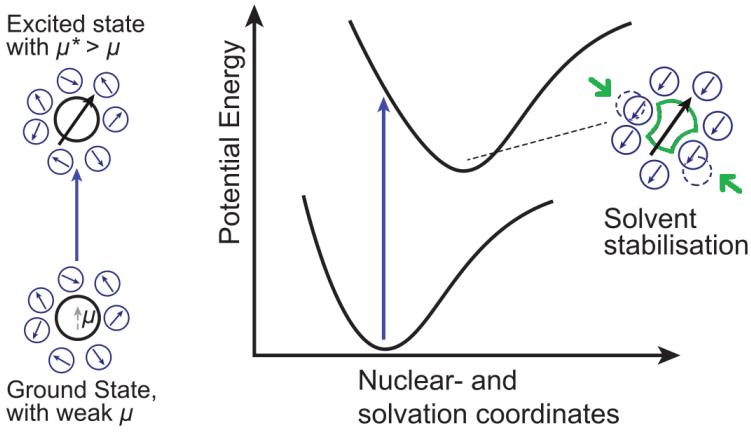

Figure 2.8: Illustration of solvation dynamics following electronic excitation of a molecule in a solution. The solvent responds to the change in dipole of the molecule. Furthermore, the solute-solvent distances are also affected by the changes in the structure of the solute molecule (such changes are represented in green). Adapted from [35].

tribution of the solute upon excitation, the solvent molecules reorganize so that the solvation energy (the amount of energy associated with dissolving a solute in a solvent) in the excited state can be lowered. This process is illustrated in Fig. 2.8.

The reorganization of the solvent molecules involve both polar (or dielectric) processes and non polar processes [36, 38]. These processes are both represented in Fig. 2.8 and described as follows. Dielectric processes mainly involve a rotation of the solvent molecules, which adapt the direction of their dipole to the change in charge distribution of the solute. Non polar processes involve centre-of-mass motions of the molecules and are connected to a change of shape and size of the solvent cavity that accommodate the solute molecule.

Solvent relaxation occur on multiple time scales. Within the first hundred femtoseconds after photoexcitation, the first solvation shell undergoes the so-called inertial (or underdamped) response [36], meaning that the solvent molecule have some freedom to undergo motions governed by their dynamics before the coupling with other intra- and inter-degrees of freedom occurs [39]. After the dephasing of such dynamics, a slower component in the solvent relaxation involves diffusive motions (such as large amplitude reorientation and translation of solvent molecules) [40].

With respect to the neat solvent, the interaction between the dipole (or induced-dipole) of the solvent molecules with the linearly polarized field of the laser pump causes the molecule to rotate into a position that minimizes the energy of the dipole in the electric field. This drives vibrational and rotational dynamics in the bulk solvent, similarly to the ultrafast response induced by a change in charge distribution of a solute molecule [41]. The response to the external electric field can be measured with techniques such as the optical Kerr effect and have been reported to occur in tens to hundreds of femtoseconds [42, 41].

Finally, once all the excess energy has been dissipated to the solvent and transformed in roto-vibrational modes of the solvent molecules, a new equilibrium is found and it can be described through thermodynamic properties. Thermalization of the solvent after an 'instantaneous' deposition of heat from a dye has been found to happen on two different time scales: an initial increase in temperature at constant volume happening in the 1-100 ps time timescale, followed by a density increase which is completed on a μs time scale [43, 44]. As further described in Section 3.4, the scattering signal arising from these changes in the bulk solvent can be measured in dye-solvent dedicated experiments and then be directly included in the analysis of any XDS data set.

2.6 Systems of interest

This section introduces the transition metal complexes investigated in this thesis and the time-resolved XDS experiments performed at LCLS on these systems.

2.6.1 [Co(terpy)2]2+

$[Co(terpy)_2]^{2+}$ (terpy = 2,2':6', 2"-terpyridine) was one of the first cobalt(II) spin-crossover (SCO) complex reported in literature (in the early 1960s) [45]. SCO compounds can undergo spin-state transition (SST) driven, for instance, by temperature increase, excitation by light or high magnetic fields. Their unique magnetic and structural properties can be exploited in several applications, such as the design of memory and spintronic devices [46, 47, 48].

The molecular structure of $[Co(terpy)_2]^{2+}$ is illustrated in Fig. 2.9. A central Co atom coordinates to two terpyridine ligands through six N atoms. As observed in crystallographic studies, the compound is compressed in the LS state (short axial and long equatorial Co-N bonds) due mostly to the geometrical constraints of the coordinating tridentate ligands. A pseudo Jahn-Teller effect

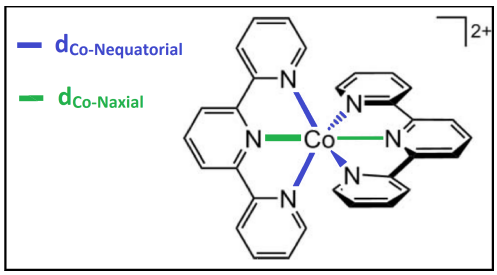

Figure 2.9: Molecular structure of $[Co(terpy)_2]^{2+}$. The axial and the equatorial Co-N bonds are represented in green and blue, respectively. From Paper III.

can also affect the LS state, so that one ligand is closer to the Co-center than the other [49, 50]. The LS $\rightarrow$ HS transition is accompanied by changes of the metal-to-ligand bond lengths [51]. The single-crystal studies report that the compound change structure anisotropically upon SST: the axial metal-to-ligand bond length increases by 0.21 Å, the equatorial one by 0.07 Å [52]. This is due to the transfer of one electron from the bonding t_{2g} to the anti-bonding e_g^* orbital. DFT calculations on gas-phase agree on the anisotropic expansion of $[Co(terpy)_2]^{2+}$ upon the spin change [50]. A schematic illustration of the changes in electronic and structural configuration upon SST in the compound is given in Fig. 2.10.

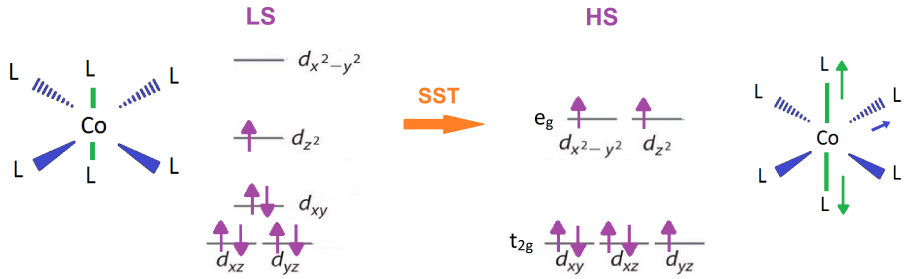

Figure 2.10: Schematic representation of the *d*-orbitals electronic configuration of the LS and HS state of $[Co(terpy)_2]^{2+}$, and schematic representation of the structural changes caused by the SST transition.

Very few studies have been published on $[Co(terpy)_2]^{2+}$ in solution. In general Co(II) complexes have received less attention than their Fe(II) analogue. In Fe(II) and Fe(III) SCO systems, the ground state is of singlet multiplicity and

the lowest excited metal-centered (MC) state is usually a quintet state, thus the total change in spin is $\Delta S = 2$. In Co(II) complexes, the SST yield a change in spin of $\Delta S = 1$ (from double to quartet). This leads to smaller energy difference between the LS and the HS state and thus to smaller structural changes and faster dynamics compare to Fe systems [53]. The dynamics of Fe(II) and Fe(III) complexes in solution upon photoinduced SST have been extensively investigated in last decade [51, 54, 55, 56, 17, 57, 16]. On the contrary, very little information can be found in the literature about the dynamics of Co(II) compounds. In particular, before Paper III was published, the HS $\rightarrow$ LS relaxation time of $[Co(terpy)_2]^{2+}$ was only known to be less than 2 ns [58].

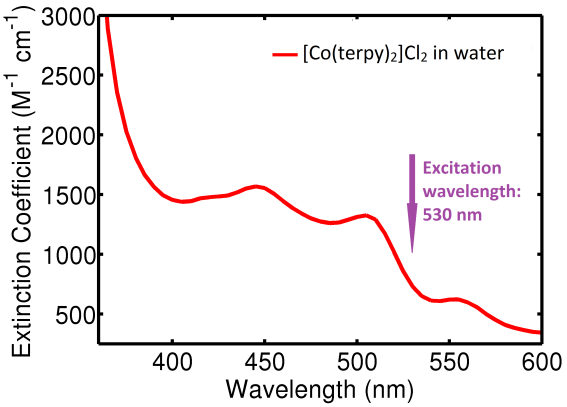

Figure 2.11: Absorption spectrum of $[Co(terpy)_2]^{2+}$ in water at room temperature. From Paper III.

[Co(terpy)2]2+ experiment

The time-resolved X-ray scattering experiment on $[Co(terpy)_2]^{2+}$ in water was conducted at the XPP instrument at LCLS to investigate the ultrafast (< 3 ps) dynamics upon photoinduced SST. Relevant parameters of the experiment are reported in Table 2.1.

Fig. 2.11 shows the absorption spectrum of the sample at room temperature. Kremer *et al.* [59] indicate a ground state with predominant LS character for $[Co(terpy)_2]^{2+}$ in solution. The peaks visible in the 430-560 nm range have been assigned to metal-to-ligand charge transfer (MLCT) transition from the LS state. In the experiment the excitation wavelength was 530 nm. From the MLCT state, the HS state is expected to be quickly populated [53].

	[Co(terpy)2]2+ exp.	PtPOP exp.
$\lambda_{excitation}$ (nm)	530(8)	395(5)
Sample concentration (mM)	20	80
Jet thickness (μm)	100	30
X-ray energy (KeV)	8.3	9.5
Laser pulse length (fs)	70	70
X-ray pulse length (fs)	30	30
Q-range ($Å^{-1}$)	0.5 - 3.5	0.5 - 4
Laser fluency (J cm^{-3})	0.26	0.03

Table 2.1: Experimental parameters of the time-resolved XDS experiments conducted at XPP to study the photoinduced dynamics of $[Co(terpy)_2]^{2+}$ and PtPOP.

2.6.2 PtPOP

The tetrakis-μ-pyrophosphitodiplatinate(II) ion $[Pt_2(P_2O_5H_2)_4^{4-}$, PtPOP] is a square-planar platinum(II) complex consisting of a biplanar Pt-Pt pair held together by four pyrophosphito ligands. The molecular structure is shown in Fig.2.12(a). The compound was first synthesized in 1977 and has been object of a vast amount of studies, due to its characteristic photophysical properties and activity as a photocatalyst [60]. In the last decades PtPOP has became a model compound for time-resolved X-ray studies, due to its high scattering power, its long lifetime, and its high symmetry, which enhance the effective signal [14].

Fig. 2.12(b) shows the absorption and emission spectra of the compound in aqueous solution. Crystallographic studies have assigned the strong absorption band at 370 nm to the singlet-to-singlet ($1A_{1g} \rightarrow 1A_{2u}$) transition with polarization along the Pt-Pt distance. The absorption peak at 450 nm corresponds to a singlet-to-triplet ($1A_{1g} \rightarrow 3A_{2u}$) transition with polarization perpendicular to the Pt-Pt bond. The assignment of other electronic transitions can be found in Fig. 2.12(d). Low temperature spectra of PtPOP single crystals display a vibronic progression in the order of 150 cm^{-1} (T = 0.22 ps) of both the 370 nm and the 450 nm peaks [63]. The similarity of the bandwidth and excited state vibrational frequencies implies that the singlet and triplet state PESs are very similar, which accordingly should imply structural similarities of these excited states. The T = 0.22 ps progression was assigned to the excited state Pt-Pt stretch [63].

The emission spectrum of PtPOP (Fig. 2.12(b)) is dominated by a strong emission band at 514 nm, with a weaker band at 403 nm. The 514 nm emission

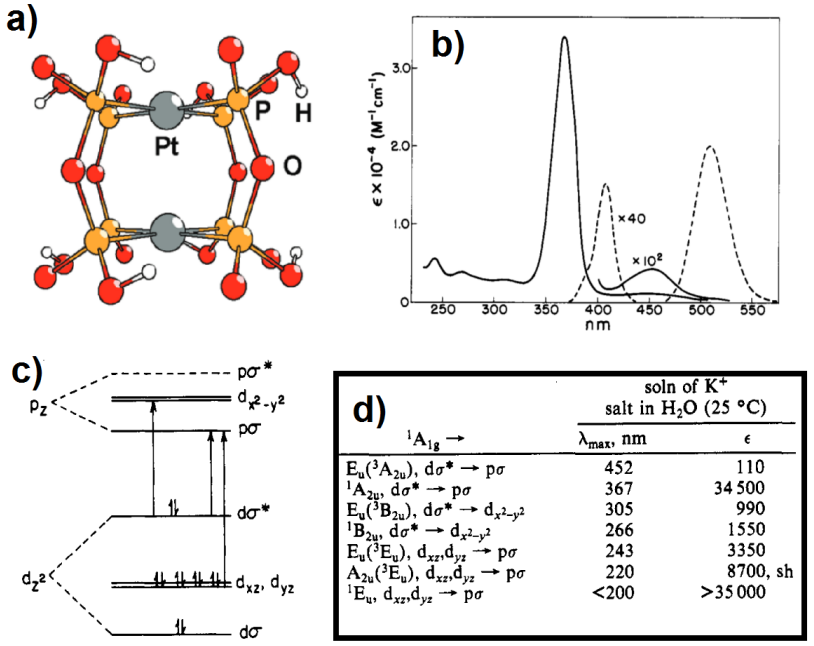

d)

$^1A_{1g} \rightarrow$	soln of K^+ salt in H_2O (25 °C) λ_{max}, nm	ϵ
$E_u(^3A_{2u})$, $d\sigma^* \rightarrow p\sigma$	452	110
$^1A_{2u}$, $d\sigma^* \rightarrow p\sigma$	367	34 500
$E_u(^3B_{2u})$, $d\sigma^* \rightarrow d_{x^2-y^2}$	305	990
$^1B_{2u}$, $d\sigma^* \rightarrow d_{x^2-y^2}$	266	1550
$E_u(^3E_u)$, d_{xz},$d_{yz} \rightarrow p\sigma$	243	3350
$A_{2u}(^3E_u)$, d_{xz},$d_{yz} \rightarrow p\sigma$	220	8700, sh
^1E_u, d_{xz},$d_{yz} \rightarrow p\sigma$	<200	>35 000

Figure 2.12: **a)** Molecular structure of PtPOP. From [61]. **b)** Absorption (continuous line) and emission (dashed line) of aqueous PtPOP. From [62]. **c)** Molecular orbital diagram and electronic electronic transitions of Pt-POP. From [63]. **d)** Assignment of the electronic transition of the absorption of PtPOP in aqueous solution in the visible spectrum. From [63].

has been assigned to the phosphorescence from the triplet and, in aqueous solution at room temperature, its lifetime has been reported to be in the ~ 10 μs range. The 403 nm emission band has been assigned to fluorescence with a $\sim$ 10 ps lifetime [64]. Low temperature phosphorescence and fluorescence spectra display a 118 cm^{-1} (T = 0.28 ps) progression. The vibronic fine structure of emission spectra generally provides information on the spacing between vibrational levels in the ground state, since this is the state reached in the electronic transition involved. Since the polarization is parallel to the Pt-Pt axis, the 118 cm^{-1} progression has been attributed to the Pt-Pt stretch.

As shown in the molecular orbital (MO) diagram in Fig. 2.12(c), the transition between the highest energy occupied MO (HOMO) and the lowest energy unoccupied MO (LUMO) involves the promotion of an electron from the antibonding

dσ^* to the bonding pσ orbital and should thus entail some degree of contraction of the Pt-Pt bond. Christensen *et al.* investigated the structure of the triplet excited state of PtPOP in water with time-resolved XDS and obtained a Pt-Pt contraction of 0.24 ± 0.06 Å [14] with respect to the ground state of the molecule. Van der Veen *et al.* observed a 0.31 ± 0.05 Å Pt-Pt contraction upon excitation of the complex in ethanol, with X-ray absorption spectroscopy [65].

PtPOP experiment

The time-resolved X-ray scattering experiment on PtPOP in water was conducted at the XPP instrument at LCLS to investigate the ground state structural dynamics at the ultrafast (< 5 ps) time scale, as detailed below. Relevant parameters of the experiment are reported in Table 2.1.

In the experiment, the excitation wavelength was 395 nm, on the far red side of the 370 nm peak in the absorption spectrum and in correspondence of the fluorescence peak in the emission spectrum. Fig. 2.13 illustrates the excitation process. A 'hole' in the ground state population is created by selectively exciting solute molecules in a pre-defined geometry: the geometry of the photoselected PtPOP molecules is the equilibrium configuration of the molecules in the singlet excited state. Therefore, the dynamics on the excited state PES is quenched and the main observable of the experiment is expected to be the structural dynamics taking place on the ground state PES.

The PtPOP molecule is a symmetric top molecule, with the main axis of symmetry parallel to the Pt-Pt bond length, which is also the direction of the transition dipole moment photoselected in this experiment. These characteristics meet the assumptions made on the molecular geometry when deriving the formalism to describe the scattering signal from an aligned ensemble of molecules (see Section 2.2.1). Therefore the PtPOP is a good molecule to benchmark this formalism.

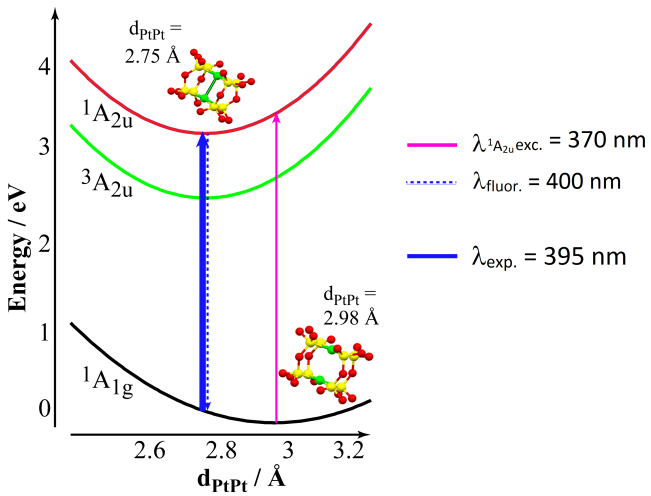

Figure 2.13: PESs of PtPOP as a function of the Pt-Pt distance and some of the possible transitions between them. For the experiment described in this thesis, the excitation wavelength was 395 nm, close to the fluorescence emission line (400 nm), and on the red side of singlet-to-singlet ($1A_{1g} \rightarrow 1A_{2u}$) absorption band centered at 370 nm. In this way, a 'hole' in the ground state state population is created by selectively exciting the molecule with a structural configuration corresponding to the equilibrium configuration of the singlet excited state.

Chapter 3

Data Reduction

This chapter describes the relevant steps in the acquisition, correction, and reduction of (potentially) anisotropic scattering patterns at XFELs. This description refers in particular to experiments performed at XPP, but can be generalized to describe the reduction of similar data measured at any XFEL.

3.1 Data collection

This section describes the types of scattering patterns and some of the relevant beam diagnostics that are usually measured, and then saved for further analysis, in a typical time-resolved X-ray scattering experiments at XPP.

The typical setup for a time-resolved X-ray scattering experiments on liquid samples has been described in chapter 1. Every X-ray pulse hitting the sample yields a scattering image on the CSPAD. A characteristic scattering pattern is shown in Fig. 3.1(a). The stochastic nature of the SASE process characteristic of the XFEL sources [26] leads to big pulse-to-pulse variations and over-time drifting. Therefore, the scattering images, as well as the parameters that describe the beam properties, are saved on a shot-to-shot basis. Some relevant experimental parameters are:

- X-ray intensity. The X-ray intensity is monitored by several diodes along the X-ray beam path. Due to fluctuations of the liquid sheet thickness, an estimate of the intensity actually hitting the sample is calculated as an average (over all pixels) of the intensity recorded by the CSPAD (since it is placed after the sample).
- X-ray energy. The actual photon energy of each pulse is calculated from the electron beam energy measured at the beginning of the undulator.
- Event code. The event code consists of boolean values for the arrival of the laser and the X-rays pulses at the sample position. Based on the event code, the measured 2D patterns can be classified as:
  - Off-images. The laser shot is dropped and only the X-ray pulse hits the sample, so that the image is a snapshot of the sample in the ground state.
  - On-images. Both the laser and the X-ray pulse hit the sample, with a tunable time delay between the two pulses.
  - Dark-images. Both the X-ray and the laser pulses are dropped and the dark images are then measurements of the background.
- Real time. To overcome the $\sim$ 500 fs (FWHM) time-jitter, the time delay t between the laser and the X-ray pulse is measured by a timing tool with an accuracy of $\sim$ 10 fs (FWHM) [66].

The data are first saved as XTC files and then translated into the HDF5 format, which can be more easily accessed by the users. Usually, for each measurement, the delay stage that controls the arrival of the laser pump is moved in discrete steps (nominal time points) and thousands of images are saved at every nominal time point. A measurement, which comprises a range of 10-100 of such time steps, is performed in few minutes (given a repetition rate of 120 Hz) and the resulting HDF5 file is $\sim$ 200 GB in size. For each experiment, hundreds of measurements are collected and tens of TB of data are produced. The reduction of the storage requirements is obtained by creating a summary statistics of the data: 1D scattering curves are extracted from the 2D scattering patterns and used for further analysis.

3.2 Correction of 2D scattering patterns

This section describes how the 2D scattering patterns are corrected, scaled, and time sorted before the extraction of 1D difference scattering curves. In particular, this section provides a summary and an example of the procedure presented

in Paper II for the correction of fluctuating artefacts in 2D scattering patterns. The data shown in this section were collected at XPP during the experiment performed to investigate the photoinduced dynamics of $[Co(terpy)_2]^{2+}$ in water, as introduced in section 2.6.1. The complete analysis of the XDS data is presented in chapter 4.

Background corrections and masking

As a first step in the data correction, several dark images (see above) are averaged to create a background image, which is then subtracted from each raw scattering pattern. Afterwards, a mask is applied to remove unbonded pixels and shaded areas on the detector (such as the beamcenter and possible other shadows due to the experimetal setup). Fig. 3.1(a) shows a raw scattering pattern on the CSPAD and Fig. 3.1(b) shows the same pattern after subtracting the background and masking. The intensity is plotted in Analog-to-Digital Units (ADU) and the dark contribution accounts for $\sim$ 1500 ADU/pixel, decreasing the intensity of the original image of about 25 %.

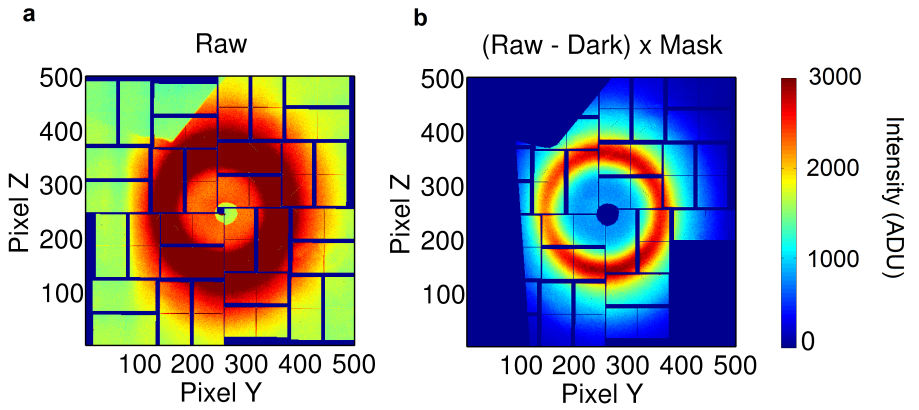

Figure 3.1: **(a)** A characteristic scattering pattern on the CSPAD, with an intense ring at around Q = 2 Å due to scattering from the solvent. **(b)** The same scattering pattern as in (a) after background subtraction and masking.

2D-Singular Value Decomposition

As a second step, a Singular Value Decomposition (SVD) of the scattering images is used to identify fluctuating components in the data set due to e.g. detector non-linearity and the SASE nature of the source. As described in Paper II, if these components are found to be correlated with shot-to-shot fluctuations of the beam parameters, they can be assigned a physical interpretation and removed from the data set.

Fluctuations of the same order of magnitude of the difference scattering signal were highly visible in the data collected when using the first version of the CSPAD detector [67]. These fluctuations are explained as deviations from the expected linear response of the detector and they appear in the signal independently on the dynamics photoinduced in the sample. Initially, these artefacts were identified in the following way: the components obtained from a SVD of the 1D difference scattering curves before the excitation event (time zero) are included into the model used to describe the signal after time zero [68, 16]. Afterwards, a method was developed to remove these fluctuations from the 2D scattering patterns, before the extraction of the isotropic and anisotropic contributions. This method is presented in Paper II and, in this thesis, such a method is referred to as 2D-SVD. The 2D-SVD is done on the Off-images, that are supposed to be nominally identical, and allows identifying the cause of the fluctuations in the data by looking at their dependency on the variations of the beam parameters. As an advantage compare to the previous method, the 2D-SVD is independent on the knowledge of the specific system under investigation. The 2D-SVD procedure is described and exemplified below.

Description of the 2D-SVD

The 2D-SVD procedure is illustrated in Fig. 3.2. Each Off-image is unrolled in a column vector and a series of Off-images are collected into a l x h matrix M, where l is the total number of pixels in an image and h is the number of Off-images considered, and decompose such that:

$$M = U \cdot S \cdot V^T \tag{3.1}$$

where U is an orthonormal l x r matrix whose columns are called left singular vectors of M (referred to as SVD-components); S is a r x r matrix whose diagonal elements $S_{i,i}$ are the singular values (and $S_{1,1} > S_{2,2} > .. > S_{i,i} > .. > S_{r,r} > 0$); V is a orthonormal h x r matrix whose columns are the right singular vectors and carries information about the column-to-column variation of M. r is the chosen rank of the SVD decomposition, and it can be equal or smaller than h, the original number of Off-images considered.

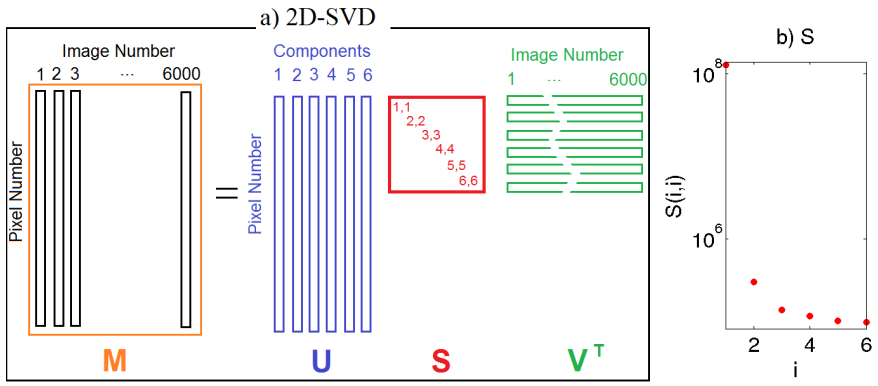

Figure 3.2: **(a)** Illustration of a rank-6 2D-SVD approximation, as described in the text and in Eq. 3.1. Matrix M contains, as columns, a series of 2D-Images. M is decomposed into a U matrix (whose columns are SVD-components), a S matrix (whose diagonal elements are the singular values), and a V matrix (whose columns represents the magnitude of each component as a function of number of 2D-Images). **(b)** Singular values obtained from a rank-6 2D-SVD of a series of Off-Images measured upon probing solvated $[Co(terpy)_2]^{2+}$ at XPP. The first component dominates the signal. The SVD-components and the amplitudes are shown in Fig. 3.3 and Fig. 3.4.

2D-SVD on the $[Co(terpy)_2]^{2+}$ data set

Fig. 3.2(b) shows the singular values $S_{i,i}$ (with i = 1,..,6) obtained after a rank-6 2D-SVD of the Off-images measured upon probing $[Co(terpy)_2]^{2+}$ in water. The first component accounts for more than 99% of the signal. Fig. 3.3(a) and Fig. 3.4(a) show, respectively, the first three components (i = 1, 2 and 3) and the second three component (i = 4, 5 and 6) obtained from the decomposition. Fig. 3.3(b) and Fig. 3.4(b) show, for each component i, the amplitude ($S_{i,i} \cdot V_i$) as a function of the number assigned to each Off-image. This number correspond to the order in which the images were collected during the experiment.

Correlation with X-ray energy and intensity

In Fig. 3.3(c) and Fig. 3.4(c), the amplitude of the components is plotted against the X-ray intensity (blue dots), while in Fig. 3.3(d) and Fig. 3.4(d) the amplitude is plotted against the X-ray energy (green dots). The black points in these plots represent a 9th order polynomial fit to the data. The goodness of fit is deter-

mined by an R^2-measure and used to establish the dependence of the amplitude on the beam parameters. In Fig. 3.3: Component 1 is linear in X-ray intensity, as expected assuming a linear detector; Component 2 is found dependent on X-ray energy; Component 3 doesn't correlate to either of the parameters. With respect to Component 3, the intensity fluctuating with opposite sign in the left and right side of the detector is most likely connected to the liquid jet being tilted 45 degrees about the z axis (since the setup was optimized to record X-ray emission lines other than scattering). In Fig. 3.4: Component 4 correlates with X-ray intensity; Component 5 and 6 are independent of the beam parameters.

Correction of the data set

The parametric description found for Components 2 and 4, whose amplitude is found dependent on X-ray energy and intensity, respectively, can be used to subtract these components from each raw image of the dataset. In this way the On-images are corrected for the artefacts, without danger of removing any signal arising from the photoinduced dynamics in the sample. The sum of Components 2 and 4 accounts, on average, for ~ 3.1 ADU/pixel, which correspond to 0.3 % of the total scattering signal. Since this value is on the same order of magnitude of the difference scattering signal, the effect of applying the 2D-SVD is evident when looking at the reduced difference scattering curves, as shown in Fig. 3.5.

After correcting for these fluctuations, a second 2D-SVD was performed on the Off-images. This is shown in Appendix B and it confirms the robustness of the method: the previous Components 2 and 4 are no longer present in the corrected data set and the others components scale up in position accordingly; moreover, the dependencies of the new components on the X-ray energy and X-ray intensity are investigated and no correlations are found.

Other corrections and scaling

After the subtraction of the SVD components that correlate with X-ray intensity and energy, every 2D image is also corrected for X-ray polarization and absorption through the liquid sheet, as well as solid angle covered by each pixel [69]. A combination of these corrections is shown in Fig. 3.6(a). Each individual 2D image is then scaled to the liquid unit cell reflecting the stoichiometry of the sample [20], yielding the acquired signal in electron units per solute molecule (e.u./molec.). Fig. 3.6(b) shows the scattering patterns measured upon photoexcitation of solvated $[Co(terpy)_2]^{2+}$ (see also Fig. 3.1) after corrections and scaling.

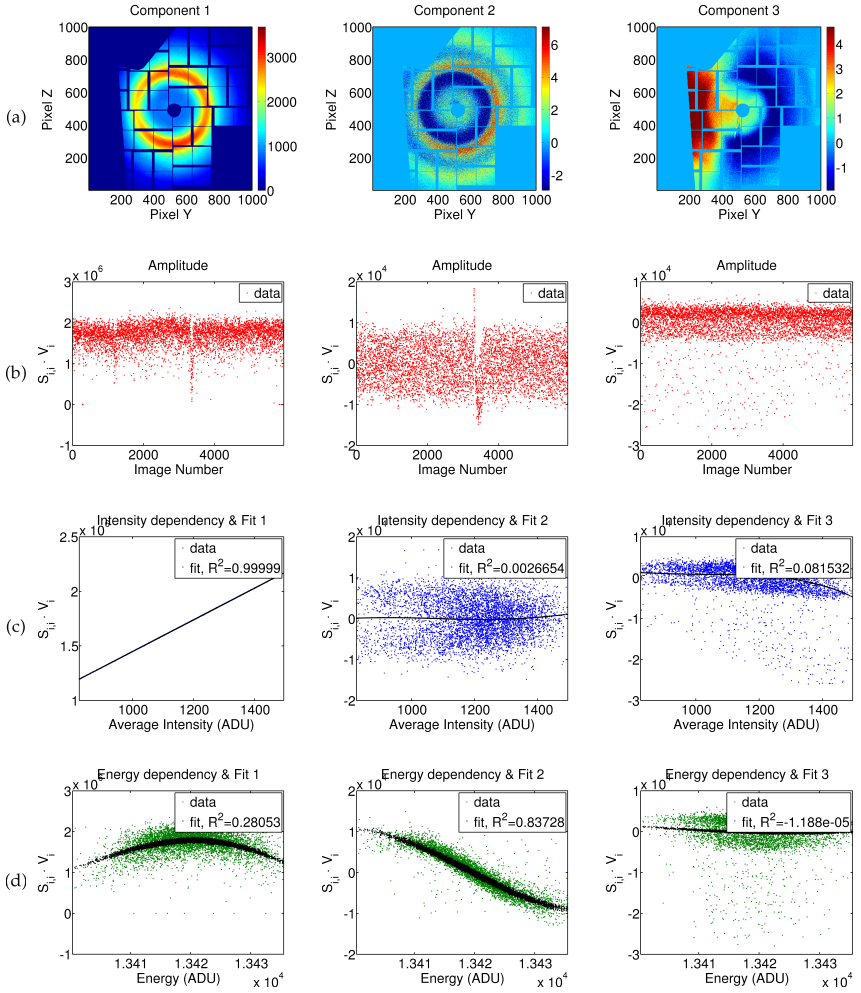

Figure 3.3: Results of a rank-6 2D-SVD of scattering patterns, as described in the text and in Eq. 3.1. **(a)** Components 1, 2 and 3 visualized on the CSPAD. Each component U is multiplied by its mean amplitude. **(b)** Amplitude of the component as a function of acquisition time. **(c)** Amplitude of the components against X-ray intensity (blue dots) and polynomial fit (black dots). **(d)** Amplitude of the components against the electron beam energy (red dots) and polynomial fit (black dots).

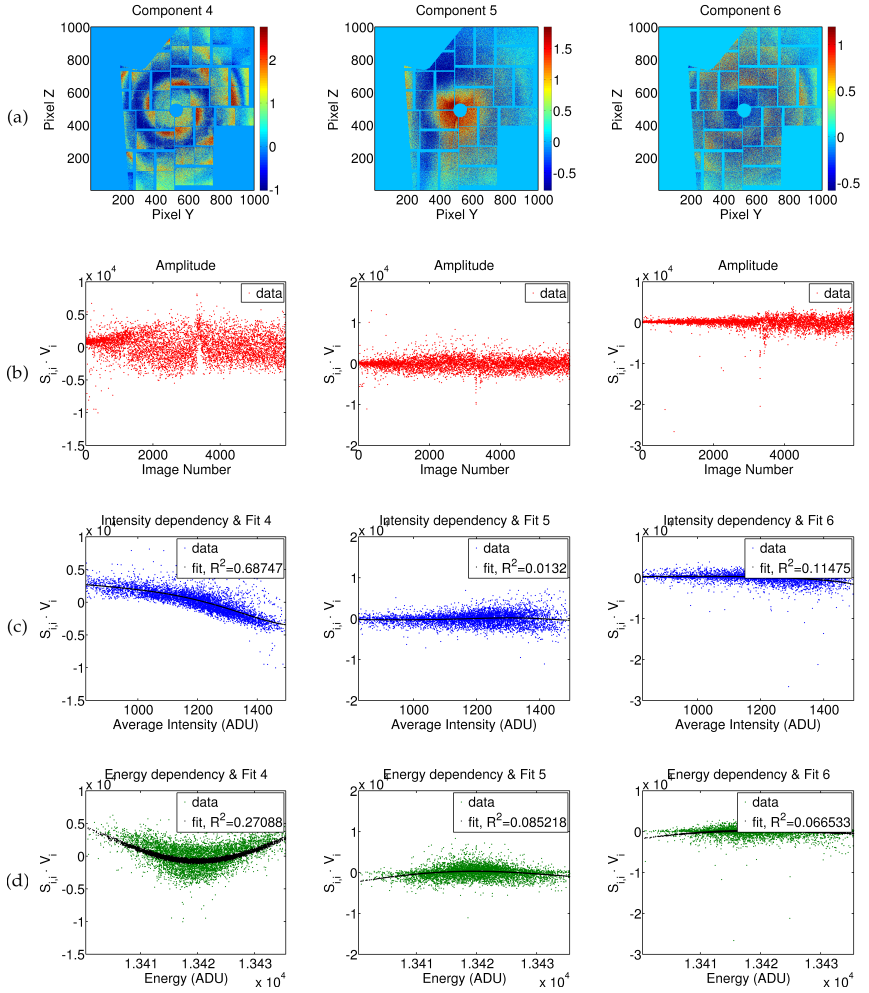

Figure 3.4: Results of a rank-6 2D-SVD of scattering patterns, as described in the text and in Eq. 3.1. **(a)** Components 4, 5 and 6 visualized on the CSPAD. Each component U is multiplied by its mean amplitude. **(b)** Amplitude of the component as a function of acquisition time. **(c)** Amplitude of the components against X-ray intensity (blue dots) and polynomial fit (black dots) **(d)** Amplitude of the components against the electron beam energy (red dots) and polynomial fit (black dots).

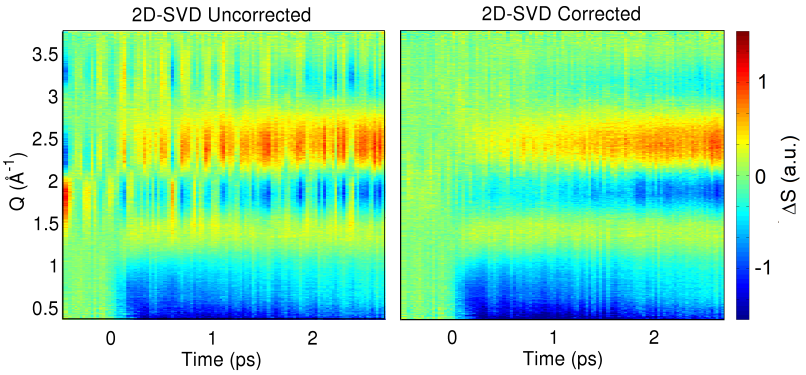

Figure 3.5: Isotropic difference scattering signal upon photoexcitation of $[Co(terpy)_2]^{2+}$ in solution. The data have been extracted from the 2D scattering patterns before (left) and after (right) removal of fluctuations with 2D-SVD.

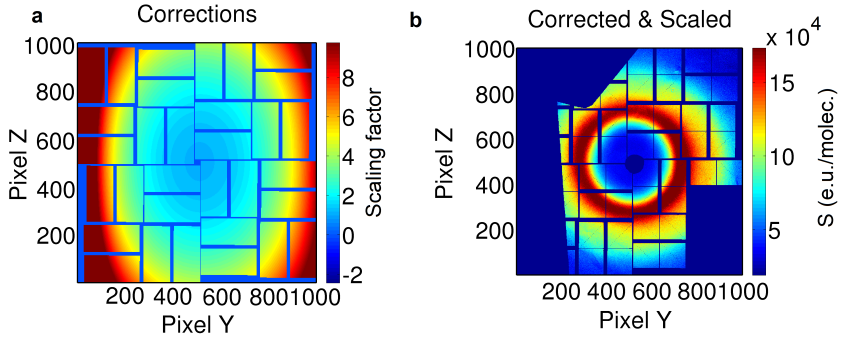

Figure 3.6: **(a)** The combination of all the corrections (geometry, absorption of the liquid sheet, X-ray polarization) applied to each measured 2D scattering pattern. **(b)** The scattering pattern shown in Fig. 3.1, after correction and scaling.

2D difference scattering patterns

From the corrected scattering patterns, the difference scattering images are created by subtracting from each On-image the mean of the two Off-images measured, respectively, immediately before and after that specific On-image. Fig. 3.7(a) shows one single difference scattering pattern collected 1 ps after the photoexcitation of $[Co(terpy)_2]^{2+}$ in water. Such an image shows a very low signal-to-noise (S/N) ratio. Difference images from multiple measurements are

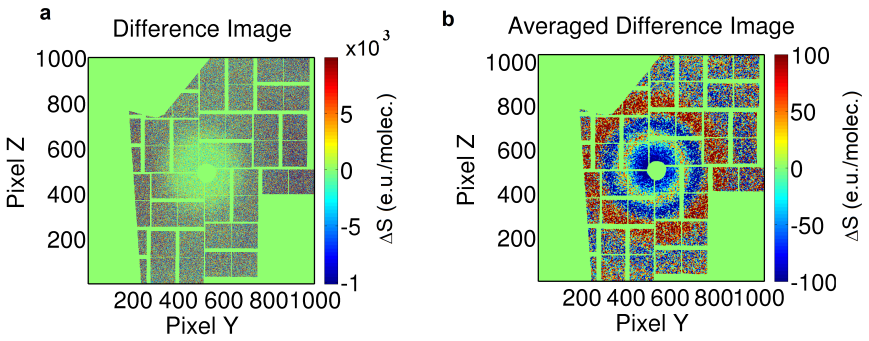

Figure 3.7: **(a)** Difference scattering pattern measured 1 ps after the photoexcitation of $[Co(terpy)_2]^{2+}$ in water. **(b)** Average of ~ 600 difference scattering pattern measured ~ 1 ps after the photoexcitation of $[Co(terpy)_2]^{2+}$ in water.

therefore binned in time and averaged when belonging to the same time bin. Fig. 3.7(b) shows an average of ~ 600 images collected in a 30 fs wide time bin centred at 1 ps. By comparison with the total scattering signal shown in Fig. 3.6(b), the difference scattering signal is ~ 0.1 % of the total scattering.

3.3 From 2D patterns to 1D curves

This section describes the extraction of 1D isotropic and anisotropic scattering curves from the 2D difference scattering patterns. The procedure is exemplified on a data set collected at XPP to investigate the photoinduced dynamics of PtPOP in water. This experiment is described in section 2.6.2.

As described in chapter 2, in a pump-probe experiment on molecules in solution, the laser pump excites the molecules whose transition dipole moment has a favourable orientation with respect to the laser polarization axis. Assuming this orientation to be a cosine-square distribution, the difference scattering signal can be written as:

$$\Delta S(Q, \cos\theta_q) \propto \Delta S_0(Q) - P_2(\cos\theta_q)\Delta S_2(Q) \tag{3.2}$$

where S_0 and S_2 represent the isotropic and anisotropic scattering, respectively, and P_2 is a second order Legendre polynomial that depends on the angle (θ_q)

between the laser polarization axis and the scattering vector Q:

$$P_2(\cos\theta_q) = \frac{1}{2}(\cos^2\theta_q - 1) \tag{3.3}$$

As shown by Eq. 3.2, at each fixed Q value a linear relationship is established between ΔS and P_2. In particular, for each fixed Q value, the extraction of the isotropic and anisotropic scattering curves can be done through a straight line fit [29], as exemplified in the following.

In the PtPOP experiment, the laser polarization axis was perpendicular to the direction of propagation of the X-ray beam (x axis) and at 20 degrees with respect to the vertical axis (z axis). Therefore, as seen in chapter 2 (Eq. 2.22):

$$\cos\theta_q = -\cos\theta\cos\phi \tag{3.4}$$

where ϕ is the azimutal angle and θ is half of the scattering angle. Fig. 3.8(a) shows P_2 mapped on the CSPAD and calculated accordingly to this specific experimental setup, with $\phi = 0$ along the direction of the projection of the laser polarization axis on the detector surface. Fig. 3.8(c) shows P_2 plotted as a function of azimuthal angle ϕ for a fixed value of scattering angle 2θ, correspondent to Q = 2 Å.

Fig. 3.8(b) shows an an average of 80 difference scattering patterns collected in a $\sim$ 40 fs wide time bin centred at 4.5 ps (after photoexcitation of the sample). The 2D pattern was divided in 500 radial bins and 45 azimuthal bins. The difference scattering signal corresponding to the radial bin centred at Q = 2 Å^{-1} (white circle) is plotted in Fig. 3.8(d) versus the value of P_2 at the same Q value. The red line is a straight line fit of the data points. The fit, according to Eq. 3.2, yields ΔS_2 (Q = 2 Å^{-1}) as negative slope and ΔS_0 (Q = 2 Å^{-1}) as intercept with the $P_2 = 0$ axis. The fitting procedure is discussed in more detail in the next section. Repeating the procedure for all the radial bins yields the 1D isotropic and anisotropic difference scattering curve for the full Q range at this specific time delay: Fig. 3.9 shows ΔS_0 and ΔS_2 extracted from the scattering pattern measured at 4.5 ps. The bars are calculated according to the procedure described by Haldrup *at al.* [20] and in Paper III. Once the isotropic and anisotropic contributions have been separated, they can be re-projected independently on the detector surface. ΔS_0 gives rise to an isotropic scattering pattern (Fig. 3.10(a)), while the projection of ΔS_2, being modulated by P_2, yields an anisotropic scattering pattern (Fig. 3.10(b)). Fig. 3.10(c) shows the reconstructed full 2D difference scattering signal accordingly to Eq. 3.2 and Fig. 3.10(d) shows the residuals obtained after subtracting the reconstructed pattern from the measured one. The latter shows comparatively low-residuals, that are isotropically distributed on the CSPAD.

As introduced in chapter 1, the established procedure to reduce scattering data

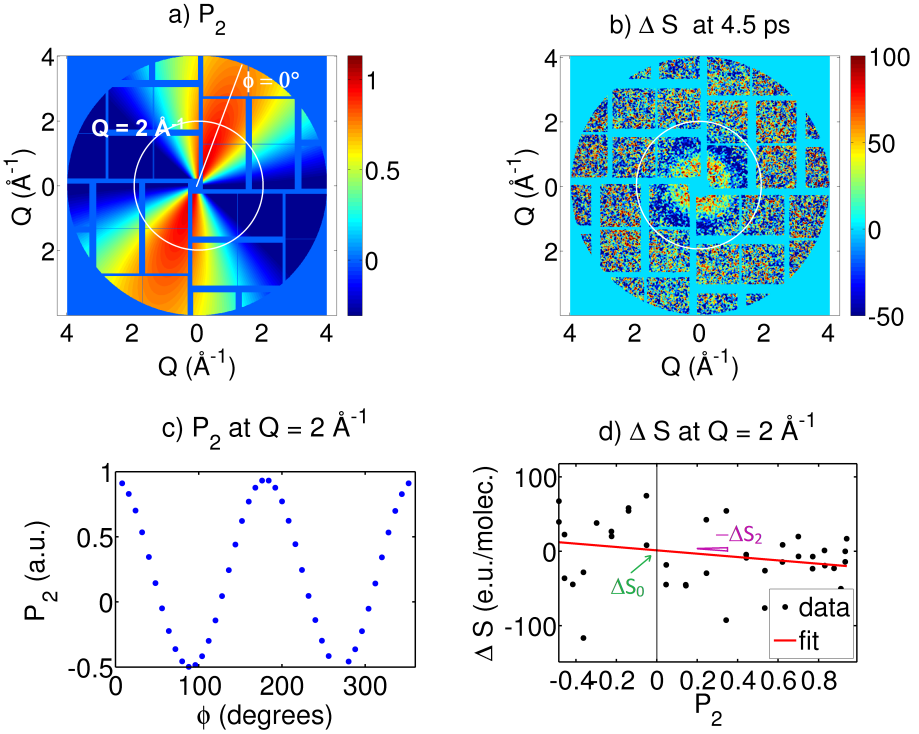

Figure 3.8: **(a)** P_2 (Eq. 3.3) mapped on the CSPAD. The azimuthal angle (ϕ) is zero in correspondence of the projection on the detector surface of the laser polarization axis. A radial bin corresponding to Q = 2 Å^{-1} is selected. **(b)** Averaged difference scattering pattern at 4.5 ps after the photoexcitation of the sample. **(c)** Value of P_2 for the specific radial bin selected in panel (a), correspondent to Q = 2 Å^{-1}. **(d)** Difference scattering signal ΔS at Q = 2 Å^{-1} versus P_2 (black dots) and fitted straight line (red).

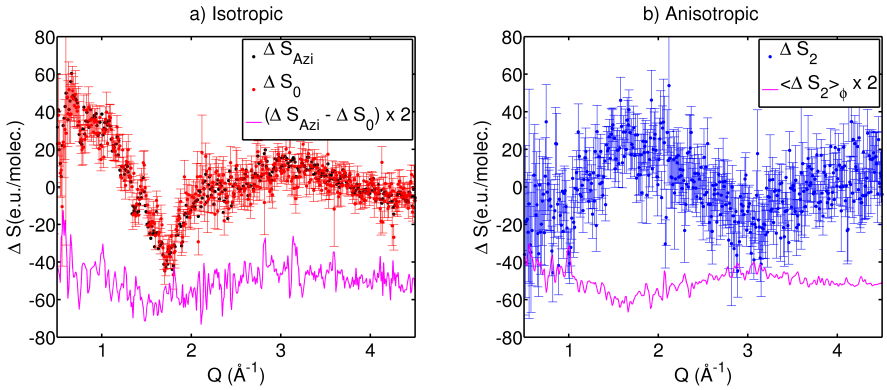

Figure 3.9: **(a)** Extracted ΔS_0 (red points) and ΔS_{azi} (black points) from the pattern in Fig. 3.8(b). The magenta line shows the difference (offset and multiplied by two) between the two curves. **(b)** Extracted ΔS_2 from the same pattern (blue points) and azimuthal average (offset and multiplied by two) of $-P_2\Delta S_2$ (the magenta line). See also Fig. 3.10(b).

from liquid sample consists of a radial integration of the 2D scattering patterns [20, 19]. The obtained radially integrated 1D signal is usually assumed as arising from an isotropically distributed ensemble of molecules, and therefore interpreted by comparison with models calculated using the Debye formula. However, this assumption is not always valid, as shown in the following.

Going back to Fig. 3.9, Fig. 3.9(a) shows the isotropic contribution ΔS_0 extracted from the 2D scattering pattern at 4.5 ps (in Fig. 3.8(b)) and an azimuthal integration ΔS_{azi} of the same pattern. The magenta line shows the difference between ΔS_{azi} and ΔS_0 and this signal is on average (in the full Q range) 6 % of the magnitude of ΔS_0. From Eq. 3.2, such a difference between the isotropic scattering and the radial integration is expected to be due to the presence of the anisotropic contribution on the 2D pattern. This is confirmed by looking at Fig. 3.9(b), which shows the anisotropic contribution ΔS_2 and the signal (magenta line) obtained from an azimuthal integration of the anisotropic contribution projected on the detector surface ($-P_2\Delta S_2$, shown in Fig. 3.10(b)). The latter is found similar to the difference between the isotropic signal and the radial integration (magenta line in Fig. 3.9(a)).

For the same dataset, the difference between the azimuthal integration and the extracted isotropic contribution at time delays immediately after the excitation event, where the anisotropy is more pronounced, is found to be ~ 20 % of the magnitude of the isotropic contribution. These observations indicate that the azimuthal signal can be greatly affected, both in magnitude and shape, by the

presence of the anisotropic contribution on the 2D pattern and cannot then be always considered as a true representation of the scattering arising from an isotropic ensemble.

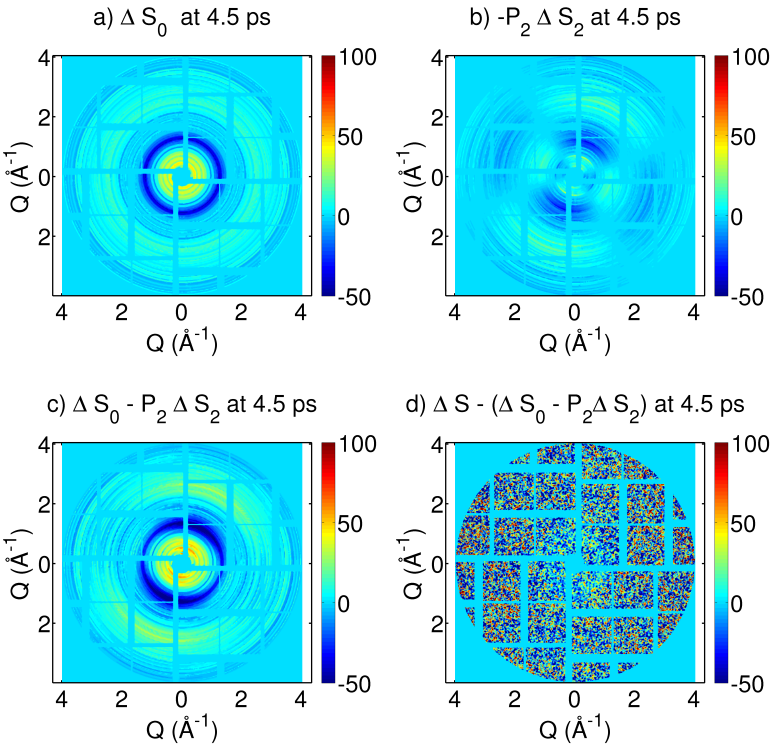

Figure 3.10: For illustration purposes, the isotropic and anisotropic contributions extracted from the 2D pattern in Fig. 3.8(b) are re-projected separately onto the CSPAD. **(a)** Projection on the CSPAD of ΔS_0. **(b)** Projection on the CSPAD of $-P_2\Delta S_2$. The azimuthal integration of this signal is shown in Fig. 3.9(b). **(c)** Reconstruction of the full pattern: ΔS_0 - $P_2\Delta S_2$. **(d)** Residuals between the reconstructed pattern in (c) and the measured difference scattering pattern in Fig. 3.8(b), from which Δ_0 and ΔS_2 were extracted.

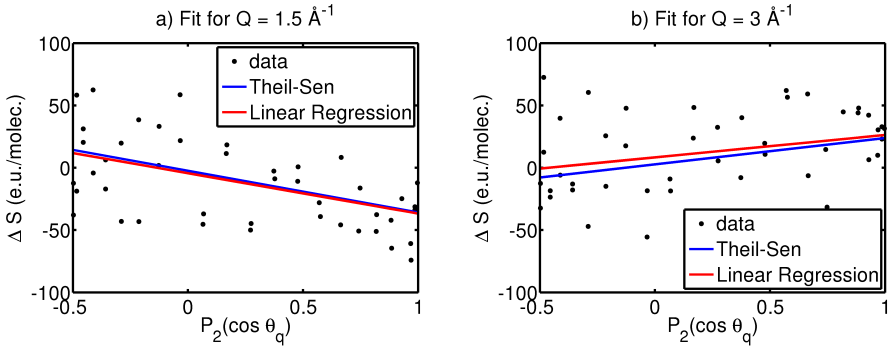

Figure 3.11: Difference scattering signal at a fixed Q value [(a) Q = 1.5 Å^{-1}, (b) Q = 3 Å^{-1}] versus P_2 and straight line fit obtained with a simple regression (the red line) and with the Theil-Sen method (the blue line). According to Eq. 3.2, the intercept with the P_2=0 axis yields ΔS_0 and the negative slope yields ΔS_2 at that specific Q value.

Straight line fitting procedure

This sections describes the robust extraction of ΔS_0 and ΔS_2 from a measured difference scattering pattern.

With respect to the pattern in Fig. 3.8(b), Fig. 3.11 shows the difference scattering signal as a function of $P_2(\cos\theta_q)$ (black dots) for two specific Q values, Q = 1.5 Å^{-1} and Q = 3 Å^{-1}, and a linear fit of these points. The fit, according to Eq. 3.2 and as described above, yields ΔS_2 as negative slope and ΔS_0 as intercept with the P_2=0 axis. Since the data set can contain outliers, the fitting procedure is made more robust by using the Theil-Sen method (the blue line in Fig. 3.11) rather than the simple linear regression (the red line). According to the Theil-Sen method [70, 71, 72], given n data points $[(x_i, y_i)\ 1 < i < n]$, the slope is calculated as the median m of the slopes $m_{i,j}$ determined by all pairs of data points:

$$m_{i,j} = \frac{y_j - y_i}{x_j - x_i}, 1 < i < n, 1 < j < n, i \neq j \tag{3.5}$$

and the intercept as the median of the values $y_i - mx_i$. If there are not outliers, the two methods yield similar results, as for the examples shown in Fig. 3.11.

3.4 Analysis of 1D curves

The isotropic and anisotropic difference scattering signals are further analysed with modelling. This section describes how the 1D difference scattering curves can be modelled.

The quantitative treatment of XDS data is to simulate the scattering intensity from the sample and compare such a signal against the measured data using a maximum likelihood framework [20, 19]. As described in section 2.5, the difference scattering signal (both isotropic and anisotropic) at a specific time point can be modelled as:

$$\Delta S(Q) = \Delta S_{\text{solute}}(Q) + \Delta S_{\text{cage}}(Q) + \Delta S_{\text{solvent}}(Q). \tag{3.6}$$

The following describes how to modelled each of these contributions.

Solute

ΔS_{solute} can be calculated from the DFT structures of the ground and excited state(s) of the molecule. As described in chapter 2, the isotropic contribution is calculated through the Debye formula:

$$S_0^{gs/es}(Q) = \sum_{i,j}^{N} f_i(Q) f_j(Q) \frac{sin(Qr_{ij})}{Qr_{ij}}, \tag{3.7}$$

while the anisotropic contribution is calculated as:

$$S_2^{gs/es}(Q) = 2 \sum_{i,j}^{N} f_i(Q) f_j(Q) P_2(\cos\theta_{ij}) j_2(Qr_{ij}), \tag{3.8}$$

where P_2 is the second order Legendre polynomial and j_2 the second order spherical Bessel function. In Eq. 3.7 and Eq. 3.8, N is the number of atoms in the molecule; r_{ij} the interatomic distance between atom i and atom j; and θ_{ij} the angle between the transition dipole moment of the molecule and r_{ij}. gs and es refer, respectively, to the DFT structures corresponding to the ground and the excited state of the molecule. As detailed in Appendix A, the isotropic difference scattering signal is calculated as:

$$\Delta S_0(Q) = S_0^{es}(Q) - S_0^{gs}(Q), \tag{3.9}$$

and the anisotropic difference scattering signal as

$$\Delta S_2(Q) = S_2^{es}(Q) - S_2^{gs}(Q). \tag{3.10}$$

For the structural refinement (or for the description of structural dynamics), some interatomic distances of the original DFT structures are changed in order to create a variety of possible geometries for either the ground or the excited state of the molecule. Since refinement of each interatomic distance independently cannot be achieved due to limitation on the number of parameters which can be deduced from the XDS signal [20], certain interatomic distances will be selected as main parameters and varied from the original DFT-calculated values. Then, by connecting such variations with the variations in the rest of the structure, the overall molecular structure can be refined as a function of the selected parameters. Such selected distances are usually those corresponding to the atom pairs that contribute the most to the scattering signal, i.e. the pairs of the heavy atoms in the molecule. Historically, the XDS technique has mostly been used to refine structures of molecules typically containing strong scatterers like ruthenium [12, 73], iodine [74, 11, 18], iridium [15] or platinum [14]. In polyatomic molecules where several atoms pair have the same scattering power, the analysis is more challenging because of the many degrees of freedom involved. This can be the case for transition metal complexes where carbon- and nitrogen-based ligands are attached to a central metal atom.

Cage

In this analysis framework, the cage term describes the changes in the solute-solvent distances of the sample. Such distances are usually calculated through molecular dynamics (MD) or quantum mechanical (QM) calculations and expressed as RDFs. ΔS_{cage} can then be calculated with the formalism seen above with respect to the solute contribution (Eq. 3.7 and Eq. 3.8), but using RDFs instead of fixed nuclear arrangements. How to calculate isotropic scattering signal from RDFs is covered in Paper I. In order to calculate anisotropic scattering, the RDFs should be angle-resolved [29], and this approach has not yet been implemented. With respect to the analysis presented in chapter 4 and chapter 5, ΔS_{cage} is assumed to describe the changes in geometry and rearrangements of the solvent molecules in close proximity to the solute.

Solvent

As introduced in section 2.5, the (isotropic) contribution to the difference scattering signal from the changes of the thermodynamic properties of the bulk solvent can be modelled as:

$$\Delta S_{solvent}(Q) = \Delta T \frac{\partial S(Q)}{\partial T}\bigg|_{\rho} + \Delta\rho \frac{\partial S(Q)}{\partial \rho}\bigg|_{T} \tag{3.11}$$

where ΔT and $\Delta\rho$ are the changes in temperature and density, respectively, $\left.\frac{\partial S(Q)}{\partial T}\right|_{\rho}$ is the temperature differential and $\left.\frac{\partial S(Q)}{\partial \rho}\right|_{T}$ is the density differential. The solvent differentials for a large range of solvent have been obtained by performing separate solvent-heating experiments [44, 43].

Chapter 4

Femtosecond structural dynamics of a solvated metal complex

This Chapter aims at exemplifying the structural analysis of a time-resolved X-ray scattering data set on a transition metal complex in solution. Specifically, the analysis is done on a data set collected at XPP to investigate the dynamics of $[Co(terpy)_2]^{2+}$ upon photoinduced SST. The system and the experiment are described in section 2.6.1. This chapter revisits the content of Paper III.

4.1 Structural analysis of the [Co(terpy)2]2+ data set

This Section describes the model used for the analysis of the difference scattering signal measured upon photoexcitation of solvated $[Co(terpy)_2]^{2+}$ and presents the obtained results.

Model

Fig. 4.1(a) shows the isotropic difference scattering signal ΔS_0 measured upon photoexcitation of $[Co(terpy)_2]^{2+}$ in aqueous solution. As described in Section 3.4, the difference scattering signal can be described as arising from three contributions: the changes in the solute structure (ΔS_{solute}), the changes in geometry and rearrangements of the solvent molecules in close proximity to the solute (ΔS_{cage}), the temperature and density changes of the bulk solvent. For this data set, the density changes were found to be negligible [Paper III], and only the temperature solvent differential ($\frac{\partial S(Q)}{\partial T}\Big|_\rho$) was included in the model. The following expression was then used to fit the difference scattering signal at every time point:

$$\Delta S^{\text{model}}(Q) = \alpha \Delta S_{\text{solute}}(Q) + \beta \Delta S_{\text{cage}}(Q) + \Delta T \frac{\partial S(Q)}{\partial T}\Big|_\rho . \qquad (4.1)$$

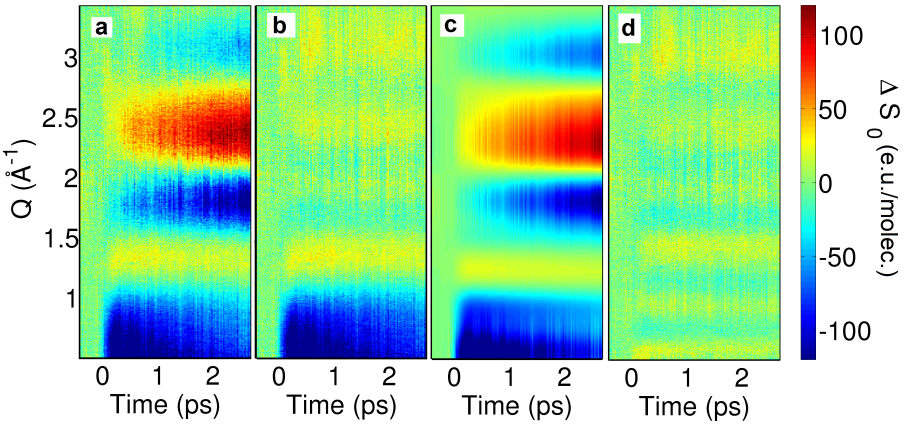

Figure 4.1: **(a)** Isotropic difference scattering signal ΔS_0 measured upon photoexcitation of $[Co(terpy)_2]^{2+}$ in water. **(b)** Structural signal measured upon photoexcitation of $[Co(terpy)_2]^{2+}$ in water, obtained as $\Delta S_0 - \Delta S_{\text{solvent}}$, i.e. by subtracting the solvent contribution from the measured data. **(c)** Model ($\Delta S_0^{\text{model}}$) obtained by fitting Eq. 4.1 to the measured data. **(d)** Residuals obtained by subtracting the model from the measured data ($\Delta S_0 - \Delta S_0^{\text{model}}$).

The three components of the fit are shown in Fig. 4.2(a). ΔS_{solute} is constructed from the DFT structures of the LS and HS state of $[Co(terpy)_2]^{2+}$, whose main

	LS	HS		DFT	Measured
$d_{\text{Co-Naxial}}$ (Å)	1.902	2.058	$\Delta d_{\text{Co-Naxial}}$ (Å)	0.16	0.13
$d_{\text{Co-Nequatorial}}$ (Å)	2.08	2.16	$\Delta d_{\text{Co-Nequatorial}}$ (Å)	0.08	0.06
η	0.91	0.95			

Table 4.1: Structural parameters of the DFT-calculated LS and HS structures of $[Co(terpy)_2]^{2+}$ obtained in the present study. $d_{\text{Co-Naxial}}$ and $d_{\text{Co-Nequatorial}}$ are averages over the two axial and the four equatorial metal-ligand bond distances, respectively, and $\eta = \frac{d_{\text{Co-Naxial}}}{d_{\text{Co-Nequatorial}}}$. A pseudo Jahn-Teller effect affects the LS state, so that η is smaller than in the HS state. The change of each parameter upon the LS $\rightarrow$ HS spin transition is also reported and compared with the values obtained from the measured data. Table from Paper III.

structural parameters are reported in Table 4.1. The main structural change involves the lengthening of the Co-N bonds, leading to a negative difference scattering signal in the low Q region. ΔS_{cage} is calculated from the RDFs obtained through MD simulation after solvating the LS and HS DFT structures in water boxes [Paper I, Paper III]. Finally, the temperature differential (the pink line in Fig 4.2(a)) was obtained from previous measurements [44] and its main features are above 1.5 $Å^{-1}$.

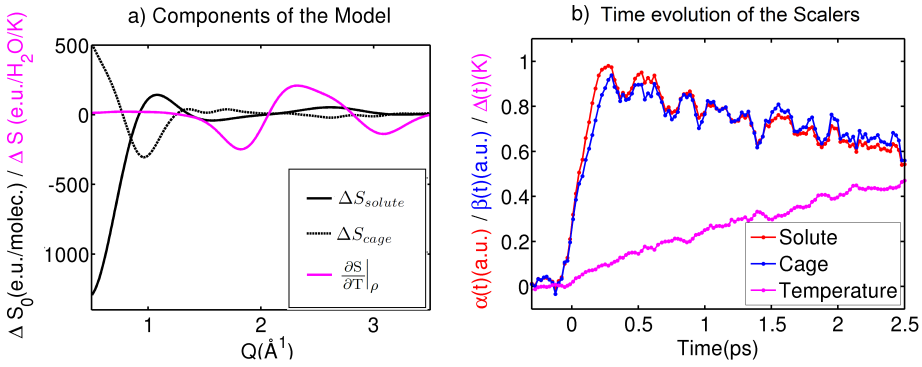

Figure 4.2: **(a)** Contributions used to model the difference scattering signal from the sample (Eq. 4.4). **(b)** Scaler values obtained when fitting Eq. 4.4 to the measured data.

Results

Fig. 4.1(c) shows the full model obtained after fitting Eq. 4.1 to the measured ΔS_0 upon photoexcitation of $[Co(terpy)_2]^{2+}$ and Fig. 4.1(d) shows the residuals after subtracting the model from the measure data. The relatively low residuals show that the three components included in the model (solute, cage, and solvent) can describe the relevant features present in the data set.

Fig. 4.2(b) shows the time evolution of the scaler values obtained from fitting Eq. 4.1 to the data. The magnitude of the solute contribution (α, the red line) grows-in in less than 300 fs (indicating an ultrafast elongation of the Co-N bonds) and then decays on the few picoseconds time scale with an oscillatory behaviour. This decay cannot be easily related to physical quantities, since the time evolution of α depends on both population kinetics and structural dynamics, as further detailed in the next section.

The scaler of the cage contribution (β, the blue line) evolves similarly to that of the solute, with a slightly slower grow-in at early time scale. This could maybe be an indication of the time it takes to the water molecules to respond to a structural change of the solute. This observation is consistent with the fact that, in this analysis framework, the calculated cage signal describes the packing of the solvent molecules around the thermally equilibrated LS and HS structures of $[Co(terpy)_2]^{2+}$. The close similarity between the cage and the solute dynamics indicates a very fast geometric solvent re-organization in response to the changes of the solute structure.

Finally, the magenta line shows the magnitude of the temperature component. ΔT grows in the few picosecond time scale, signifying a temperature increase of the bulk solvent following energy deposition due to relaxation of the solute. From the analysis of a long-time range measurement presented in Paper III, the total increase in temperature is found to be ~ 0.8 K and the process occurs within ~ 4 ps. The bulk solvent contribution is not discussed further in this work and details of the analysis and of the energetics can be found in Paper III.

4.2 Structural signal

This section investigates in more detail the structural contribution to the signal measured upon photoexcitation of solvated $[Co(terpy)_2]^{2+}$. This investigation yields information necessary to conduct further structural analysis on the data set.

Fig. 4.1(b) shows the measured isotropic difference scattering signal ΔS_0 after subtraction of the solvent contribution. Such a signal comprises contributions from both changes in the solute structure and changes in the solvation shells surrounding the solute upon photoexcitation. It is mainly dominated by a negative signal at low Q, which is characteristic of a decreased electron density on the scale of the molecular dimension, and indicates an elongation of the Co-N bonds. Oscillations as a function of time can also be observed in the low Q part of the data. These oscillations can be related to fluctuations in the amplitude of the structural changes giving rise to this signal, in this case the changes in the the Co-N bond lengths.

After a rank-5 SVD of the structural signal, the first components is found to describe 99 % of the data [Paper III]. This is consistent with the previous observation that solute and cage show the same kinetics. The time evolution of the amplitude of the first component is shown in Fig. 4.3(a) (the red line) and shows an ultrafast grow-in followed by oscillations superimposed on a monotonic decay. A broadened exponential decay (the black line) describes this temporal evolution well, except for the oscillatory part of the signal. The blue line shows the difference between the data and the fit and describes the oscillatory structural signal (OSS) present in the data.

Fig. 4.3(b) shows a time dependent Fourier Transform of the OSS. It is obtained, at each time point, by fast Fourier transforming the OSS in a 2 ps interval around that data point, after applying a Hann window. It is seen that two main frequencies dominate the oscillatory signal: the main one appears immediately after the excitation event and has a broad band around T = 340 fs; a second one kicks in after $\sim$ 1 ps, with higher frequency (corresponding to a period T = 230 fs) and weaker intensity than the main one.

The interpretation of the observed frequencies is bound to a closer investigation of the structural dynamics. For a quantitative interpretation, such a dynamics needs to be distinguished from the population kinetics, that happen on the same timescale. This is further discussed below.

4.3 Structural dynamics vs population kinetics

This section describes the model used for a quantitative description of the structural dynamics measured upon photoexcitation of solvated $[Co(terpy)_2]^{2+}$. With respect to Paper III, this section stresses the description of the procedure used to disentangle structural dynamics and population kinetics.

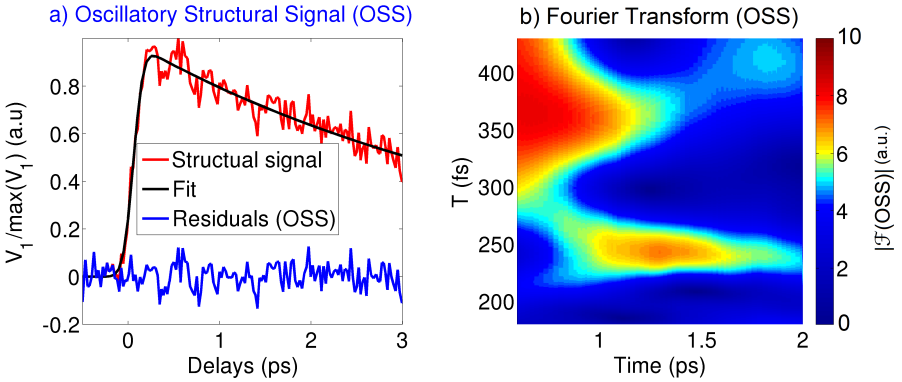

Figure 4.3: **(a)** The red line illustrates the first SVD component obtained by a SVD of the structural signal in Fig. 4.1(b). The black line is a fit to the signal (broadened exponential decay). The blue line is the difference between the signal and the fit and it is referred to as Oscillatory Structural Signal (OSS). **(b)** Time depended fast Fourier Transform of the OSS, showing the two main frequencies that dominate the signal.

Model

The description of the structural dynamics was obtained by the fitting of the data according to the model described above and by varying the HS structure of $[Co(terpy)_2]^{2+}$. Specifically, the axial Co-N bond length could vary up to $\pm$ 0.1 Å from the original DFT-calculated value (see Table 4.1). The ratio η between the equatorial and the axial bond of the molecule was kept constant [75, 17]. In this way, the structural changes are parametrized through the axial Co-N distance of the HS state ($d_{\text{Co-Naxial}}$) and the equatorial Co-N bond can be calculated as $d_{\text{Co-Nequatorial}} = \eta d_{\text{Co-Naxial}}$. The difference scattering signal arising from the changes in the solute structure is written as:

$$\Delta S_{\text{solute}}(Q,t) = \Delta S_{\text{solute}}(Q, d_{\text{Co-Naxial}}(t)) \tag{4.2}$$

Fig. 4.4(a) shows the calculated difference scattering signal upon LS $\rightarrow$ HS transition of $[Co(terpy)_2]^{2+}$ as a function of varying the axial Co-N bond length of the HS state. By increasing the difference between the axial Co-N bond of the LS structure and the axial Co-N bond of the HS structure ($\Delta d_{Co-Naxial}$), the magnitude of the negative signal at low Q increases accordingly. In particular, on a first order approximation, the difference scattering signal is found linearly dependent on the magnitude of the structural change giving rise to the signal. This induces a correlation between $d_{\text{Co-Naxial}}$ and the scaling factor α, when

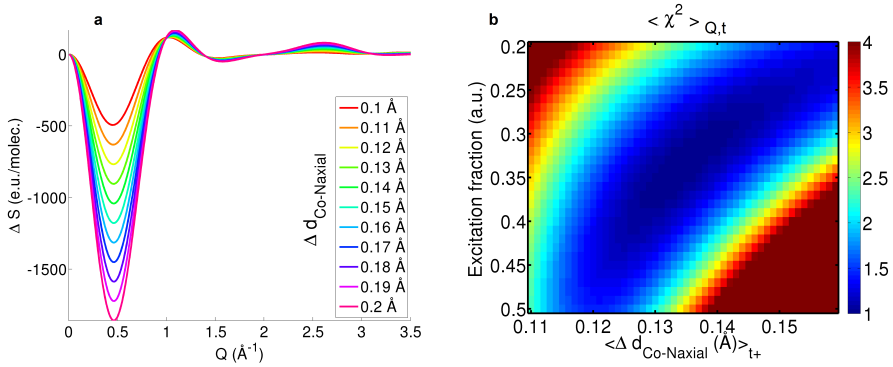

Figure 4.4: **(a)** Difference scattering signal from the LS $\rightarrow$ HS transition in $[Co(terpy)_2]^{2+}$ as a function of varying $\Delta d_{\text{Co-Naxial}}$ from 0.1 Å to 0.2 Å in step of 0.01 Å. **(b)** χ^2 obtained when fitting Eq. 4.4 to the experimental data as a function of the two free parameter α and $d_{\text{Co-Naxial}}$. The x-axis is the average change (upon LS $\rightarrow$ HS transition) of the axial Co-N bond distance over all the positive time delays t_+.

fitting the model described above (Eq. 4.1) to the data. This correlation is illustrated in Fig. 4.4(b).

In order to overcome this correlation, a guess on either the population kinetics or the structural dynamics has to be made. Based on the results from the SVD of the structural component of the signal (see above and Fig. 4.3(a)), the electronic state associated to the bond-elongated structure was assumed to be instantaneously populated and then the population to decay exponentially. α was therefore modelled as a IRF-broadened exponential decay with initial amplitude A (describing the initial excitation fraction) and time constant τ (describing the lifetime of the bond-elongated state). The expression can be written as:

$$\alpha(\mathrm{t}) = \mathrm{IRF}(\sigma_{\mathrm{IRF}}, \mathrm{t}) \otimes A e^{-\frac{\mathrm{t}-\mathrm{t}_0}{\tau}} \tag{4.3}$$

where t_0 (the arrival time of the laser pump) and σ_{IRF} (the width of the Gaussian IRF) were determined from the anisotropic part of the scattering signal (as detailed in Chapter 5 and in Paper III). The lifetime τ of the bond-elongated state was found 6.8 ps $\pm$ 0.8 ps from the analysis of a long-time range measurement presented in Paper III and this parameter was fixed in the analysis.

In summary, the model used to fit the entire set of scattering data is then:

$$\Delta S_{\text{model}}(Q,t) = \alpha(t)\Delta S_{\text{solute}}(Q, d_{\text{Co-Naxial}}(t)) + \beta(t)\Delta S_{\text{cage}}(Q) + \Delta \mathrm{T}(\mathrm{t})\left.\frac{\partial \mathrm{S}(\mathrm{Q})}{\partial \mathrm{T}}\right|_{\rho} \tag{4.4}$$

where α describes the time evolution of the excitation fraction as in Eq. 4.3. The free parameters are four: A (the initial excitation fraction), $d_{Co-Naxial}$, β, and ΔT. For each time point, β and ΔT are found nominally identical to the best-fit results obtained when using the model in Eq. 4.1 and shown in Fig. 4.2(b).

Note that, differently from the analysis presented in Paper III, in this analysis ΔS_{cage} keeps a scaling factor (β) different from that of ΔS_{solute}. As further detailed below, the two analysis yield the same results. This is expected since the close similarity between the solute and the cage dynamics seen in Fig. 4.2(b) justifies the assumption, used in Paper III, of a 1:1 correspondence between the cage and the solute signal.

Results

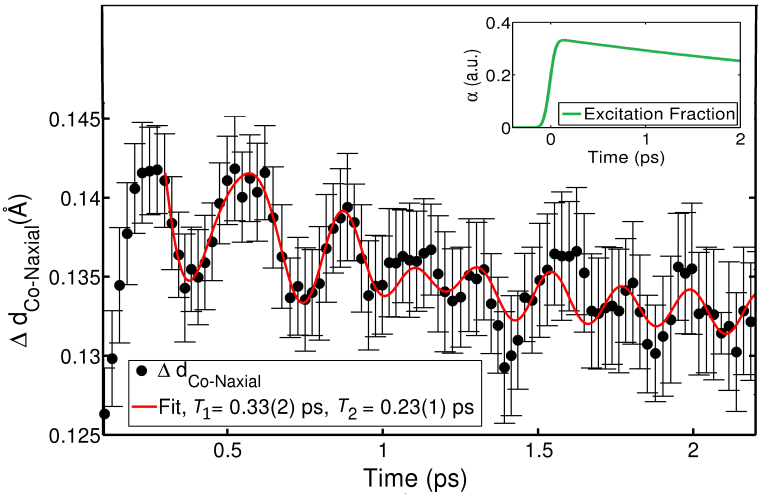

Figure 4.5: Changes, upon photoexcitation of solvated $[Co(terpy)_2]^{2+}$, of the axial Co-N bond length as a function of time. The red line shows a heuristic fit, incorporating sequential activation of first a T_1 ~0.33 ps mode and then a T_2 ~0.23 ps mode identified as, respectively, breathing- and pincer-like by direct comparison with DFT calculations. The two oscillators are superimposed on an exponential decay with time constant of 0.7 ps. The insert shows the time evolution of the excitation fraction, modelled as a IRF-broadened exponential decay with initial amplitude A = 0.34 and time constant τ = 6.8 ps, which is interpreted as the lifetime of the bond-elongated state. Adapted from Paper III.

On summary, the model in Eq. 4.4 was fit to the isotropic difference scattering signal measured upon photoexcitation of solvated $[Co(terpy)_2]^{2+}$. In the model, the structural changes are parametrized through $d_{\text{Co-Naxial}}$, the axial Co-N bond length of the HS state, and the temporal evolution of the excitation fraction α is described through an IRF-broadened exponential decay (Eq. 4.3).

Fig. 4.5 shows the changes in $d_{\text{Co-Naxial}}$ from the LS to the HS state as a function of time. The bond elongates at ultrafast time scale (< 300 fs) and then oscillates while reaching an equilibrium value which is approximately 0.1 Å shorter than the distance obtained immediately after excitation. After this relaxation, that happens on a ~ 1 ps time scale, $\Delta d_{\text{Co-Naxial}} = 0.13$ Å, from which the changes in equatorial distances can be calculated as $\Delta d_{\text{Co-Nequatorial}} = 0.07$ Å. These changes are slightly smaller than the DFT-predicted values; such a comparison can be found in Table 4.1.

The red line in Fig. 4.5 shows a heuristic fit to the data points. The model fit consists of two oscillators superimposed on an exponential decay. The model is further described in Paper III. Two oscillators were chosen after inspection of a Fourier transformation of the data points; moreover the residuals between the data and the fit were found relatively low compared to those obtained by using a single oscillator. The first oscillator is damped and the second driven, both with time constant of ~ 0.6 ps. The periods of the two oscillators are found ~ 330 fs and ~ 250 fs, respectively. These results are in agreements with the results obtained from the Fourier transform of the OSS (as seen in Fig. 4.3), indicating that the stretching of the Co-N bonds is mainly responsible for the observed coherent dynamics. The assignment of vibrational modes was made possible by a comparison with the DFT-calculated frequencies. As detailed in Paper III, the frequencies were assigned to a breathing-like and a pincer-like vibrational mode of the molecule. The former involves synchronous stretching of all six Co-N distances, the latter involves stretching of the axial Co-N bond accompanied with changes in the bite angle Nequatorial-Co-Naxial.

Finally, the inset of Fig. 4.5 shows the profile of the excitation fraction, as modelled in Eq. 4.3. A, the initial excitation fraction, was found ~ 34 %.

4.4 Discussion

The quantitative interpretation of time-resolved X-ray scattering data measured upon photoexcitation of $[Co(terpy)_2]^{2+}$ was made possible by the direct comparison with DFT and MD calculations and by the disentanglement of the structural dynamics and the population kinetics. An average ~ 0.09 Å elongation of the

six Co-N bonds was observed upon excitation, together with oscillations due to vibrational modes that involve the stretching of the Co-N bonds.

Since no information regarding the electronic configuration can be extracted from the scattering data, the results of this analysis need to be combined with the analysis of the X-ray spectroscopy measurements in order to achieve a complete picture of the relaxation pathway of the molecule. Pre-analysis of the kinetic profile of the k_β spectrum, which is sensitive to the spin state of the Co atom, has confirmed a fast population of the HS state, with a subsequent lifetime of $\sim$ 7 ps [76]. This allows the assignment of the the bond-elongated structure detected by the X-ray scattering to the HS state of the molecule.

Open questions remain about the early time kinetics. If the population of the HS state was instantaneous, as assumed in the analysis of the scattering data, the first oscillation would achieve its maximum amplitude half of its period ($\sim$ 0.17 ps) after the excitation event. On the contrary, the peak of the first oscillation is found about 0.26 ps after the excitation event. Such delay of the first outer turning point in metal-ligand stretch vibration following a LS $\rightarrow$ HS transition has been observed in the similar compound $[Fe(bpy)_3]^{2+}$ [77]. In $[Fe(bpy)_3]^{2+}$ the outer turning point is delayed by 50 fs due to a significant (120 fs) residence time in an MLCT state which has an equilibrium structure very close to that of the ground state. Based on the similarities of the systems and the observed dynamics, we interpret the delay in the Co-N stretch as a signature of a significant ($>$ 100 fs) residence time in one or more excited states with an equilibrium Co-N bond length distance much shorter than that of the HS state. The exact electronic nature of these intermediates can be elucidated by ultrafast X-ray and optical spectroscopy.

The first mode to be activated after the excitation, the breathing like mode, is found with an amplitude of $\sim$ 0.02 Å, which is 15 % of the initial elongation of the axial Co-N bond ($\sim$ 0.13 Å). This relatively low amplitude is possibly due to the following two reasons. First, the $\sim$ 100 fs delayed in the population of the HS state with respect to the excitation event could cause a broadening of this population in terms on the Co-N bond length. Secondly, the observed oscillations cannot be related one-to-one to the reaction (or configurational) coordinate of the spin transition. This reaction coordinate is not totally symmetric, due to and additional pseudo Jahn-Teller distortion in the LS state compare to the HS state and as reported for a similar complex, i.e. $[Fe(terpy)_2]^{2+}$ [78, 79, 80]. For this reasons the amplitude of the vibrations cannot be easily connected to the excess excitation energy.

The structural dynamics resulting from spin transitions of $[Fe(terpy)_2]^{2+}$ have been successfully explained by using the axial bond length and the bending angle of the ligand, (a parameter related to equatorial bond length parameter),

as reaction coordinates [81, 78]. With respect to $[Co(terpy)_2]^{2+}$, the observed activation, ~ 0.6 ps after excitation, of the pincer-like mode suggests the inclusion of the bending angle as a second normal coordinate in the investigation of the structural dynamics of the system. In order to do so, X-ray scattering data should access a larger Q range (i.e. a larger information content [20]) than that available in the measurements presented in this work.

Chapter 5

Anisotropic scattering: applications in XDS data analysis

This Chapter analyses anisotropic difference scattering signals measured at XFELs on transition metal complexes in water. Focus is given on the information that can be extracted from such signals and then used to improve the overall analysis of an XDS data set. The first part of the chapter describes the anisotropic signal measured in connection to the $[Co(terpy)_2]^{2+}$ experiment, the second part describes the analysis of the photoinduced dynamics of PtPOP.

5.1 Anisotropic signal due to ultrafast solvent dynamics

This section shows anisotropic difference scattering signals arising from the transient response of the water molecules to the electric field of the laser pulse. Such a signal is used to estimate the Instrument Response Function (IRF) of the experiment.

5.1.1 Ultrafast water dynamics

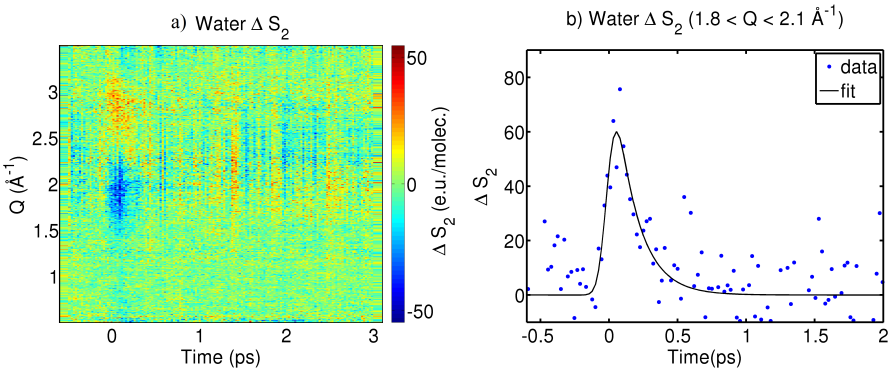

Figure 5.1: **a)** Anisotropic difference scattering signal $\Delta S_2(Q,t)$ measured upon photo-excitation of $[Co(terpy)_2]^{2+}$ in water. Such signal is expected to arise from the transient alignment of water molecules with the polarized laser pulse. **b)** Averaged value of the signal in a) in the interval 1.8 Å $< Q <$ 2.1 Å, where ΔS_2 is most dominant. The fit (black line) is a Gaussian function of width 0.05 ps $\pm$ 0.03 ps convoluted with an exponential decay with a time constant of 0.16 ps $\pm$ 0.08 ps (Eq. 5.1). The Gaussian is interpreted as the IRF of the experiment, as further detailed in the text. Adapted from Paper III.

Fig. 5.1(a) shows the anisotropic difference scattering signal measured upon photoexcitation of $[Co(terpy)_2]^{2+}$ in aqueous solution. The signal consists of a negative feature at around Q = 2 Å and a weaker positive feature at around Q = 3 Å, and occurs only during the first few hundred femtoseconds following the excitation event. Since the photoinduced MLCT transition of $[Co(terpy)_2]^{2+}$ does not have any specific polarization [59], the solute gives no contribution to the anisotropic difference scattering signal [29, 28]. The anisotropic signal is then assumed to arise from the interaction between the dipole moment of the water molecules and the linearly polarized electric field of the laser pulse [42].

Both measurements [42] and theoretical calculations [82] show that the nuclear response of water to an impulsive external electric field or, equivalently, to the electronic rearrangements of a solute molecule following photoexcitation comprises two contributions [40]:

- an ultrafast response due to the inertial motions of the solvent molecules. These initial motions are highly local such that each solvent molecule moves independently from the others. This response is reported to account

for more than 50 % of the signal arising from the solvation dynamics, to have a maximum at $\sim$ 20 fs, and to be damped in tens of femtoseconds [82].

- a slower component due to the diffusive reorientation of the water molecules, that has been reported to occur on the time scale of hundreds of femtoseconds [42].

Caster and Chang [83] measured the complete intermolecular dynamical spectrum of liquid water, by using optical Kerr effect spectroscopy. The frequency range was covered from 0-1200 cm^{-1}, thus comprising the diffusive, interaction-induced, translational, and librational motions of water. Fig. 5.2 shows the inverse Fourier transform of the frequency spectrum, i.e. a time-domain representation for all of the nuclear-coordinate intermolecular dynamics of liquid water. Three peaks occur at around 20, 60, and 200 fs and are assigned to the quantum beat interference of the librational and translational modes of liquid water. The diffusive reorientation lasts has a characteristic time scale of several picoseconds.

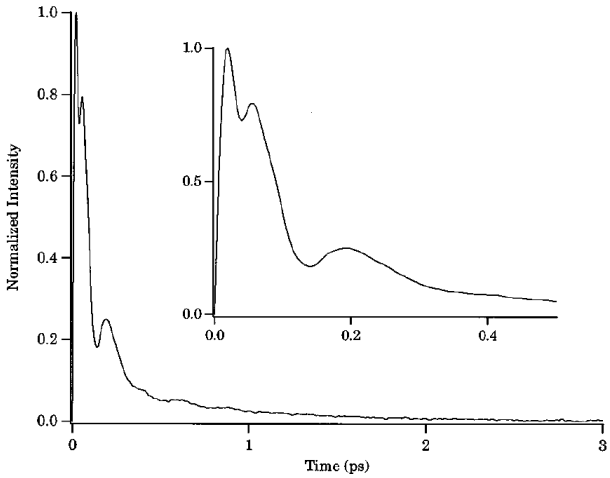

Figure 5.2: Nuclear-coordinate impulse-response function for the intermolecular dynamics of water. From [83].

These observations are consistent with the measured anisotropic difference scattering signal presented in Fig. 5.1(a) and shown in Fig. 5.1(b) as a function of time (after being averaged in the Q range where the signal is most intense). The signal in Fig. 5.1(b) and the curve in Fig. 5.2 are qualitatively alike. A

broadened single exponential decay with lifetime 0.16 ps ± 0.08 ps is fit to the data in Fig. 5.1(b). Due to the poor S/N ratio of the dataset, this time constant can be considered as a combination of the decay times of both the inertial and the diffusive motions. As a conclusion, the anisotropic signal in Fig. 5.1(a) is interpreted as a direct observation of the ultrafast water dynamics in response to the impulsive electric field of the laser pump.

5.1.2 Instrument response function

Since the transient water response to the laser field is (nearly) instantaneous [83], the measurement of such a response can be used to estimate the IRF of the experiment.

Assuming the IRF to be described by a Gaussian function, the signal in Fig. 5.1(b) is fit with a convolution between a Gaussian function and an exponential decay. In particular, the following expression is used for the fit:

$$r(t) = \int_{-\infty}^{+\infty} \frac{1}{\sigma\sqrt{2\pi}} e^{\frac{-(t-t_0-y)^2}{2\sigma^2}} H(y) A e^{-\frac{y}{\tau}} dy. \tag{5.1}$$

where σ is the width of the Gaussian function; A and τ are the amplitude and the lifetime, respectively, of the exponential decay; t_0 is the arrival time of the laser pulse; H the Heaviside step function and y is the integration variable. The best fit results for σ (0.05 ± 0.03 ps) and t_0 (-0.01 ± 0.03 ps) are assumed to describe the width and the central value, respectively, of the (Gaussian) IRF of the experiment.

The IRF can be considered the FWHM of the convolution of all the contributing factors to the time resolution of the experiment. Given that the time-jitter is corrected by the timing tool, the main factors that affect the time resolution are usually the laser and X-ray pulse length and the thickness of the liquid sheet. With respect to the data presented here, these values are $\sim$ 70 fs, $\sim$ 30 fs and $\sim$ 100 μm, respectively. Given a $\sim$ 1 fs per μm mismatch in the travel time of the laser and X-ray pulse in water, the thickness of the liquid sheet is assumed to contribute to the total IRF with a 100 fs FWHM. An heuristic estimate of the IRF is then given by:

$$\text{FWHM} = \sqrt{70^2 + 30^2 + 100^2} \quad \text{fs} = 126 \quad \text{fs} \tag{5.2}$$

From the value of σ found by fitting Eq. 5.1 to the transient response of water, a FWHM of 0.12 ps ± 0.07 ps can be calculated, in agreement with the estimate in Eq. 5.2.

5.1.3 Summary and Discussion

This sections shows that, upon photoexcitation of $[Co(terpy)_2]^{2+}$ in water through a non-polarized electronic transition, the measured anisotropic signal contains only contributions from the transient response of the water molecules to the laser field. Since the anisotropic transient response of the water molecules is nearly-instantaneous, the analysis of the anisotropic scattering results in the determination of the time-zero (the arrival time of the laser pulse at the sample) and of the IRF (that is found 0.12 ps $\pm$ 0.07 ps FWHM) of the experiment. These parameters are used in the analysis of the isotropic part of the data set, as described in chapter 4, and highly improve this analysis by facilitating the disentanglement of the many degrees of freedom involved in the ultrafast dynamics of $[Co(terpy)_2]^{2+}$. These methods are believed to be applicable to any time-resolved XDS experiment on solvated transition metal complexes, if the photoinduced structural changes of the solute are isotropic and thus the anisotropic signal arises only from the transient response of the solvent molecules to the laser field.

With respect to the ultrafast water dynamics observed in the experiment presented in this section, the time scale matches with the time scale that has been reported in literature from measurements of the optical 'Kerr effect' [83]. An atomistic interpretation of the underlying structural changes is yet not available. The picture that has emerged from optical experiments, simulations, and theory is that the ultrafast part of the water response can be viewed as arising from inertial motions (in particular translational and librational motions) [42, 82]. Since such motions have frequencies lying in the 60-600 cm^{-1} range (T = 50-500 fs) [83], time resolution of $\sim$ 10-20 fs should be achieved for a better insight of the water dynamics and for a structural interpretation of the signal. This would require jet thickness of around 10 μm, and the compression of both laser and X-ray pulses to single-femtosecond FWHM.

5.2 Combined structural analysis of isotropic and anisotropic scattering

This section presents the analysis of the time-resolved XDS data measured upon photoexcitation of PtPOP in water. The system and the experiment are described in Section 2.6.2.

5.2.1 Structural analysis of PtPOP

Fig. 5.3(a) and Fig. 5.3(c) show, respectively, the isotropic and anisotropic difference scattering signal measured upon photoexcitation of PtPOP in water at 395 nm. Both the data sets show clear oscillatory features as a function of time. As described in Section 2.6.2, the 395 nm laser pulse excites those molecules that already have a structural configuration corresponding to the equilibrium configuration of the singlet excited state. The excite state dynamics is therefore quenched and the 'hole' in the ground state population is created by selectively exciting solute molecules in a geometry different than the equilibrium configuration of the ground state. The observed oscillations are then expected to arise from the ground state structural dynamics.

5.2.1.1 Model

The temporal evolution of the ground state 'hole' population on the ground state PES leads to time-dependent changes in average Pt-Pt distance, which is the fundamental observable in the present experiment. Therefore, in order to describe the observed structural dynamics in the PtPOP data set, the photoinduced structural changes were parametrized through the changes in the Pt-Pt bond length. A series of geometries for the ground state of the molecule was constructed and used to model the difference scattering signal, as described in the following. DFT calculations were used as a starting point for the analysis[1]. The optimized DFT structure of the ground state has a Pt-Pt distance of $d_{\text{Pt-Pt}} = 2.92$ Å. This distance was varied up to ± 0.3 Å in steps of 0.01 Å. For every step, the $d_{\text{Pt-Pt}}$ was constrained and the other structural parameters were optimized through DFT calculations. The DFT structure of the excited state[2] yields $d_{\text{Pt-Pt}} = 2.75$ Å and this structure was not changed throughout the analysis.

From the singlet excited state, ISC occurs in ~ 10 ps [63]. The singlet and the triplet excited state PESs are found very similar [63], which accordingly implies structural similarities of these excited states. In this thesis, the singlet and the triplet excited state structure are assumed to be nominally identical. Therefore, in the framework of this analysis, the excited state population is constant on the time scale of the experiment.

The isotropic scattering signal was then modelled through the following expres-

[1] DFT calculations were carried out with the ASE-GPAW program package [84] utilizing the PBE exchange correlation functional in combination with the dzptzp basis set. [85]

[2] The calculation for the first triplet excited state were performed within spin-polarized DFT [85].

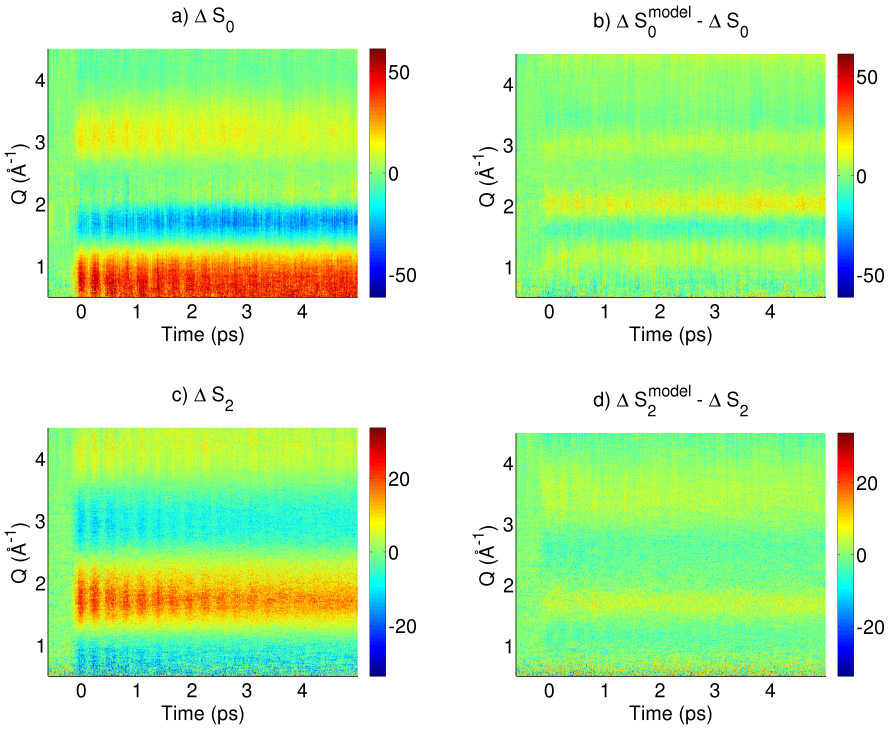

Figure 5.3: a) Isotropic difference scattering signal (ΔS_0) measured upon photoexcitation of PtPOP in water. b) Residuals after subtracting the model (Eq. 5.3) from the measured isotropic data. The model comprises a structural signal arising from the ground state dynamics and the contribution from the increase in the temperature of the bulk solvent. c) Anisotropic difference scattering signal (ΔS_2) upon photoexcitation of PtPOP in water. d) Residuals after subtracting the model (Eq. 5.4) from the measured anisotropic data set. The model includes only the contribution from the structural changes of the solute. The data are binned in 5 fs wide bins (and $\sim$ 100 difference scattering patterns were averaged in each).

sion:

$$\Delta S_0^{\text{model}} = \alpha \Delta S_0^{\text{solute}}(d_{\text{Pt-Pt}}(t)) + \Delta T(t) \frac{\partial S(Q)}{\partial T}\bigg|_{\rho} \tag{5.3}$$

where α is the excitation fraction, ΔT describes the increase in temperature and $\frac{\partial S(Q)}{\partial T}\Big|_{\rho}$ is the solvent differential, as introduced in Section 3.4. The free parameters in the fit are ΔT and $d_{\text{Pt-Pt}}$, while α was fixed at 2.6 %. The best

value for α was obtained from the inspection of the χ^2 values obtained by fitting Eq. 5.3 to the data as a function of different (locked) values of α and letting free all the other parameters. Additional details and the results of this analysis are presented in Fig. 5.4. After fitting Eq. 5.3 to the data, the obtained model was subtracted from the measured isotropic difference scattering yielding relatively low residuals, as shown in Fig. 5.3(b). The χ^2 was found 1.82.

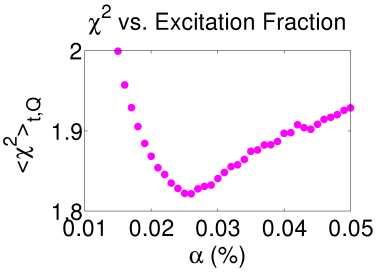

Figure 5.4: χ^2 obtained by fitting Eq. 5.3 to the isotropic difference scattering signal as a function of the excitation fraction α. α was varied in the range 0.015-0.05 (in step of 0.005) and, for each fixed value of α, Eq. 5.3 was fit to the data with $d_{\text{Pt-Pt}}$ and ΔT as free parameters. The reported χ^2 is the average over all time delays and Q points. The minimum χ^2 (1.82) is found at $\alpha = 0.026$, which was then kept constant throughout the analysis.

The anisotropic difference scattering signal was modelled through the following expression:

$$\Delta S_2^{model} = \alpha f(t) \Delta S_2^{\text{solute}}(d_{\text{Pt-Pt}}(t)) \tag{5.4}$$

where α is the excitation fraction (2.6 %) and $f(t)$ describes the temporal evolution of the magnitude of the anisotropic signal. $\Delta S_2^{\text{solute}}$ is calculated according to Eq. 3.8 and the transition dipole moment is assumed parallel to the Pt-Pt bond according to the polarization of the electronic transition at 395 nm [63]. Therefore, a cosine-square distribution of Pt-Pt distances about the laser polarization axis is assumed immediately after the excitation event. The initial amplitude of $f(t)$ is normalized to 1 and its temporal evolution is described by a biexponential decay, as obtained from the analysis of a long time range data set and detailed below (Section 5.2.3). The only free parameter in the fit is then d_{Pt-Pt}. Fig. 5.3(d) shows the residuals obtained after subtracting the model in Eq. 5.4 from the measured ΔS_2. The relatively low residuals indicate that the structural contribution alone can describe most of the anisotropic data set. The χ^2 was found 1.3.

5.2.1.2 Structural dynamics

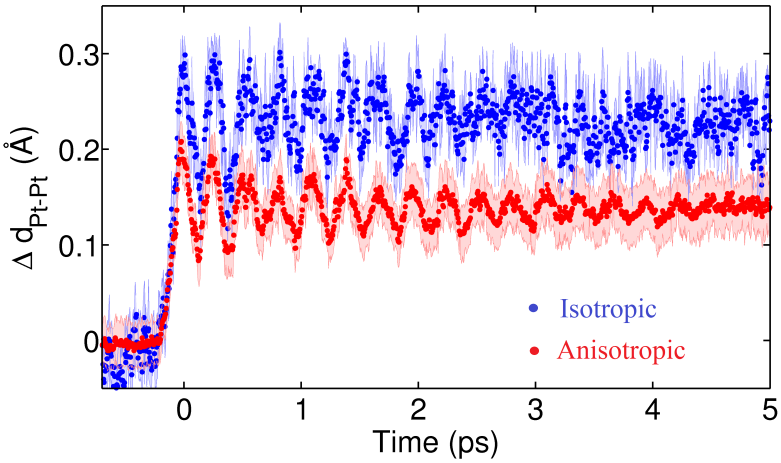

Figure 5.5: Changes in the Pt-Pt distance upon photoexcitation of PtPOP in water at 395 nm, as obtained from the analysis of the isotropic difference scattering signal (blue dots), and from the analysis of the anisotropic signal (red dots). The data have been smoothed by a 4-point nearest neighbour filter (20 fs); the uncertainties have been calculated following the procedure described in Paper III and are represented as shaded bars.

Fig. 5.5 shows the best fit results for the changes of $d_{\text{Pt-Pt}}$ upon photoexcitation as a function of time. The blue points show the results obtained from the analysis of the isotropic data set, the red points those obtained from the analysis of the anisotropic one. The time-dependent changes in average Pt-Pt distance are due to the evolution of the ground state 'hole' population on the ground state PES. Therefore, at each time point, $d_{\text{Pt-Pt}}$ represents the (average) Pt-Pt distance of the ground state hole population at that specific time point. Immediately after photoexcitation, $d_{\text{Pt-Pt}}$ increases and then shows oscillations that are damped on the few picosecond time scale. By inspection of the results obtained from the analysis of the isotopic dataset, the equilibrium $d_{\text{Pt-Pt}}$ after excitation is found approximately 0.23 Å longer than before the excitation. 0.23 Å is then the difference between the Pt-Pt bond length of the ground and the excited state structures and it is found in agreement with previous X-ray scattering measurements by Christensen *et al.* [14] (0.24 ± 0.06 Å) and slightly shorter than what reported by van Deer Veen *et al.* [65] with time-resolved X-ray spectroscopy (0.31 ± 0.05 Å).

As for $[\text{Co(terpy)}_2]^{2+}$, the magnitude of the difference scattering signal is to

a first approximation linearly dependent on the magnitude of the structural changes giving rise to the signal (in this case the changes in Pt-Pt bond length). In the model used to describe the anisotropic signal (Eq. 5.4), the changes in the Pt-Pt distance at each time point are therefore correlated to the value chosen for α, the excitation fraction, and to the value of $f(t)$ at that specific time point. Presuming that the assumption of a cosine-square distribution of Pt-Pt distances hold true, and if the same number of molecules contributed to the isotropic and anisotropic scattering, the results found for the value of $d_{\text{Pt-Pt}}$ (immediately after the excitation event) from the analysis of the isotropic and anisotropic data sets should be in quantitative agreement. On the contrary, the results in Fig. 5.5 indicate that the magnitude of the anisotropic signal is $1/3$ lower than that of the isotropic one. Following the above considerations, this discrepancy could, for instance, be due to the fact that 1 % of the population of molecules is excited without preferential orientation and therefore don't contribute to the anisotropic scattering signal. This will discussed further below.

5.2.1.3 Oscillatory structural signal

A broadened step function was fitted to each of the the time evolutions of $d_{\text{Pt-Pt}}$ shown in Fig. 5.5 and then subtracted from the respective data. The so obtained oscillatory structural signal (OSS) is shown in Fig. 5.6(a) for the isotropic data set and in Fig. 5.6(d) for the anisotropic one. A Fourier Transform (FT) of the two signals is shown in Fig. 5.6(b) and Fig. 5.6(e), respectively. One frequency is dominant in both the OSSs, corresponding to a period of approximately T = 284 fs. This value is in very good agreement with the frequency of the Pt-Pt stretching in the ground state as determined by optical studies (118 cm^{-1}/T = 0.28 ps [64, 61]).

Fig. 5.6(c) and Fig. 5.6(f) show a time-dependent FT of, respectively, the isotropic and anisotropic OSSs. The time-dependent FT is done with a 1.5 ps Hann window applied to the signal, by sliding the window from -0.1 ps to 4 ps. The plots show that the dominant mode is activated immediately after photoexcitation and that it decays on a few picoseconds time scale. The relatively long persistence of the coherence is in agreement with previous studies by Van der Veen *et al.*, who reported a $\sim$ 2 ps coherence decay time for the Pt-Pt stretch mode in the singlet state [61]. Van der Veen *et al.* assigned this behaviour to the harmonicity of the Pt-Pt oscillator and to the fact the the oscillator is not completely exposed to the solvent: the solute-solvent interaction occurs primarily along the axial coordination sites of the Pt atoms [61, 14].

Finally, it can be noticed that the the anisotropic OSS is less noisy than the isotropic OSS; the Fourier transformation of the former shows a slightly narrower

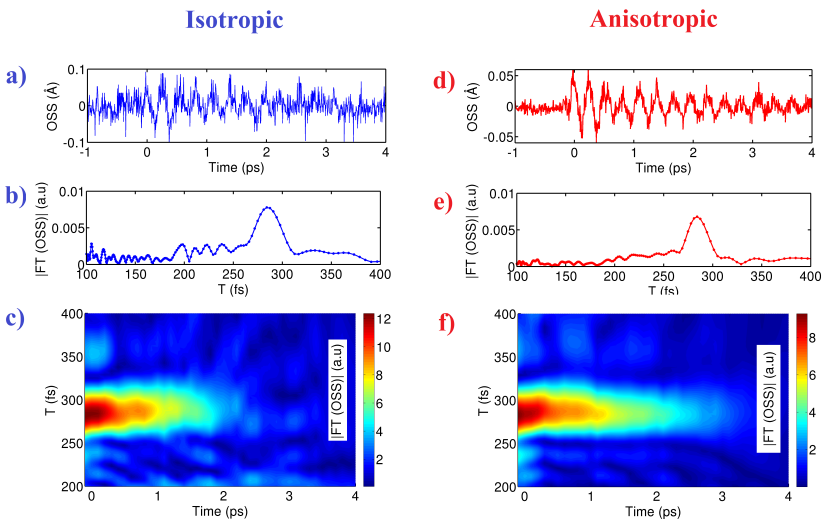

Figure 5.6: **(a)** Oscillatory structural signal (OSS) obtained from the analysis of the isotropic scattering signal upon photoexcitation of PtPOP. It will be called isotropic OSS. **(b)** Fourier Transform of the isotropic OSS shown in panel a). **(c)** Time-dependent Fourier transform of the isotropic OSS shown in panel a). **(b)** OSS obtained from the analysis of the anisotropic scattering signal upon photoexcitation of PtPOP. It will be called anisotropic OSS. **(e)** Fourier Transform of the anisotropic OSS shown in panel d). **(f)** Time-dependent Fourier transform of the anisotropic OSS shown in panel d).

peak in correspondence of the main frequency and in general less contributions from other frequencies. From visual inspection of the time-dependent FTs of the the two OSSs, the decay time of the main mode is slightly shorter in the isotropic data set than in the anisotropic one. These observations indicate that the coherence of the Pt-Pt stretching is enhanced in the anisotropic data set.

5.2.1.4 Energy deposition

Fig. 5.7 shows the temporal evolution of ΔT as obtained from the fitting of the isotropic difference scattering signal with the model in Eq. 5.3. On a few picoseconds time scale the water temperature increases approximately 0.25 K. Considering the excitation fraction (2.6 %) and the concentration of the sample (80 mM), there are approximately 23000 water molecules per each excited

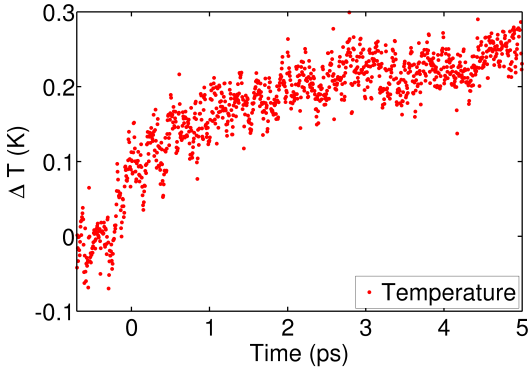

Figure 5.7: Fit results for ΔT, obtained when fitting Eq. 5.3 to the isotropic difference scattering signal measured upon photoexcitation of PtPOP in water (Fig. 5.3(a)). As detailed in the text, a ~ 0.25 K temperature increase occurring in the few ps after the excitation event cannot be explained by only single-photon absorption of the solute.

PtPOP molecule. Since the heat capacity of water is 4187 $J\ell^{-1}K^{-1}$, every PtPOP molecule would have to release 4.7 eV of energy to the solvent in order to explain the observed 0.25 K temperature increase. Since the 395 nm excitation wavelength corresponds to 3.1 eV, single-photon excitation of the solute cannot explain the observed temperature increase. A possible contribution from ISC (occuring on the $\sim$ 10 ps timescale [61]) would only be of the order of 1 eV, which is the energy difference between the singlet and the triplet excited states. The possible contribution from multi-photon absorption in the solvent is considered negligible, given that the laser fluency used in the experiment was smaller than 0.03 Jcm^{-2} [86]. The possibility of multi-photon absorption of the solute is considered further below.

5.2.2 Enhanced structural information in the anisotropic contribution

This section shows some of the results obtained from a rank-5 SVD of the measured data and the residuals shown in Fig. 5.3.

The black data points in Fig. 5.8(a) and Fig. 5.8(b) show the singular values $S_{i,i}$ (with i = 1,2,..,5) obtained from a rank-5 SVD of, respectively, the isotropic and anisotropic difference scattering signals. The red data points in the same plots show the singular values from a rank-5 SVD of the residuals for the two data

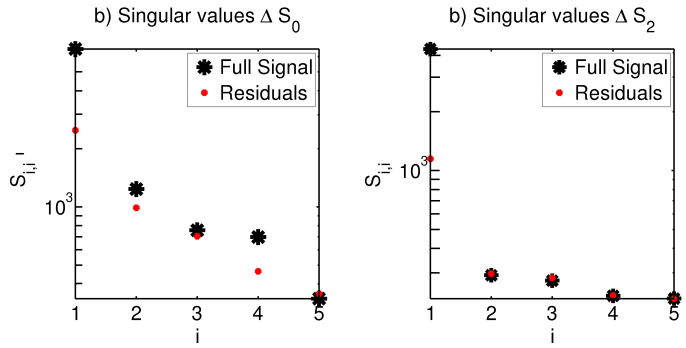

Figure 5.8: **(a)** The black dots are the singular values obtained from a SVD of the measured isotropic difference scattering signal upon photoexcitation of PtPOP (ΔS_0 in Fig. 5.3(a)). The red dots are the singular values obtained from a SVD of the residuals ($\Delta S_0 - \Delta S_0^{\mathrm{model}}$) shown in Fig. 5.3(b). **(b)** The black dots are the singular values obtained from a SVD of the measured anisotropic difference scattering signal upon photoexcitation of PtPOP (ΔS_2 in Fig. 5.3(c)). The red dots are the singular values obtained from the SVD decomposition of the residuals ($\Delta S_2 - \Delta S_2^{\mathrm{model}}$) shown in Fig. 5.3(d). The singular values are also reported in Table 5.1.

sets. The singular values are also reported in Table 5.1. By assuming that each data set is fully described by the first five SVD-components, the contribution c of each component i to the data can be evaluated as:

$$c_i = \frac{S_{i,i}}{\sum_{i=1}^{5} S_{i,i}} \tag{5.5}$$

and $\sum_{i=1}^{5} c_i = 1$. From the singular values of the SVD of the isotropic data set, it is obtained $c_1 = 0.68$; $c_2 = 0.13$, $c_3 = 0.08$, $c_4 = 0.07$ and $c_5 = 0.04$. Therefore, the first component describes 68 % of the variations of the signal and the 2nd, 3rd and 4th component are also relevant for the complete description of the isotropic scattering signal. The singular values obtained from the SVD of the anisotropic data set yield $c_1 = 0.8$; $c_2 = 0.06$, $c_3 = 0.06$, $c_4 = 0.04$ and $c_5 = 0.04$. Therefore, 80 % of the anisotropic data set is described by the first component, which is also the one mainly described by the model, as detailed further below.

The SVD-components of the isotropic data set are shown in Fig. 5.9(a). For this data set, the SVD-components cannot be individually assigned to physical properties of the system and they are most likely a mixture of structural and solvent contributions. The time evolution of the amplitudes of the components

	$S_{1,1}$ $\cdot 10^{-3}$	$S_{2,2}$ $\cdot 10^{-3}$	$S_{3,3}$ $\cdot 10^{-3}$	$S_{4,4}$ $\cdot 10^{-3}$	$S_{5,5}$ $\cdot 10^{-3}$
ΔS_0	6.57	1.24	0.76	0.70	0.36
$\Delta S_0^{\text{model}}$ - ΔS_0	2.45	1.03	0.72	0.40	0.35
ΔS_2	4.18	0.29	0.27	0.23	0.22
$\Delta S_2^{\text{model}}$ - ΔS_2	1.08	0.29	0.27	0.23	0.22

Table 5.1: Singular values obtained from a rank-5 SVD of the isotropic (ΔS_0) and anisotropic (ΔS_2) difference scattering signal and of the respective residuals: $\Delta S_0^{\text{model}}$ - ΔS_0 and $\Delta S_2^{\text{model}}$ - ΔS_2. The singular values are also plotted in Fig. 5.8.

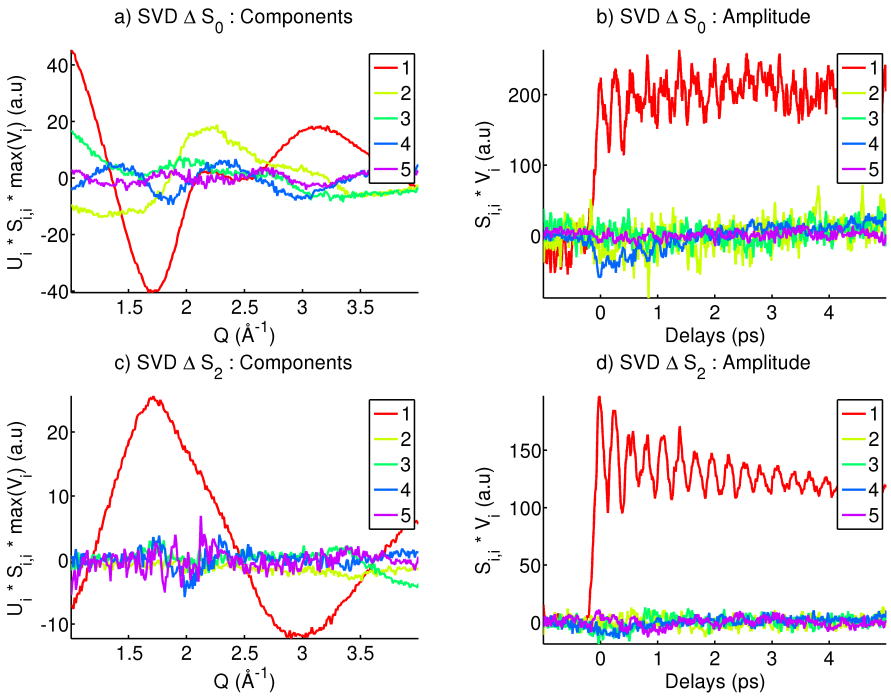

Figure 5.9: **(a)-(b)** Results of a 5-rank SVD analysis on ΔS_0, shown in Fig. 5.3(a). **(c)-(d)** Results of a 5-rank SVD analysis on ΔS_2, shown in Fig. 5.3(c).

is shown in Fig. 5.9(b); at least two of them show oscillatory behaviour. The SVD-components of the anisotropic data set and their amplitudes are shown in Fig. 5.9(c) and Fig. 5.9(d), respectively. The first SVD-component can be assigned to the structural signal. The other components (i=2,3,4,5) are noisy;

component 4 and 5 are mainly contributing at around Q = 2 Å and at early time points. These features resembles the signatures observed for the impulsive response of water to the electric field of the laser (see Section 5.1), indication that they may be due to the 'Kerr effect' [83].

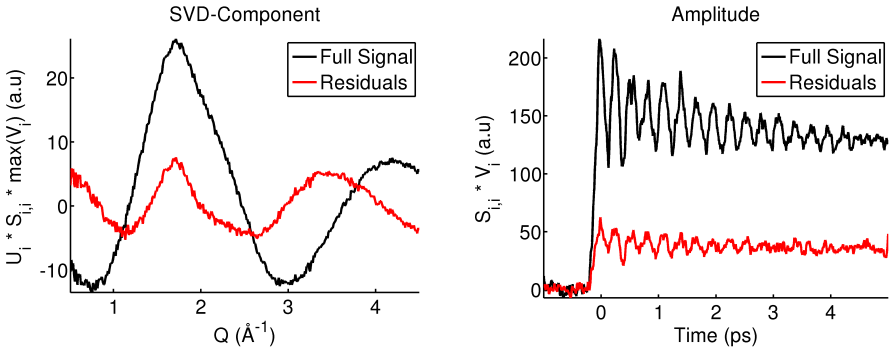

Figure 5.10: **(a)** First SVD component of the anisotropic difference signal (black) and of the respective residuals (red). The latter is 25 % of the former, according to the singular values in Table 5.1. The first SVD-component of the anisotropic signal is interpreted as structural signal. **(b)** Temporal evolution of the magnitude of the SVD-components shown in panel a). The structural signal and the residuals shows similar dynamics, indicating incompleteness of the model used to describe the data.

Finally, Fig. 5.10(a) shows the first SVD-component obtained from the SVD of ΔS_2 and the first SVD-component obtained from the SVD of the associated residuals ($\Delta S_2^{\text{model}}$ - ΔS_2). Fig. 5.10(b) shows a similar temporal behaviour for the amplitude of the two components, indicating that the residuals contain signal arising from the structural changes in the solute or from changes in geometry and rearrangements of the solvent molecules in close proximity to the solute, since, as seen for $[Co(terpy)_2]^{2+}$, the temporal modulations of the cage signal can follow closely those of the solute. If the residuals are an indication of changes occurring in the solvation shell, a cage term should be included in the analysis, as discussed further below. From inspection of the singular values reported in Table 5.1, the first component of the residuals describes 75 % of the first component of the anisotropic signal. Since the structural contribution to the anisotropic scattering is fully described by the first SVD component of the data set, as described above, it can be concluded that ΔS^{solute} (in Eq. 5.3 and Eq. 5.4) describes 75 % of the structural contribution present in the XDS data set.

5.2.3 Decay of anisotropy

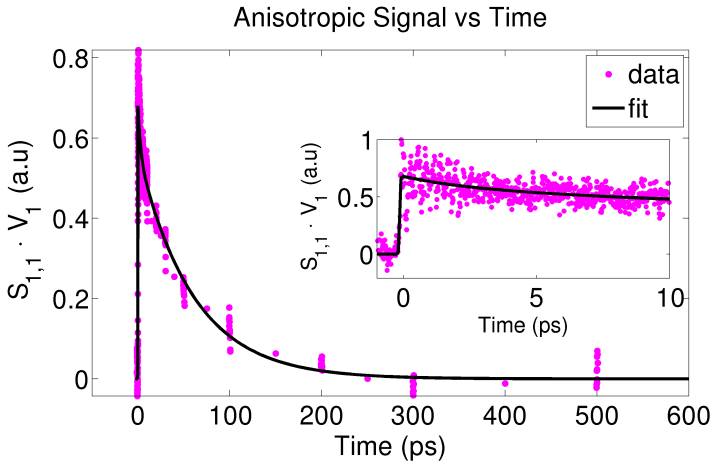

Figure 5.11: Amplitude of the first SVD-component obtained from a 5-rank SVD analysis on the anisotropic scattering signal measured up to 1 μs. A broadened exponential decay is fit to the data (black line). The first time constant (3 ps $\pm$ 2 ps) is most likely connected to the vibrational cooling in the ground state PES, while the second time constant (0.06 ns $\pm$ 0.01 ns) is interpreted as the rotational correlation time of PtPOP in water.

The rotational dephasing time of the laser induced orientation in the excited state and in the 'hole' population of PtPOP molecules could be extracted from a long time range measurement (up to 1 μs). In this analysis, it is assumed that the molecule has the same rotational correlation time in its ground and excited states. The anisotropic part of the data set was analysed through SVD, since the first SVD-component have been interpreted as the structural signal from the molecule. Fig. 5.11 shows the temporal evolution of the first so-obtained SVD-component (magenta points). The black line is a fit of the data with a broadened biexponential decay. A single exponential decay could not describe the signal. 20 % of the signal was found to decay with a time constant of 3 ps $\pm$ 2 ps; while 80 % of the signal was found to decay with a time constant of approximately 0.06 ns $\pm$ 0.01 ns. The latter is interpreted as the rotational correlation time of the PtPOP molecule in water. Using the Stokes-Einstein-Debye model [87], the rotational correlation time of a sphere can be described as:

$$\tau_r = \frac{4\pi\eta r^3}{3K_B T} \tag{5.6}$$

where η is the viscosity of water, K_B the Boltzman constant, T the temperature

and r the radius of the sphere. Approximating the PtPOP molecule to a sphere, and taking r as half the longest inter-atomic distance in the PtPOP molecule (r = 4 Å), the rotational correlation time at room temperature can be calculated as 50 ps. This value is in agreement with the $\sim$ 60 ps found in this analysis. The interpretation of the first time constant is tentative, but it is most likely connected to the vibrational relaxation in the ground state PES.

5.2.4 Summary and Discussion

The results of the analysis presented in this Section lead to observations that can be summarized as follows.

- The anisotropic scattering signal is dominated by the signal arising from the structural changes in the solute and in the solvation shells surrounding the solute. Since the model in Eq. 5.4 describes 75 % of the anisotropic data set, $\Delta S_{\mathrm{solute}}$ cannot describe all the structural changes occurring in the solute and/or a cage contribution should be included in the model.
- Femtoseconds coherent dynamics arising from the Pt-Pt stretching in the ground state PES is observed in both the isotropic and the anisotropic data sets with a period of T = 284 fs and a damping time on the picosecond time scale. The isotropic OSS is more noisy and shows a slightly shorter coherence decay time with respect to the anisotropic OSS. This indicate that the anisotropic signal is highly sensitive to the Pt-Pt stretching.
- Assuming a cosine-square distribution of the Pt-Pt distances after the excitation event, the discrepancy between the magnitude of the isotropic and the anisotropic signal indicates that part of the molecules are excited through an electronic transition not polarized along the Pt-Pt bond length.
- The temperature increase, obtained by fitting of the isotropic data set with the model in Eq. 5.4, suggests incompleteness of the model used to describe the structural changes (ΔS_{solute}) and/or multi-photon excitation of the solute.

From these observations, the strategy for the second iteration of the analysis can be outlined as follows.

First, structural refinement should be attempted by comparing a set of models to the measured data. New DFT calculations with the BLYP functional have shown a better agreement with previous studies than those used in this analysis [85]. Starting from these new DFT structures, several models for the ground

and the excited state of PtPOP can be constructed by exploring more than one coordinate in the structural parameters space [65].

With respect to the fact that no cage contribution was included in the analysis, this choice is consistent with previous analysis by Christensen *et al.* [14], who, starting from the observation that no solvatochromism is observed in optical studies, concluded that there is no axial coordination of solvent molecules with the Pt atoms, neither in the ground state nor the excited state. The contribution to the scattering signal from the solute-solvent changes is thus expected to be negligible. However, Van der Veen *et al.* [61] states that there must be a transient solute-solvent interaction through which the excess excitation energy from the singlet state can be dissipated. This is due to the fact the the Pt-Pt stretch is the lowest-frequency mode in PtPOP, therefore IVR is excluded. They then conclude that a Pt-H interaction should be possible along the axial coordination site of the Pt atoms. Accordingly to this scenario, the changes in solute-solvent distances would also be anisotropic and thus contribute to the anisotropic scattering signal. In order to simulate an anisotropic cage signal, the formalism presented in Paper I, based on the Debye equation and on RDFs, should be expanded: the second-order term in the expansion of Legendre polynomials of the scattering signal can be calculated through spacial (angle-resolved) distribution function, that can be obtained from MD or Quantum Mechanics/Molecular Mechanics (QM/MM) simulations [88, 35].

The second iteration of the analysis should also include a second population created by multi-photon absorption in the solute, which is most likely happening though transitions less oriented with respect to the Pt-Pt distance. The existence of such transitions in the absorption spectrum at around 200 nm is well documented in the literature [63].

A tentative new model can then be written as:

$$\Delta S_0^{\text{model}} = \alpha(t)\Delta S_0^{\text{str.}}(d^{sp}_{\text{Pt-Pt}}(t)) + \beta(t)\Delta S_0^{\text{str.}}(d^{mp}_{\text{Pt-Pt}}(t)) + \Delta T(t)\left.\frac{\partial S(Q)}{\partial T}\right|_{\rho} \quad (5.7)$$

$$\Delta S_2^{\text{model}} = \gamma(t)f(t)\Delta S_2^{\text{str.}}(d^{sp}_{\text{Pt-Pt}}(t)) \quad (5.8)$$

where $\Delta S^{str.}$ comprises the structural changes in both solute and surrounding solvation shells ($\Delta S^{str.} = \Delta S^{solute} + \Delta S^{cage}$). $d^{sp}_{\text{Pt-Pt}}$ describes the structural changes with respect to the equilibrium configuration of the excited state populated through single-photon (sp) absorption, and $d^{mp}_{\text{Pt-Pt}}$ describes the structural changes with respect to the equilibrium configuration of the state populated through multi-photon (mp) excitation. α and β are the corresponding excitation fractions and their temporal behaviour are inter-dependent. γ describes the amount of molecules contributing to the anisotropic scattering signal, and

its initial amplitude and temporal behaviour depends on the polarization of the *mp* transition.

The model for the isotropic signal in Eq. 5.7 comprises multiple free parameters, that would probably show correlations in the fitting of the data. Fewer degrees of freedom are involved in the description of the anisotropic data set through Eq. 5.8, since the anisotropic signal is dominated by the Pt-Pt stretching (a strongly-anisotropic mode in the molecule) arising from a highly-polarized transition. The feasibility of such a complex analysis is due to the fact that the information obtained from quantitative analysis of the anisotropic signal and from side-by-side comparison of the isotropic and anisotropic signal can be used to constrain some of the multiple parameters involved in the dynamics of Pt-POP.

As a conclusion, an experiment can be designed such that photoselection enhances specific structural information in the anisotropic scattering signal. This information can make it possible to disentangle the many degrees of freedom involved in the analysis of the full scattering signal arising from a disordered system. Based on this, the quantitative interpretation of the anisotropic signal will improve and deliver information that can greatly benefit the overall interpretation of high-content scattering data from transition metal complexes in solution.

Chapter 6

Summary and Conclusion

This thesis presents the use of time-resolved X-ray scattering experiments on transition metal complexes in solution at XFELs.

Time-resolved XDS at synchrotron sources was shown to be an excellent tool for the structural characterization of excited states of molecules. In this thesis, focus was given to the development and application of methods for the analysis and interpretation of time-resolved XDS data at XFELs. First, corrections of 2D scattering patterns for artefacts arising from the shot-to-shot fluctuations characteristic of XFELs sources and non-linearity of the detector were successfully achieved through 2D-SVD. Secondly, since asymmetric effect caused by photoselection can be observed at the femtosecond time scale of XFELs, the azimuthal integration of the 2D scattering patterns applied to synchrotron data was substituted with the extraction of 1D isotropic and anisotropic difference scattering curves. Quantitative interpretation of both contributions was achieved through modelling.

The aforementioned methods were first applied to investigate the dynamics of $[Co(terpy)_2]^{2+}$ in aqueous solution upon photoinduced SST. Ultrafast elongation of the Co-N bond length was observed followed by two oscillations with a period of T $\sim$ 0.33 ps and T $\sim$ 0.23 ps arising from stretching of the Co-N bond lengths and decaying on a sub-picosecond time scale. The observed vibrational modes were assigned to a breathing-like and a pincer-like mode, respectively,

through direct comparison with DFT calculations. The bond-elongated structure was assigned to the HS state of the molecule and found with a lifetime of $\sim$ 7 ps. MD simulations described most of the structural changes occurring in the first solvation shell of $[Co(terpy)_2]^{2+}$. As a second result obtained in this thesis, the anisotropic scattering signal provided access to anisotropic solvent and solute dynamics induced by the linearly polarized laser field. The impulsive response of water molecules to the electric field of the laser pulse was observed for the first time with time-resolved XDS. Valuable informations such the time-zero and the IRF of the experiment were extracted from this anisotropic signal and improved the overall XDS analysis by diminishing the number of degrees of freedom involved in the description of the isotropic part of the data. Upon geometry- and orientation-selective excitation of PtPOP in water, coherent vibrational dynamics arising from the Pt-Pt stretching in the ground state PES ($T \sim 0.23$ ps) was found to be enhanced in the anisotropic part of the scattering signal. This structural sensitivity of the anisotropic signal facilitated the disentanglement of the different electronic and nuclear degrees of freedom involved in the photoinduced dynamics of PtPOP. As a general result, alignment-enhanced information proved to benefit the interpretation of time-resolved XDS data on solvated transition metal complexes.

Collectively, the application of the methods described in this thesis provides direct access to information on structural dynamics and solvation response of transition metal complexes in solution at the femtosecond time scale. Furthermore, with adequate prior knowledge, information on electronic state kinetics can also be gained. Thus, the excited state nature of transition metal complexes can be understood at the intrinsic time scale of atomic motions.

6.1 Outlook

This thesis presents a development towards a complete and coherent framework for the analysis and interpretation of time-resolved XDS data sets on solvated metal complexes collected at XFELs. Currently, the average time from acquisition to publication of such results is three years. With the upcoming European XFEL and the upgrading of LCLS, the repetition rate will enter the MHz regime, thus allowing the acquisition of orders of magnitude larger data sets in the same short time. Establishing standardized methods for efficiently analysing these large XDS data sets is therefore essential for the full realization of the method. This would also make time-resolved XDS more accessible and consequently enlarge the number of the scientific questions that can be posed and answered.

One of the major challenge in the study of ultrafast photochemical and -physical

processes is understanding the interplay between many coupled electronic and nuclear (inter- and intra-molecular) degrees of freedom. The combination of XDS with other X-ray or optical techniques helps the disentanglements of these different contributions, particularly the separation of population kinetics of electronic states and structural dynamics. At the European XFEL, the X-ray energy range will be increased up to 21 keV allowing the access to a larger region of momentum-space compared to current XFELs studies. In this way, the amount of information content will be increased and enable detailed studies of the structural dynamics.

Another challenge is achieving a deeper understanding of solvation processes, since they can greatly affect the outcome of a chemical reaction. Both polar and non polar solvation effect have been explained in the past mostly with continuum models [36, 38, 89]. However, continuum models cannot provide a direct insight into the local changes of the solvation shell, but mostly look at averaged quantities. QM/MM has emerged as a tool for providing an atomistic interpretation of the solvation processes [35]. XDS observables can directly relate to such calculations, but so far experimental characterization of solvation dynamics has remained a challenge, mainly due to the difficulty in achieving the requisite time resolution. This difficulty can be overcome at XFELs, facilitating new insights into complex and dynamical solvation effects.

Appendix A

Calculation of ΔS

As detailed in Chapter 2, the scattering signal arising from a molecular species s can be written as:

$$S^s(Q, \cos\theta_Q) = S_0^s(Q) - P_2(\cos\theta_Q) S_2^s(Q) \tag{A.1}$$

where S_0^s and S_2^s are the isotropic and anisotropic contribution, respectively. Eq. 2.13 can be written so that:

$$S_0^s = c_0^s s_0^s \tag{A.2}$$

where c_0^s is the 0-order rotational coefficient, and

$$s_0^s(Q) = \sum_{i,j}^{N_s} f_i(Q) f_j(Q) \frac{sin(Qr_{ij})}{Qr_{ij}}. \tag{A.3}$$

Similarly, Eq. 2.14 is rewritten as:

$$S_2^s = c_2^s s_2^s \tag{A.4}$$

where c_2^s is the 2-order rotational coefficient , and

$$s_2^s(Q) = \sum_{i,j}^{N_s} f_i(Q) f_j(Q) P_2(\cos\theta_{ij}) j_2(Qr_{ij}) \tag{A.5}$$

In these formulae, N_s is the number of atoms of the specific molecular species.

Before the excitation event, the molecules are in the ground state and randomly oriented in solution. Assuming that there is only one molecular species in solution, the scattering signal before the excitation event (S^{off}) will be only isotropic:

$$S^{off} = s_0^{gs}, \tag{A.6}$$

where s_0^{gs} is the scattering signal arising from the ground state population and $c_0^{gs} = 1$ (normalization to the total population). The scattering signal after the excitation event (S^{on}) comprises contributions from both the excited state ensemble (es) of molecules and the ensemble of the molecules that remain in the ground state (labelled un, as un-excited), both of them being oriented ensemble with respect to the laser polarization axis,:

$$S^{on} = S^{es} + S^{un} \tag{A.7}$$

If the excited state population has a cosine-squared distribution about the laser polarization axis, $c_2 = 2c_0$ and:

$$S^{es} = f^{es} s_0^{es} - 2 f^{es} P_2 s_2^{es} \tag{A.8}$$

where f^{es} is the excite state population fraction. On the contrary, the initial distribution of the transition dipole moments of the unexcited population is the complement of that of the excited state (therefore proportional to 1 - $\cos^2$). The scattering signal arising from this species can be expressed as [28]:

$$S^{un} = (1 - f^{es}) s_0^{un} + 2 P_2 f^{es} s_2^{un} \tag{A.9}$$

Eq. A.6 can be rewritten as:

$$S^{off} = f^{es} s_0^{gs} + (1 - f^{es}) s_0^{gs} \tag{A.10}$$

and since $s_0^{un} = s_0^{gs}$ and $s_2^{un} = s_2^{gs}$, the difference scattering signal results:

$$\Delta S = S^{off} - S^{on} = f^{es} (\Delta s_0 - 2 P_2 \Delta s_2) \tag{A.11}$$

where:

$$\Delta s_0 = s_0^{es} - s_0^{gs} \tag{A.12}$$

and

$$\Delta s_2 = s_2^{es} - s_2^{gs} \tag{A.13}$$

This expression is valid immediately after the excitation event, where the complementarity of the distributions of the excited and un-excited species is assumed (Eq. A.9). The orientations of the un-excited sample and of the excited population will evolve in time with different rotational correlation time, if the

respective moments of inertia are different. The time-dependent difference scattering signal (considering static population of the excited state) can be written as:

$$\Delta S(t) = f^{es}\Delta s_0 - P_2\Delta S_2(t) \tag{A.14}$$

In this expression, Δs_0 is as in Eq. A.12, while the anisotropic difference scattering is:

$$\Delta S_2(t) = c_2^{es}(t)s_2^{es} - c_2^{un}(t)s_2^{un}(t) \tag{A.15}$$

where c_2^{es} and c_2^{un} describe the time evolution of the angular distributions of the two species.

Appendix B

2D-SVD

In Chapter 3, a series of Off-Images are analysed through a rank-6 2D-SVD. The amplitude of two of the so-obtained SVD-components is found correlated to beam diagnostics. Such SVD-components are therefore removed from the data set. The so-obtained corrected Off-Images are analysed a second time through a rank-6 2D-SVD. Fig. B.1 and Fig.B.1 show the obtained results. The corrected Off-images don't show any fluctuations dependent on X-ray intensity or energy.

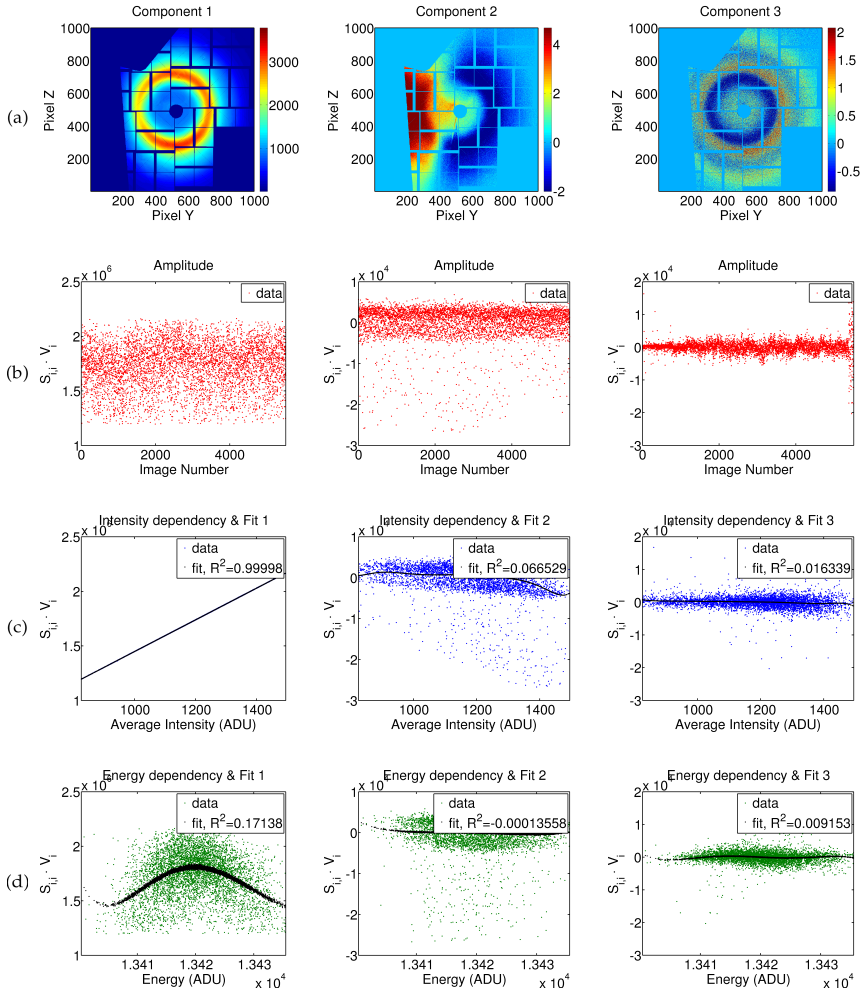

Figure B.1: Results of a SVD of Off-images previously corrected for artefact correlated to X-ray intensity and energy, as detailed in Section 3.2. (a) Components 1:3 visualized on the CSPAD. Each component U is multiplied by its mean amplitude. b) Amplitude of the component as a function of acquisition time. c) Amplitude of the components against X-ray intensity (blue dots) and polynomial fit (black dots). d) Amplitude of the components against the electron beam energy (from which the X-ray energy could be calculated) (red dots) and polynomial fit (black dots).

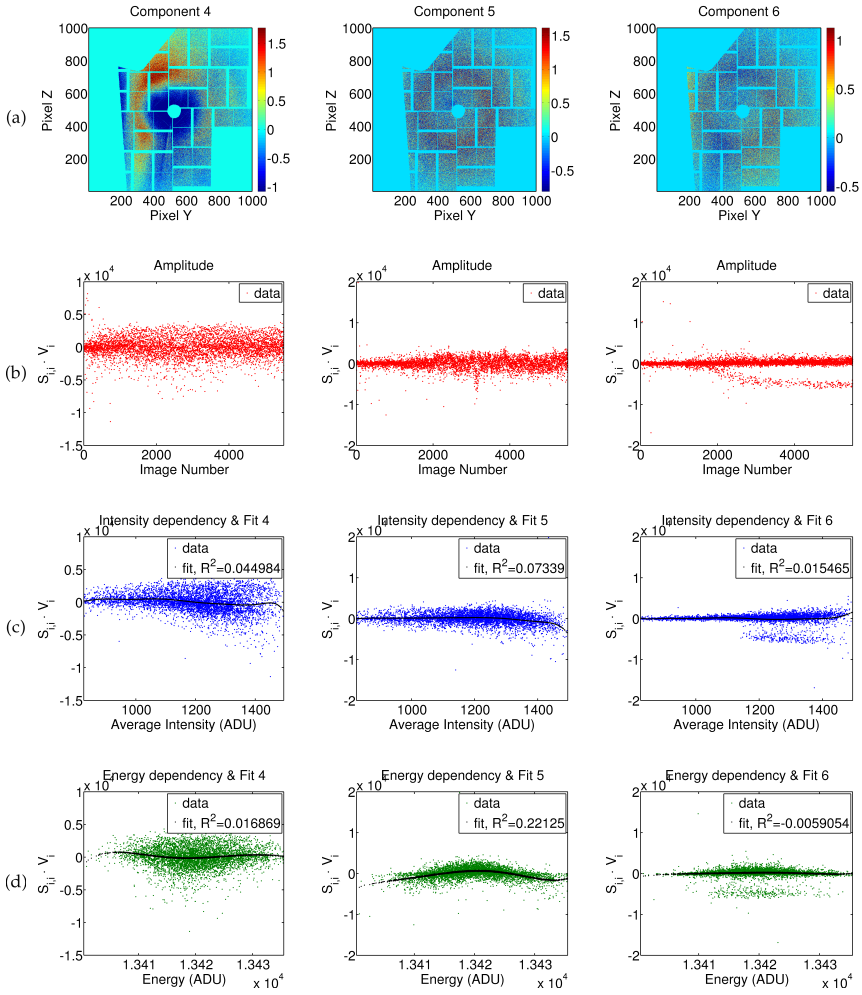

Figure B.2: Results of a SVD of Off-images previously corrected for artefact correlated to X-ray intensity and energy, as detailed in Section 3.2. (a) Components 4:6 visualized on the CSPAD. Each component U is multiplied by its mean amplitude. b) Amplitude of the component as a function of acquisition time. c) Amplitude of the components against X-ray intensity (blue dots) and polynomial fit (black dots) d) Amplitude of the components against the electron beam energy (from which the X-ray energy could be calculated) (red dots) and polynomial fit (black dots).

Bibliography

[1] A. H. Zewail, "Femtochemistry. past, present, and future," *Pure Appl. Chem.*, vol. 72, no. 12, pp. 2219–2231, 2000.

[2] T. S. Rose, M. J. Rosker, and A. H. Zewail, "Femtosecond real-time observation of wave packet oscillations (resonance) in dissociation reactions," *The Journal of Chemical Physics*, vol. 88, no. 10, pp. 6672–6673, 1988.

[3] H. T. Lemke, C. Bressler, L. X. Chen, D. M. Fritz, K. J. Gaffney, A. Galler, W. Gawelda, K. Haldrup, R. W. Hartsock, H. Ihee, J. Kim, K. H. Kim, J. H. Lee, M. M. Nielsen, A. B. Stickrath, W. Zhang, D. Zhu, and M. Cammarata, "Femtosecond x-ray absorption spectroscopy at a hard x-ray free electron laser: Application to spin crossover dynamics," *The Journal of Physical Chemistry A*, vol. 117, p. 735–740, 2013.

[4] T. C. B. Harlang, Y. Liu, O. Gordivska, L. A. Fredin, C. S. Ponseca, P. Huang, P. Chábera, K. S. Kjær, H. Mateos, J. Uhlig, R. Lomoth, R. Wallenberg, S. Styring, P. Persson, V. Sundström, and K. Wärnmark, "Iron sensitizer converts light to electrons with 92 % yield," *Nature Chemistry*, vol. 7, no. 11, pp. 883–889, 2015.

[5] M. K. Nazeeruddin, E. Baranoff, and M. Grätzel, "Dye-sensitized solar cells: A brief overview," *Solar Energy*, vol. 85, no. 6, pp. 1172 – 1178, 2011.

[6] E. Fujita, "Photochemical carbon dioxide reduction with metal complexes," *Coordination Chemistry Reviews*, vol. 185–186, pp. 373 – 384, 1999.

[7] J. D. Blakemore, R. H. Crabtree, and G. W. Brudvig, "Molecular catalysts for water oxidation," *Chemical Reviews*, vol. 115, no. 23, pp. 12974–13005, 2015.

[8] V. Fernandez-Moreira, F. L. Thorp-Greenwood, and M. P. Coogan, "Application of d6 transition metal complexes in fluorescence cell imaging," *Chem. Commun.*, vol. 46, pp. 186–202, 2010.

[9] M. R. Arkin, E. D. A. Stemp, R. E. Holmlin, J. K. Barton, A. Hörmann, E. J. C. Olson, and P. F. Barbara, "Rates of dna-mediated electron transfer between metallointercalators," *Science*, vol. 273, no. 5274, pp. 475–480, 1996.

[10] E. Borfecchia, C. Garino, L. Salassa, and C. Lamberti, "Synchrotron ultrafast techniques for photoactive transition metal complexes," *Philosophical Transactions of the Royal Society of London A: Mathematical, Physical and Engineering Sciences*, vol. 371, no. 1995, 2013.

[11] Q. Kong, J. Kim, M. Lorenc, T. K. Kim, H. Ihee, and M. Wulff, "Photodissociation reaction of 1,2-diiodoethane in solution: A theoretical and x-ray diffraction study," *The Journal of Physical Chemistry A*, vol. 109, no. 45, pp. 10451–10458, 2005.

[12] Q. Kong, J. Lee, A. Plech, M. Wulff, H. Ihee, and M. Koch, "Ultrafast x-ray solution scattering reveals an unknown reaction intermediate in the photolysis of [ru3(co)12]," *Angewandte Chemie International Edition*, vol. 47, no. 30, pp. 5550–5553, 2008.

[13] K. H. Kim, J. Kim, K. Y. Oang, J. H. Lee, D. Grolimund, C. J. Milne, T. J. Penfold, S. L. Johnson, A. Galler, T. W. Kim, J. G. Kim, D. Suh, J. Moon, J. Kim, K. Hong, L. Guerin, T. K. Kim, M. Wulff, C. Bressler, and H. Ihee, "Identifying the major intermediate species by combining time-resolved x-ray solution scattering and x-ray absorption spectroscopy," *Phys. Chem. Chem. Phys.*, vol. 17, pp. 23298–23302, 2015.

[14] M. Christensen, K. Haldrup, K. Bechgaard, R. Feidenhans'l, Q. Kong, M. Cammarata, M. L. Russo, M. Wulff, N. Harrit, and M. M. Nielsen, "Time-resolved x-ray scattering of an electronically excited state in solution. structure of the 3a2u state of tetrakis-μ-pyrophosphitodiplatinate(ii)," *Journal of the American Chemical Society*, vol. 131, no. 2, pp. 502–508, 2009.

[15] K. Haldrup, T. Harlang, M. Christensen, A. Dohn, T. B. van Driel, K. S. Kjær, N. Harrit, J. Vibenholt, L. Guerin, M. Wulff, and M. M. Nielsen, "Bond shortening (1.4 Å) in the singlet and triplet excited states of [ir2(dimen)4]2+ in solution determined by time-resolved x-ray scattering," *Inorganic Chemistry*, vol. 50, no. 19, pp. 9329–9336, 2011.

[16] K. Haldrup, W. Gawelda, R. Abela, R. Alonso-Mori, U. Bergmann, A. Bordage, M. Cammarata, S. Canton, A. Dohn, T. van Driel, D. Fritz, A. Galler,

P. Glatzel, T. Harlang, K. Kjær, H. Lemke, K. Moller, Z. Németh, M. Pápai, N. Sas, J. Uhlig, D. Zhu, G. Vankó, V. Sundstrom, M. Nielsen, and C. Bressler, "Observing solvation dynamics with simultaneous femtosecond x-ray emission spectroscopy and x-ray scattering," *The Journal of Physical Chemistry B*, vol. 120, no. 6, pp. 1158–1168, 2016.

[17] S. E. Canton, X. Zhang, L. M. Lawson Daku, A. L. Smeigh, J. Zhang, Y. Liu, C.-J. Wallentin, K. Attenkofer, G. Jennings, C. A. Kurtz, *et al.*, "Probing the anisotropic distortion of photoexcited spin crossover complexes with picosecond x-ray absorption spectroscopy," *The Journal of Physical Chemistry C*, vol. 118, no. 8, pp. 4536–4545, 2014.

[18] K. H. Kim, H. Ki, J. H. Lee, S. Park, Q. Kong, J. Kim, J. Kim, M. Wulff, and H. Ihee, "Solvent-dependent structure of molecular iodine probed by picosecond x-ray solution scattering," *Phys. Chem. Chem. Phys.*, vol. 17, pp. 8633–8637, 2015.

[19] H. Ihee, M. Wulff, J. Kim, and S. ichi Adachi, "Ultrafast x-ray scattering: structural dynamics from diatomic to protein molecules," *International Reviews in Physical Chemistry*, vol. 29, no. 3, pp. 453–520, 2010.

[20] K. Haldrup, M. Christensen, and M. Meedom Nielsen, "Analysis of time-resolved x-ray scattering data from solution-state systems," *Acta Crystallographica Section A*, vol. 66, no. 2, pp. 261–269, 2010.

[21] P. Emma *et al.*, "First lasing and operation of an Ångstrom-wavelength free-electron laser," *Nature Photonics*, vol. 4, pp. 641 – 647, 2010.

[22] T. Ishikawa *et al.*, "Compact x-ray free-electron laser emitting in the sub-Ångström region," *Nature Photonics*, vol. 6, pp. 540–544, Feb 2012.

[23] J. Kim, K. Kim, K. Oang, T. Kim, H. Ki, J. Jo, J. Kim, T. Sato, S. Nozawa, S.-i. Adachi, and H. Ihee, "Rotational dephasing of a gold complex probed by anisotropic femtosecond x-ray solution scattering using an x-ray free-electron laser," *Journal of Physics B Atomic Molecular Physics*, vol. 48, no. 24, p. 244005, 2015.

[24] K. H. Kim, J. G. Kim, S. Nozawa, T. Sato, K. Y. Oang, T. W. Kim, H. Ki, J. Jo, S. Park, C. Song, T. Sato, K. Ogawa, T. Togashi, K. Tono, M. Yabashi, T. Ishikawa, J. Kim, R. Ryoo, J. Kim, H. Ihee, and S.-i. Adachi, "Direct observation of bond formation in solution with femtosecond x-ray scattering," *Nature*, vol. 518, p. 385–389, 2015.

[25] D. Arnlund *et al.*, "Visualizing a protein quake with time-resolved x-ray scattering at a free-electron laser," *Nature Methods*, vol. 11, no. 51, p. 923–926, 2014.

[26] C. Pellegrini, "The history of x-ray free-electron lasers," *The European Physical Journal H*, vol. 37, pp. 659–708, 2012.

[27] J. R. Lakowicz, *Principle of fluorescence spectroscopy*. Springer, 2006.

[28] S. Baskin and J. Ahmed H. Zewail, "Oriented ensembles in ultrafast electron diffraction," *ChemPhysChem*, vol. 7, p. 1562 – 1574, 2006.

[29] U. Lorenz, K. B. Møller, and N. E. Henriksen, "On the interpretation of time-resolved anisotropic diffraction patterns," *New Journal of Physics*, vol. 12, no. 11, p. 113022, 2010.

[30] L. U. L. Brinkmann and J. S. Hub, "Anisotropic time-resolved solution x-ray scattering patterns from explicit-solvent molecular dynamics," *The Journal of Chemical Physics*, vol. 143, no. 10, 2015.

[31] J. Kim *et al.*, "Anisotropic picosecond x-ray solution scattering from photoselectively aligned protein molecules," *The Journal of Physical Chemistry Letters*, vol. 2, p. 350–356, 2011.

[32] J. Als-Nielsen and D. McMorrow, *X-rays and their interaction with matter*, pp. 1–28. John Wiley and Sons, Inc., 2011.

[33] Møller and K. B. N. E. Henriksen, "Time-resolved x-ray diffraction:the dynamics of the chemical bond," *Struct Bond*, vol. 142, pp. 185–212, 2012.

[34] J. S. Baskin and A. H. Zewail, "Ultrafast electron diffraction: Oriented molecular structures in space and time," *ChemPhysChem*, vol. 6, no. 11, pp. 2261–2276, 2005.

[35] Asmus O. Dohn, Transient Changes in Molecular Geometries and How to Model Them, PhD Thesis (2015).

[36] A. Rosspeintner, B. Lang, and E. Vauthey, "Ultrafast photochemistry in liquids," *Annual Review of Physical Chemistry*, vol. 64, pp. 247–261, 2013.

[37] A. Pigliucci, G. Duvanel, L. M. Lawson Daku, and E. Vauthey, "Investigation of the influence of solute-solvent interactions on the vibrational energy relaxation dynamics of large molecules in liquids," *The Journal of Physical Chemistry A*, vol. 111, no. 28, pp. 6135–6145, 2007.

[38] M. Berg, "Viscoelastic continuum model of nonpolar solvation. 1. implications for multiple time scales in liquid dynamics," *The Journal of Physical Chemistry A*, vol. 102, no. 1, pp. 17–30, 1998.

[39] R. M. Hochstrasser, "Studies of fast inertial and diffusive motions in liquids," *Hyperfine Interactions*, vol. 38, no. 1, pp. 633–650, 1987.

[40] M. Maroncelli, P. V. Kumar, A. Papazyan, M. L. Horng, S. J. Rosenthal, and G. R. Fleming, "Studies of the inertial component of polar solvation dynamics," *AIP Conference Proceedings*, vol. 298, no. 1, pp. 310–333, 1994.

[41] M. Cho, S. J. Rosenthal, N. F. Scherer, L. D. Ziegler, and G. R. Fleming, "Ultrafast solvent dynamics: Connection between time resolved fluorescence and optical kerr measurements," *The Journal of Chemical Physics*, vol. 96, no. 7, 1992.

[42] S. Palese, L. Schilling, R. J. D. Miller, P. R. Staver, and W. T. Lotshaw, "Femtosecond optical kerr effect studies of water," *The Journal of Physical Chemistry*, vol. 98, no. 25, pp. 6308–6316, 1994.

[43] M. Cammarata, M. Lorenc, T. Kim, J. Lee, Q. Kong, E. Pontecorvo, M. L. Russo, G. Schiro, A. Cupane, M. Wulff, *et al.*, "Impulsive solvent heating probed by picosecond x-ray diffraction," *The Journal of Chemical Physics*, vol. 124, no. 12, p. 124504, 2006.

[44] K. S. Kjaer, T. B. van Driel, J. Kehres, K. Haldrup, D. Khakhulin, K. Bechgaard, M. Cammarata, M. Wulff, T. J. Sørensen, and M. M. Nielsen, "Introducing a standard method for experimental determination of the solvent response in laser pump, x-ray probe time-resolved wide-angle x-ray scattering experiments on systems in solution," *Physical Chemistry Chemical Physics*, vol. 15, pp. 15003–15016, 2013.

[45] R. Hogg and R. G. Wilkins, "Exchange studies of certain chelate compounds of the transitional metals. part viii.," *Journal of the Chemical Society*, p. 341–350, 1962.

[46] O. Kahn and C. J. Martinez, "Spin-transition polymers: From molecular materials toward memory devices," *Science*, vol. 279, pp. 44–48, 1998.

[47] G. Molnár, L. Salmon, W. Nicolazzi, F. Terki, and A. Bousseksou, "Emerging properties and applications of spin crossover nanomaterials," *Journal of Materials Chemistry C*, vol. 2, no. 8, pp. 1360–1366, 2014.

[48] E. Ruiz, "Charge transport properties of spin crossover systems," *Physical Chemistry Chemical Physics*, vol. 16, pp. 14–22, 2014.

[49] S. Hayami, Y. Komatsu, T. Shimizu, H. Kamihata, and Y. H. Lee, "Spin-crossover in cobalt (ii) compounds containing terpyridine and its derivatives," *Coordination Chemistry Reviews*, vol. 255, no. 17, pp. 1981–1990, 2011.

[50] A. Vargas, I. Krivokapic, A. Hauser, and L. M. Lawson Daku, "Towards accurate estimates of the spin-state energetics of spin-crossover complexes within density functional theory: a comparative case study of cobalt(ii) complexes," *Physical Chemistry Chemical Physics*, vol. 15, p. 3752, 2013.

[51] P. Gütlich and H. A. Goodwin, "Spin crossover—an overall perspective," *Topics in Current Chemistry*, vol. 233, pp. 1–47, 2004.

[52] B. N. Figgis, E. S. Kucharski, and A. H. White *Australian Journal of Chemistry*, vol. 36, pp. 1537–1561, 1983.

[53] H. A. Goodwin, "Spin crossover in cobalt (ii) systems," *Topics in Current Chemistry*, vol. 234, pp. 23–47, 2004.

[54] M. Chergui, *Ultrafast Studies of the Light-Induced Spin Change in Fe(II)-Polypyridine Complexes*, pp. 405–424. John Wiley & Sons Ltd, 2013.

[55] M. Cammarata, R. Bertoni, M. Lorenc, H. Cailleau, S. Di Matteo, C. Mauriac, S. F. Matar, H. Lemke, M. Chollet, S. Ravy, *et al.*, "Sequential activation of molecular breathing and bending during spin-crossover photoswitching revealed by femtosecond optical and x-ray absorption spectroscopy," *Physical Review Letters*, vol. 113, no. 22, p. 227402, 2014.

[56] G. Vankó, T. Neisius, G. Molnár, F. Renz, S. Kárpáti, A. Shukla, and F. M. F. de Groot, "Probing the 3d spin momentum with x-ray emission spectroscopy: the case of molecular spin transitions," *The Journal of Physical Chemistry B*, vol. 110, pp. 11647–11653, 2006.

[57] J. Nance, D. N. Bowman, S. Mukherjee, C. T. Kelley, and E. Jakubikova, "Insights into the spin-state transitions in [fe(tpy)2]2+: Importance of the terpyridine rocking motion," *Inorganic Chemistry*, vol. 54, no. 23, p. 11259–11268, 2015.

[58] J. K. Beattie, R. A. Binstead, M. T. Kelso, P. Del Favero, T. G. Dewey, and D. H. Turner, "Dynamics of cobalt (ii) spin-equilibrium complexes," *Inorganica Chimica Acta*, vol. 235, no. 1, pp. 245–251, 1995.

[59] S. Kremer, W. Henke, and D. Reinen, "High-spin-lowspin equilibria of cobalt(2+) in the tyripidine complexes co(terpy)2x2nh2o," *Inorganic Chemistry*, vol. 21, p. 3013–3022, 1982.

[60] D. M. Roundhill, H. B. Gray, and C. M. Che, "Pyrophosphito-bridged diplatinum chemistry," *Accounts of Chemical Research*, vol. 22, no. 2, pp. 55–61, 1989.

[61] R. M. van der Veen, A. Cannizzo, F. van Mourik, A. Vlček, and M. Chergui, "Vibrational relaxation and intersystem crossing of binuclear metal complexes in solution," *Journal of the American Chemical Society*, vol. 133, no. 2, pp. 305–315, 2011.

[62] C. M. Che, L. G. Butler, and H. B. Gray, "Spectroscopic properties and redox chemistry of the phosphorescent excited state of octahydrotetrakis(phosphorus pentoxide)diplatinate(4-) ion (pt2(p2o5)4h84-)," *Journal of the American Chemical Society*, vol. 103, no. 26, pp. 7796–7797, 1981.

[63] A. E. Stiegman, S. F. Rice, H. B. Gray, and V. M. Miskowski, "Electronic spectroscopy of d8-d8 diplatinum complexes.," *Inorganic Chemistry*, vol. 26, no. 7, pp. 1112–1116, 1987.

[64] W. A. Fordyce, J. G. Brummer, and G. A. Crosby, "Electronic spectroscopy of a diplatinum(ii) octaphosphite complex," *Journal of the American Chemical Society*, vol. 103, no. 24, pp. 7061–7064, 1981.

[65] R. van der Veen *et al.*, "Structural determination of a photochemically active diplatinum molecule by time-resolved exafs spectroscopy," *Angewandte Chemie International Edition*, vol. 48, no. 15, pp. 2711–2714, 2009.

[66] M. P. Minitti, J. S. Robinson, R. N. Coffee, S. Edstrom, S. Gilevich, J. M. Glownia, E. Granados, P. Hering, M. C. Hoffmann, A. Miahnahri, *et al.*, "Optical laser systems at the linac coherent light source," *Journal of Synchrotron Radiation*, vol. 22, no. 3, pp. 526–531, 2015.

[67] See Paper II and [68].

[68] K. Haldrup, "Singular value decomposition as a tool for background corrections in time-resolved xfel scattering data," *Philosophical Transactions of the Royal Society of London B: Biological Sciences*, vol. 369, no. 1647, 2014.

[69] See Paper II and [20].

[70] H. Theil, *A Rank-Invariant Method of Linear and Polynomial Regression Analysis*, pp. 345–381. Springer Netherlands, 1992.

[71] P. K. Sen, "Estimates of the regression coefficient based on kendall's tau," *Journal of the American Statistical Association*, vol. 63, no. 324, pp. 1379–1389, 1968.

[72] W. J. Conover, *Practical Nonparametric Statistics, 3rd Edition*. Wiley.

[73] Q. Kong, J. H. Lee, K. H. Kim, J. Kim, M. Wulff, H. Ihee, and M. H. J. Koch, "Ultrafast x-ray solution scattering reveals different reaction pathways in the photolysis of triruthenium dodecacarbonyl (ru3(co)12) after ultraviolet and visible excitation," *Journal of the American Chemical Society*, vol. 132, no. 8, pp. 2600–2607, 2010.

[74] J. Vincent, M. Andersson, M. Eklund, A. B. Wöhri, M. Odelius, E. Malmerberg, Q. Kong, M. Wulff, R. Neutze, and J. Davidsson, "Solvent dependent structural perturbations of chemical reaction intermediates visualized by time-resolved x-ray diffraction," *The Journal of Chemical Physics*, vol. 130, no. 15, 2009.

[75] M. Pápai. Personal communication.

[76] K. S. Kjær. Personal communication.

[77] H. T. Lemke, K. S. Kjær, R. Hartsock, T. B. van Driel, M. Chollet, J. M. Glownia, S. Song, D. Zhu, E. Pace, M. M. Nielsen, M. Benfatto, K. J. Gaffney, E. Collet, and M. Cammarata, "Watching coherent molecular structural dynamics during photoreaction: beyond kinetic description," arXiv:1511.01294.

[78] M. Pápai, G. Vankó, C. de Graaf, and T. Rozgonyi, "Theoretical investigation of the electronic structure of fe(ii) complexes at spin-state transitions," *Journal of Chemical Theory and Computation*, vol. 9, no. 1, pp. 509–519, 2013. PMID: 25821416.

[79] G. Vankó, A. Bordage, M. Pápai, K. Haldrup, P. Glatzel, A. M. March, G. Doumy, A. Britz, A. Galler, T. Assefa, D. Cabaret, A. Juhin, T. B. van Driel, K. S. Kjær, A. Dohn, K. B. Møller, H. T. Lemke, E. Gallo, M. Rovezzi, Z. Németh, E. Rozsályi, T. Rozgonyi, J. Uhlig, V. Sundström, M. M. Nielsen, L. Young, S. H. Southworth, C. Bressler, and W. Gawelda, "Detailed characterization of a nanosecond-lived excited state: X-ray and theoretical investigation of the quintet state in photoexcited [fe(terpy)2]2+," *The Journal of Physical Chemistry C*, vol. 119, p. 5888–5902, February 25 2015.

[80] X. Zhang, M. L. Lawson Daku, J. Zhang, K. Suarez-Alcantara, G. Jennings, C. A. Kurtz, and S. E. Canton, "Dynamic jahn–teller effect in the metastable high-spin state of solvated [fe(terpy)2]2+," *The Journal of Physical Chemistry C*, vol. 119, no. 6, pp. 3312–3321, 2015.

[81] A. Hauser, C. Enachescu, M. L. Daku, A. Vargas, and N. Amstutz, "Low-temperature lifetimes of metastable high-spin states in spin-crossover and in low-spin iron(ii) compounds: The rule and exceptions to the rule," *Coordination Chemistry Reviews*, vol. 250, p. 1642–1652, 2006.

[82] R. Jimenez, G. R. Fleming, P. V. Kumar, and M. Maroncelli, "Femtosecond solvation dynamics of water," *Nature*, vol. 369, pp. 471–473, 1994.

[83] E. W. Castner, Y. J. Chang, Y. C. Chu, and G. E. Walrafen, "The intermolecular dynamics of liquid water," *The Journal of Chemical Physics*, vol. 102, no. 2, 1995.

[84] https://wiki.fysik.dtu.dk/gpaw/.

[85] G. Levi. Personal communication.

[86] A. N. Tarnovsky, W. Gawelda, M. Johnson, C. Bressler, and M. Chergui, "Photexcitation of aqueous ruthenium(ii)-tris-(2,2'-bipyridine) with high-intensity femtosecond laser pulses," *The Journal of Physical Chemistry B*, vol. 110, no. 51, pp. 26497–26505, 2006.

[87] M. Horng, J. A. Gardecki, and M. Maroncelli, "Rotational dynamics of coumarin 153: Time-dependent friction, dielectric friction, and other non-hydrodynamic effects," *The Journal of Physical Chemistry A*, vol. 101, no. 6, pp. 1030–1047, 1997.

[88] T. J. Penfold, B. F. E. Curchod, I. Tavernelli, R. Abela, U. Rothlisberger, and M. Chergui, "Simulations of x-ray absorption spectra: the effect of the solvent," *Phys. Chem. Chem. Phys.*, vol. 14, pp. 9444–9450, 2012.

[89] M. L. Horng, J. A. Gardecki, A. Papazyan, and M. Maroncelli, "Subpicosecond measurements of polar solvation dynamics: Coumarin 153 revisited," *The Journal of Physical Chemistry*, vol. 99, no. 48, pp. 17311–17337, 1995.

Paper I

IOP Publishing Journal of Physics B: Atomic, Molecular and Optical Physics
J. Phys. B: At. Mol. Opt. Phys. **48** (2015) 244010 (8pp) doi:10.1088/0953-4075/48/24/244010

On the calculation of x-ray scattering signals from pairwise radial distribution functions

Asmus O Dohn[1], Elisa Biasin[2], Kristoffer Haldrup[2], Martin M Nielsen[2], Niels E Henriksen[1] and Klaus B Møller[1]

[1] Department of Chemistry, Technical University of Denmark, Kemitorvet 207, 2800, Kgs. Lyngby
[2] Department of Physics, Technical University of Denmark, Fysikvej 307, 2800, Kgs. Lyngby

E-mail: asod@kemi.dtu.dk and kbmo@kemi.dtu.dk

Received 4 June 2015, revised 2 September 2015
Accepted for publication 15 September 2015
Published 4 November 2015

Abstract

We derive a formulation for evaluating (time-resolved) x-ray scattering signals of solvated chemical systems, based on pairwise radial distribution functions, with the aim of this formulation to accompany molecular dynamics simulations. The derivation is described in detail to eliminate any possible ambiguities, and the result includes a modification to the atom-type formulation which to our knowledge is previously unaccounted for. The formulation is numerically implemented and validated.

Introduction

This work is concerned with the derivation of a formulation for evaluating time-resolved x-ray scattering signals of chemical systems in solution phase, based on pairwise radial distribution functions (RDFs). We aim to provide a full formalism, with the complete set of details behind its derivation, to go hand in hand with molecular dynamics (MD) simulations. These simulations are becoming more and more ubiquitous in—and essential for—the analysis of ultra-fast x-ray scattering experiments of solvated molecules [1–4]. The motivation for the work is threefold:

The physical aspect: Due to quantum and/or statistical ensemble effects, interatomic distances are inherently governed by probability distributions. The much used Debye formulation [5] of x-ray scattering, historically derived with crystalline systems in mind, assumes definite interatomic distances. Broadening can be introduced retrospectively, e.g. by averaging over scattering signals from a collection of distinct structures or using the Debye-Waller model. However, it seems appropriate to have a formulation of x-ray scattering based directly on the continuous nature of the actual probability distributions describing the physical situation.

The practical aspect: For any analysis, it is always desirable to cut computational costs and unnecessary complexity. Averaging over Debye signals scales with the number of atoms squared times the number of system configurations (frames) used. The fastest programs developed (mainly for crystallographic purposes) state that computing the scattering e.g. for a system of the equivalent size of 1000 frames from a $50 \times 50 \times 50$ Å^3 box would take days, and should be run on a cluster [6]. Programs have been developed [7] that can calculate RDFs for systems of similar sizes in hours if not minutes on a desktop computer, equipped with a GPU [8]. The method presented here could furthermore allow for direct manipulation of the RDFs, in a fitting-scenario. Either way, adopting the formulation introduced in this work can drastically improve the analysis workflow of x-ray scattering experiments in the solution phase.

The unambiguity aspect: The first work on this formulation is almost a century old [9], and many versions and modifications have been presented [1, 5, 10–23]. Much of the work has been based on determining the atomic distributions from scattering signals, not vice versa, and not always with explanations for modifications made, compared to previous publications. If some of these models are lifted straight from their papers and implemented numerically, substantial errors in the resulting signal can occur. We therefore believe it is necessary to present a fully-detailed derivation of the formalism that explains the choices and background for each step,

to take advantage of the improvements in the physical and practical aspects that this formulation has to offer.

Derivation of the formulation

For molecular x-ray scattering restricted to a single electronic state, the elastic scattering signal in units of the Thomson cross-section (a.k.a. electronic units) $S(\boldsymbol{q})$, where $\boldsymbol{q}$ is the scattering vector, is a function of the nuclear probability distribution $\rho^{(N)}(\boldsymbol{R}, t)$ of the N-atom system with coordinates $\boldsymbol{R} = (\boldsymbol{R}_1, \boldsymbol{R}_2 \ldots \boldsymbol{R}_N)$, and the molecular form factor $F(\boldsymbol{R}, \boldsymbol{q})$ [24]:

$$S(\boldsymbol{q}) = \int_0^\infty I(t) \int_{V^N} \rho^{(N)}(\boldsymbol{R}, t) |F(\boldsymbol{R}, \boldsymbol{q})|^2 d^N\boldsymbol{R} dt \quad (1)$$

where $I(t)$ is the intensity function of the x-ray probe pulse, and V is the volume of the sample over which the irradiating x-ray beam is coherent. If the total irradiated sample volume is larger than the coherence lengths of the beam, the total scattering signal from the sample is the sum of individual scattering signals given by equation (1), arising from sub-volumes over which the beam can be considered coherent [5, 25]. The molecular form factor is in principle the expectation value of the scattering operator on the all-electron wavefunction, which can be shown to give a Fourier transform of the electronic density $\rho_e(\boldsymbol{r}; \boldsymbol{R})$ [24]:

$$F(\boldsymbol{R}, \boldsymbol{q}) = \int_V \rho_e(\boldsymbol{r}; \boldsymbol{R}) e^{i\boldsymbol{q}\cdot\boldsymbol{r}} d\boldsymbol{r} \quad (2)$$

Almost always, the assumption is made that the scattering can be described as scattering from independent atoms, with spherical electronic densities. This is called the Independent Atom Model (IAM), which effectively turns the molecular scattering factor into a sum of atomic form factors $f_j(q)$:

$$F_{\mathrm{IAM}}(\boldsymbol{R}, \boldsymbol{q}) = \sum_j^N f_j(q) e^{i\boldsymbol{q}\cdot\boldsymbol{R}_j} \quad (3)$$

Even though this approximation ignores chemical bonding, it is in most cases very accurate for resolving molecular geometries [26], with few exceptions [18], see also [27]. While the full electronic distribution is directly available via *ab initio* simulations, using it directly with an adequate numerical precision within a multidimensional structural-fitting strategy, as employed e.g. by the experimental section of our group [28, 29], is unnecessarily cumbersome when working with systems where the IAM is sufficient.

The signal in the IAM is:

$$\begin{aligned} S(\boldsymbol{q}) &= \int_{V^N} \rho^{(N)}(\boldsymbol{R}) \, |F(\boldsymbol{R}, \boldsymbol{q})|^2 d^N\boldsymbol{R} \\ &= \int_{V^N} \rho^{(N)}(\boldsymbol{R}) \sum_j f_j(q) e^{-i\boldsymbol{q}\cdot\boldsymbol{R}_j} \sum_k f_k(q) e^{i\boldsymbol{q}\cdot\boldsymbol{R}_k} d^N\boldsymbol{R} \end{aligned} \quad (4)$$

where $\rho^N(\boldsymbol{R})$ is the average nuclear probability distribution during the duration of the x-ray probe pulse. We first separate the sums into sums of $j = k$ and $k \neq j$:

$$\begin{aligned} S(\boldsymbol{q}) = \int_{V^N} \rho^{(N)}(\boldsymbol{R}) \Bigg(&\sum_j f_j(q)^2 \\ &+ \sum_j \sum_{k \neq j} f_j(q) f_k(q) e^{-i\boldsymbol{q}\cdot(\boldsymbol{R}_j - \boldsymbol{R}_k)} \Bigg) d^N\boldsymbol{R} \end{aligned} \quad (5)$$

Since the density is normalised, after integration the first sum is simply $\sum_j f_j(q)^2$. We now focus on the second sum. In our previous work, it has been favourable to transform the coordinates to an internal basis [24, 30, 31], while here, we simply note that the exponential in each term is only dependent on the positions of two particles for each term in the sum. Hence, for each pair j, k, a pairwise density distribution function is constructed by integrating all the other dependencies out:

$$\begin{aligned} &\rho^{(2)}_{j,k}(\boldsymbol{R}_j, \boldsymbol{R}_k) \\ &= \int_{V^{N-2}} \rho^{(N)}(\boldsymbol{R}) d\boldsymbol{R}_1 d\boldsymbol{R}_2 \cdots \\ &\quad \times d\boldsymbol{R}_{j-1} d\boldsymbol{R}_{j+1} \cdots d\boldsymbol{R}_{k-1} d\boldsymbol{R}_{k+1} \cdots d\boldsymbol{R}_N \end{aligned} \quad (6)$$

We then substitute the integration variables $\boldsymbol{r} = \boldsymbol{R}_j - \boldsymbol{R}_k$, and $\boldsymbol{r}' = (\boldsymbol{R}_j + \boldsymbol{R}_k)/2$, and pull the distribution $\rho^{(2)}_{j,k}(\boldsymbol{r}, \boldsymbol{r}')$ through the sum in the integral of equation (5):

$$\begin{aligned} &\sum_j \sum_{k \neq j} f_j(q) f_k(q) \int_{V^2} \rho^{(2)}_{j,k}(\boldsymbol{r}, \boldsymbol{r}') e^{-i\boldsymbol{q}\cdot\boldsymbol{r}} d\boldsymbol{r} d\boldsymbol{r}' \\ &= \sum_j \sum_{k \neq j} f_j(q) f_k(q) \int_V \rho^{(1)}_{j,k}(\boldsymbol{r}) e^{-i\boldsymbol{q}\cdot\boldsymbol{r}} d\boldsymbol{r} \end{aligned} \quad (7)$$

where $\rho^{(1)}_{j,k}(\boldsymbol{r}) = \int_V \rho^{(2)}_{j,k}(\boldsymbol{r}, \boldsymbol{r}') d\boldsymbol{r}'$, which leaves us with a sum of integrals over each atomic pair and its corresponding probability density. Dropping the pair density-superscript on the probability distribution for brevity, we write up the full equation:

$$\begin{aligned} S(\boldsymbol{q}) = &\sum_j f_j(q)^2 + \sum_j \sum_{k \neq j} f_j(q) f_k(q) \\ &\times \int_V \rho_{j,k}(\boldsymbol{r}) e^{-i\boldsymbol{q}\cdot\boldsymbol{r}} d\boldsymbol{r} \end{aligned} \quad (8)$$

Now we make the isotropic assumption, meaning that there is equal probability of finding the entire molecule in any orientation. This must mean that there is also equal probability of finding *each* of the intermolecular vectors in any orientation, since a rotation of the molecule must mean a rotation of all of its pairwise vectors. In other words, we assume that $\rho_{j,k}(\boldsymbol{r}) = \rho_{j,k}(r)$. For ultrafast studies, the isotropic assumption might not always hold, but we note that all the available structural information can be extracted from the isotropic contribution to the total scattering [24]. Options for including angular dependence in scattered intensity-equations of isolated molecules have been derived elsewhere [24, 31, 32]. Evaluating the integral in the isotropic case leads

to [5, 12]:

$$\int_V \rho_{j,k}(\boldsymbol{r}) e^{-i\boldsymbol{q}\cdot\boldsymbol{r}} d\boldsymbol{r} = 4\pi \int_0^R \rho_{j,k}(r) \frac{\sin(qr)}{qr} r^2\, dr \qquad (9)$$

where R is the radius of the (on average spherically symmetric) coherence volume in the sample. Including the first sum in equation (8) we get:

$$S(q) = \sum_j f_j(q)^2 + \sum_j \sum_{k\neq j} f_j(q) f_k(q) 4\pi \times \int_0^R \rho_{j,k}(r) \frac{\sin(qr)}{qr} r^2 dr \qquad (10)$$

The double sum in equation (10) is over all atomic pairs in the system.

With distribution functions, one can collect correlations between atoms by grouping atoms into sets of 'types', for a suitable definition of 'type'. With x-ray scattering in mind, the largest possible sets can be made by grouping all atoms exhibiting identical scattering behaviour under the same type. Within the IAM this corresponds to equating type and element/ion[3]. However, we are free to further divide species of the same element/ion into different types, e.g. by distinguishing whether an atom belongs to the solute or the solvent, as shall become relevant later. With this definition of atom types, we need to redistribute the probability terms as follows: If N_l and N_m are the numbers of all atoms of type l and type m, respectively, we collect all the probability distributions $\rho_{j,k}(r)$ where atom j is of type l, and atom k is of type m into one distribution, $\rho_{l,m}(r)$. Since we also need to construct the probability distributions between different atoms in the same type, we need to make sure that the same atom ($j = k$) is not counted twice in these cases of $l = m$:

$$\rho_{l,m}(r) = \frac{1}{N_l(N_m - \delta_{l,m})} \sum_{j\in l}^{N_l} \sum_{\substack{k\in m \\ k\neq j}}^{N_m} \rho_{j,k}(r) \qquad (11)$$

where $\delta_{l,m}$ is the Kronecker delta. As mentioned, l can be equal to m. In these cases, $k \neq j$ in the summation, and to avoid pairing atoms with themselves, the normalization factor is $\frac{1}{N_l(N_m-1)}$.

Since the form factors in equation (10) are not dependent on r, they can be included in the integral and the sum can be rewritten with the definition of atom types:

$$\sum_{j\neq k} f_j(q) f_k(q) \rho_{j,k}(r) = \sum_l \sum_m \sum_{j\in l}^{N_l} \sum_{\substack{k\in m \\ k\neq j}}^{N_m} f_j(q) f_k(q) \rho_{j,k}(r)$$

where $f_j = f_l$ if $j \in l$ so:

$$= \sum_l \sum_m f_l(q) f_m(q) \sum_{j\in l}^{N_l} \sum_{\substack{k\in m \\ k\neq j}}^{N_m} \rho_{j,k}(r)$$

and using the definition in equation (11):

$$= \sum_l \sum_m N_l(N_m - \delta_{l,m}) f_l(q) f_m(q) \rho_{l,m}(r) \qquad (12)$$

which is then substituted into equation (10). Using the contracted notation for the double sum over l and m:

$$S(q) = \sum_l N_l f_l(q)^2 + \sum_{l,m} f_l(q) f_m(q) N_l(N_m - \delta_{l,m}) 4\pi \times \int_0^R \rho_{l,m}(r) \frac{\sin(qr)}{qr} r^2 dr \qquad (13)$$

where we also rewrote the sum of form factors squared for each atom, to the atom-type notation, which is $\sum_{j\in l}^{N_l} f_j(q)^2$. To finally express the scattering in terms of the (pairwise) radial distribution functions $g_{l,m}(r)$, easily obtainable from MD simulations, we recall that the probability densities and number densities are proportional, so we can use an equivalent analogy to the standard definition [10]: $g_{l,m}(r) = \frac{\rho_{l,m}(r)}{\rho_{0,l,m}}$, where $\rho_{0,l,m} = 1/V$ is the isotropic probability density, with V being the coherence volume. Thus:

$$S(q) = \sum_l N_l f_l(q)^2 + \sum_{l,m} f_l(q) f_m(q) \frac{N_l(N_m - \delta_{l,m})}{V} 4\pi \times \int_0^R r^2 g_{l,m}(r) \frac{\sin(qr)}{qr} dr \qquad (14)$$

which is the main result of this work. Illustrations of $g_{l,m}(r)$ functions can be found in figure 1. The $l = m$ terms in the double sum seem to be left out of some presentations of the formalism [1, 22], which would result in the neglection of all contributions of scattering from different atoms of the same atom type. In other works [19], l can be equal to m in the sum, but the $-\delta_{l,m}$ term is left out. If N_m is very large, this is a fine approximation, but the approximation will *not* hold for systems containing a few particularly intense scatterers such as Pt, Ir, I, etc. On a diatomic system of the same atom type, neglecting $-\delta_{l,m}$ will result in a twice as large $l = m$-term contribution to the double sum, compared to the correct result. How the full scattering signal is affected is exemplified in figure 2.

For practical applications of equation (14) a few more steps are needed, but first, we show that equation (14) is a generalisation of the Debye-equation. If we choose the types such that each atom is its own type, the RDF for an isolated pair of atoms j and k at distance $r_{j,k}$ must be a delta function, and $N_j = N_k = 1$:

$$4\pi r^2 \rho_{j,k}(r) dr = \frac{4\pi r^2 g_{j,k}(r)}{V} dr = \delta(r - r_{j,k}) dr \qquad (15)$$

[3] since there are tabulated values for form factors for the same element with different charges [33].

J. Phys. B: At. Mol. Opt. Phys. **48** (2015) 244010 A O Dohn *et al*

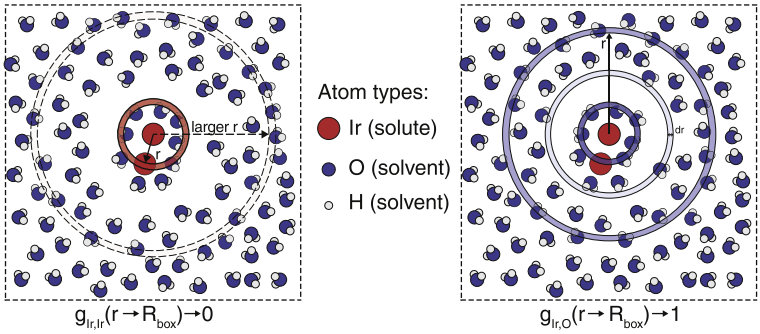

Figure 1. Illustration of the calculation of various pairwise RDFs, where the atom types are divided into subgroups based on whether they belong to the solute or the solvent. The solute here is an artificial Ir-diatomic, a simplified example based on real, previously studied systems, [40, 41]. On the left illustration where $l = m =$ Ir, the $g_{\mathrm{Ir,Ir}}(r)$ will go to 0 for $r \rightarrow R_{\mathrm{box}}$. For the solute-solvent pair on the right illustration, the simulation box is large enough that $g_{\mathrm{Ir,O}}(r)$ will converge to 1, past the solvent-shell quasi-structure. In the region just after the first solvation shell, $g_{\mathrm{Ir,O}}(r) < 1$.

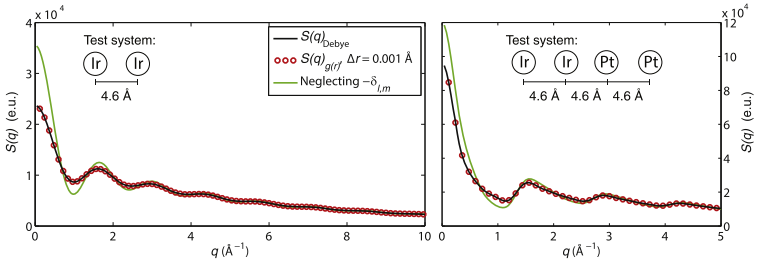

Figure 2. Comparisons of numerical implementations of calculated x-ray scattering from two single geometries (i.e. no MD-based thermal averaging), $S(q)$, implemented in Matlab®. The scattered intensity (in electronic units) goes to the number of electrons squared in the sample, when $q \rightarrow 0$. The green curves show the resulting calculated scattering from neglecting the $-\delta_{l,m}$ term, as discussed in the text.

which we can insert into equation (14):

$$S(q) = \sum_j N_j f_k(q)^2 + \sum_{j,k} f_j(q) f_k(q) N_j \left(N_k - \delta_{j,k}\right) \times \int_0^R \delta(r - r_{j,k}) \frac{\sin(qr)}{qr} dr$$

leading to the Debye-equation:

$$S(q) = \sum_j \sum_k f_j(q) f_k(q) \frac{\sin(qr_{j,k})}{qr_{j,k}} \tag{16}$$

where have collected the two sums back into one term, since $\frac{\sin(qr_{j,k})}{qr_{j,k}} \rightarrow 1$ for $r_{j,k} \rightarrow 0$, i.e. for $j = k$.

Returning to the applications of equation (14), one can conveniently rewrite the integral in the equation by adding and subtracting the distribution in the constant-density limit at long distances, $g_{0,l,m}$ (see discussion below) such that:

$$\int_0^R g_{l,m}(r) \frac{\sin(qr)}{qr} r^2 dr = \int_0^R \left[g_{l,m}(r) - g_{0,l,m}\right] \frac{\sin(qr)}{qr} r^2 dr + g_{0,l,m} \int_0^R \frac{\sin(qr)}{qr} r^2 dr \tag{17}$$

For large values of R, the last term has been argued to only contribute at $q \rightarrow 0$, and therefore often excluded [10, 11, 13–15], since this part of the q-range is often covered in the experimental setup by the beamstop. This claim deserves a bit of elaboration. Evaluating the integral gives

$$\int_0^R \frac{\sin(qr)}{qr} r^2 dr = \frac{\sin(qR)}{q^3} - \frac{R\cos(qR)}{q^2} \tag{18}$$

Since $R \gg q^{-1}$, for q being on the order of 1 Å^{-1}, the resulting absolute value of the integral will not be small, compared to the first term of equation (17), in the experimentally interesting region. However, the resulting value is rapidly oscillating in q with a period of $2\pi/R$. In traditional x-ray experiments, the coherence length R of the beam is typically much shorter (approx 0.1–1 μm ([34])) than the extent of the irradiated sample (on the order of, say, 10–100 μm). This implies that the rapidly oscillating integrals, equation (18), cancel out in the total scattering emitted from the irradiated sample [5, 16, 25]. We note that it is indeed possible on modern x-ray sources to construct experiments where the probed sample volume is tailored to match the coherence length of the beam [25, 35–39], but this will not be considered further here. For the time-resolved scattering community, the discussion of this particular term in equation (18) can be avoided altogether by evaluating 'difference-distributions' and calculating the difference scattering directly from those, as we shall see later.

In conclusion, when the total experimental signal is a sum of scattering signals $S(q)$ from individual coherence volumes, we can omit the last term in equation (17):

$$S(q) = \sum_l N_l f_l(q)^2 + \sum_{l,m} f_l(q) f_m(q) \frac{N_l(N_m - \delta_{l,m})}{V} 4\pi \times \int_0^R r^2 \left[g_{l,m}(r) - g_{0,l,m} \right] \frac{\sin(qr)}{qr} dr \tag{19}$$

which can be implemented numerically. Often [1, 19, 22] (but not always [14, 15]), $g_{0,l,m}$ is simply written as 1, since $g_{l,m}(r)$ is normalised w.r.t the macroscopic density. In the case of pure liquids, and also for dilute samples with macroscopic volumes, this is true. However, in MD simulations of solutions with finite box dimensions, not all pairs of atom types have radial distributions that reach the convergence limit of 1 within the simulation dimensions. Considering the actual computation of the scattering signal from an MD simulation, in order to subtract the correct $g_{0,l,m}$-value, we can make use of the previously mentioned freedom in defining atom types to define subgroups based on whether the atoms belong to the solute or the solvent (see figure 1). For solvent-solvent RDFs, where both atom types l and m belong to the solvent subgroup, $g_{l,m}(r) \to 1$ typically within 10–20 Å. The same is the case for solute-solvent pairs, as long as the solute itself is not too large. The MD box should be large enough for the convergence to take place. The solute-solute distance in a dilute sample is so long that the intersolute scattering can be neglected. In an MD simulation typically only one solute molecule is included, and therefore, the computed $g_{l,m}(r)$ for l, m types in the solute will go to zero.

With these values for $g_{0,l,m}$, the difference $g_{l,m}(r) - g_{0,l,m}$ will go to zero within the simulation box. We can therefore replace R of the sample by R_{box} of the box dimensions as the upper integration limit, as the length of the simulation box is typically much shorter that the coherence length of the x-ray beam. Furthermore, for clarity (and sometimes for convenience in the further analysis) we can split up the scattering signal into contributions from solvent-solvent terms $S_{\text{v}}(q)$, solute-solvent (cross) terms $S_{\text{c}}(q)$, and solute-solute terms $S_{\text{u}}(q)$:

$$S_{\text{v}}(q) = \sum_l^v N_l f_l(q)^2 + \sum_{l,m}^v f_l(q) f_m(q) \frac{N_l(N_m - \delta_{l,m})}{V} 4\pi \times \int_0^{R_{\text{box}}} r^2 \left[g_{l,m}(r) - 1 \right] \frac{\sin(qr)}{qr} dr \tag{20a}$$

$$S_{\text{c}}(q) = \sum_l^c N_l f_l(q)^2 + \sum_{l,m}^c f_l(q) f_m(q) \frac{N_l(N_m - \delta_{l,m})}{V} 4\pi \times \int_0^{R_{\text{box}}} r^2 \left[g_{l,m}(r) - 1 \right] \frac{\sin(qr)}{qr} dr \tag{20b}$$

$$S_{\text{u}}(q) = \sum_l^u N_l f_l(q)^2 + \sum_{l,m}^u f_l(q) f_m(q) \frac{N_l(N_m - \delta_{l,m})}{V} 4\pi \times \int_0^{R_{\text{box}}} r^2 g_{l,m}(r) \frac{\sin(qr)}{qr} dr \tag{20c}$$

where the v, c, u-notation above the sums indicate that the types included in the sums should belong to their respective groups.

In standard MD analysis programs, the RDFs are normalized using the simulation box volume $V = V_{\text{box}}$, in conjunction with the number of particles N_l of type l and N_m of type m in the simulation box. Hence, for numerical consistency, one should use the same values in the above equations. However, this will result in a scaling of the absolute signal by $N_{\text{box}}/N_{\text{sample}}$. Furthermore, since the solute concentration in the simulation box probably varies from the solute concentration in the sample, the three contributions $S_u(q)$, $S_c(q)$, and $S_v(q)$ must be scaled accordingly.

Two further issues arise when the numerical implementation is made:

1. Constraining bonds is an often used technique within MD. The numerical representation of constrained bond intramolecular $g_{j,k}(r)$'s with delta-distribution-like characteristics depends on the numerical precision in $dr \approx \Delta r$, the bin width for the sampled distributions.
2. The integral in equation (19) is truncated at R_{box}.

The second issue introduces spurious truncation oscillations in the calculated scattering signal, since the integral is essentially the Fourier transformation of $g_{l,m}(r)$. Many methods have been applied to this problem, often for the reverse version of obtaining $g_{l,m}(r)$ functions from $S(q)$ [12, 18, 21, 23, 42–45]. Some fit the tail of the data to an analytic function [42], while others apply a damping function to the Fourier transformation [21, 44], and others again have developed more involved methods [18, 23, 43]. We have found it adequate so far to simply employ a damping function $\frac{\sin(\pi r/L)}{\pi r/L}$ [20, 21, 45] in the transformation:

$$S(q) = \sum_l N_l f_l(q)^2 + \sum_{l,m} f_l(q) f_m(q) \frac{N_l(N_m - \delta_{l,m})}{V} 4\pi \times \int_0^{R_{\text{box}}} r^2 \left[g_{l,m}(r) - g_{0,l,m} \right] \frac{\sin(qr)}{qr} \frac{\sin\left(\frac{\pi r}{L}\right)}{\frac{\pi r}{L}} dr \tag{21}$$

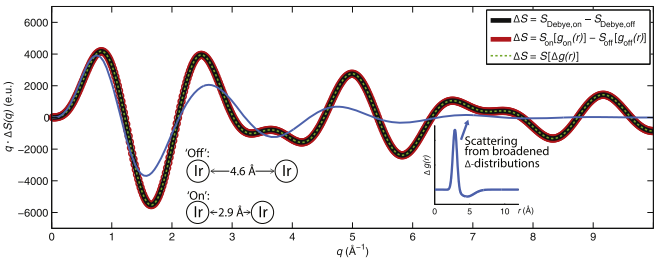

Figure 3. Comparison of numerically evaluating the difference-scattering $\Delta S(q)$ via the equations (16) (black), (20*c*) (red), and (22) (green dashed). The example is a simulation of two Ir-Ir atoms 4.6 Å apart ('off') and 2.9 Å ('on'). The blue curve on the plot shows simulated scattering from broadened distributions, more akin to real experimental conditions. The $\Delta g_{l,m}(r)$-distribution is constructed by subtracting a gaussian distribution with $\mu_{\text{off}} = 4.6$ and $\sigma_{\text{off}} = 1$ from another gaussian distribution with $\mu_{\text{on}} = 2.9$ and $\sigma_{\text{off}} = 0.3$ (see inset).

Some authors [21] choose L to be half the size of the simulation box, while others [44] provide no physical justification for their chosen value.

In its most basic description, time resolved x-ray pump-probe scattering experiments are carried out by using a 'pump' laser pulse to electronically excite the solute, instigating the dynamics, and then measuring the scattering, $S_{\text{on}}(q)$ at a given time t after excitation, by an ultrashort x-ray 'probe' pulse. Then, the signal from the unpumped sample $S_{\text{off}}(q)$ is subtracted to create $\Delta S(q) = S_{\text{on}}(q) - S_{\text{off}}(q)$, only containing contributions from the transient features of the studied geometries. Exploiting the fact that form factors are identical in the 'on' and 'off' state within the IAM, the integral in equation (14) can be made to converge inside the simulation box in another way, namely via 'difference distributions':

$$\Delta S(q) = \sum_{l,m} f_l(q) f_m(q) \frac{N_l\left(N_m - \delta_{l,m}\right)}{V} 4\pi \times \int_0^{R_{\text{box}}} \Delta g_{l,m}(r) \frac{\sin(qr)}{qr} r^2 dr \qquad (22)$$

where $\Delta g_{l,m}(r) = g_{l,m,\text{on}}(r) - g_{l,m,\text{off}}(r)$. Here, the discussion of equation (18) becomes moot, since $g_{l,m,\text{on}}(r)$ and $g_{l,m,\text{off}}(r)$ have the same limits at long distances.

Evaluating the Derivation Using a Numerical Implementation

Figure 2 shows a comparison of the numerical implementation of equation (21) made in the Matlab® programming language, with a numerical implementation of the Debye formula (equation (16)), as previously implemented and used in our group [28, 29]. The simplified test systems are chosen to confirm the validity of the derivation, especially with regards to the counting of atoms of each type, since we in this aspect diverge from previous derivations. Test system 1 consists of a single frame of two Ir atoms 4.6 Å apart, while test system 2 contains two Ir atoms and two Pt atoms on a line, with the same nearest-neighbour spacing as in system 1. For the $S(q)$ calculated via equation (20*c*), $g_{l,m}(r)$ was evaluated in the VMD program [7], with $\Delta r = 0.001$ Å in a cubic box of 100 Å side lengths, thus numerically approximating the delta-function when using $V = V_{\text{box}}$. For both test systems, the two different methods of calculating the scattering provide identical results, within the numerical accuracy. Furthermore, the validity of the implementation (and therefore the derivation) is supported by the scattered intensity value at $q \to 0$: In this limit, the scattering goes to $\left|\sum_j f_j(q \to 0)\right|^2$. Remembering that, in principle, $f(q) = \int \rho(r) e^{iqr} dr$, where $\rho(r)$ is the atomic electronic density, then $S(q \to 0) \to n^2$ where n is the number of electrons in the system[4]. Thus, it is confirmed that the two implementations produce the same scattered intensity for molecular systems.

Figure 3 shows that equation (22) successfully reproduces the Debye formulation result for the prototypical time-dependent scattering experiment where two atoms are at a shorter distance after laser excitation (assuming infinitely short pump and probe pulses). The blue curve represents scattering simulated using a broadened $\Delta g_{l,m}(r)$-distribution shown in the inset, using gaussian broadening factors based on our recent findings for a bi-metallic Ir-system [40] (neglecting the observed anharmonicity of the underlying potential, since the illustration done here is only for explanatory purposes). We note that probabilistic distributions of atomic positions, inherent everywhere in nature, change the observable scattering signal.

The next benchmarking step involves using equation (20*a*) to calculate the scattering of neat water at standard pressure and 300 K, as shown in figure 4. Due to the previously described impracticalities of using the Debye-equation (equation (16)) to calculate scattering signals from MD simulations, we compare our calculated scattering of an MD simulation of neat water, using the TIP4P-eW potential [46], to experimentally obtained results [45, 47, 48]. This of course means that differences in the two signals can arise

[4] The calculated scattering intensity in figure 2, left, at $q = 0.02$ Å is $2.37 \times 10^4 = (77 \times 2)^2$

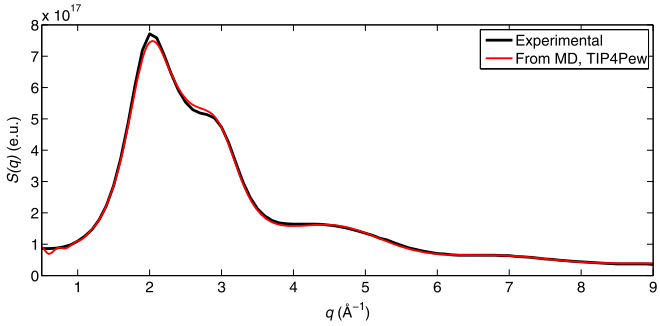

Figure 4. Red curve: Simulated scattering from an NVT MD simulation of $(50\ \text{Å})^3$ pure water at 300 K, using the TIP4P-eW potential [46], calculated using N_O and N_H values for a 46 μm sphere of neat water. Black curve: An experimentally obtained [47] scattered x-ray intensity profile from neat water, scaled in $2.9\ \text{Å}^{-1} < q < 6.0\ \text{Å}^{-1}$ to the simulated signal.

from inconsistencies of the model potential with actual water. The simulation reproduces the experimental signal within the precision of the TIP4P-eW potential, and taking into account the already explored problems with using the IAM for water [48]. This concludes the benchmarking of the new numerical implementation, which confirms the derivation.

Concluding remarks

In this work, we have provided an in-depth derivation of what can be described as a generalisation of the Debye-scattering equation (equation (16)), as we demonstrated collapsing the probability distributions to just single distances reverted the derived formulation back into the Debye result. The pairwise RDF-based equations (equations (20*a*)–(20*c*)) for the x-ray scattering readily provides significant advantages: Both practical, such as being able to use already established tools of high efficiency to obtain the needed RDFs, and from a physical interpretation point of view, e.g. readily splitting up scattering-contributions from various parts of the studied system.

With this review of the background behind the present formulation and considering its successful reproduction of known results, we hope that it will provide the motivation needed for including the derived formalism in the ever expanding toolbox of the (time-resolved) x-ray solution scattering community. In particular, the advancement towards extracting from experiment quantum and ensemble effects on structure and dynamics. Future theoretical developments will include further explorations on how to invert [31, 45, 49] the presented equations to obtain, directly from experimental signals, nuclear and electronic probability distributions.

Acknowledgments

The authors thank R Hartsock for discussions and feedback, and the reviewers for insightful comments. This work was funded by Lundbeck Foundation and the Danish Council for Independent Research.

References

[1] Ihee H, Wulff M, Kim J and Adachi S 2010 *Int. Rev. in Phys. Chem.* **29** 453
[2] Haldrup M *et al* 2012 *J. Phys. Chem.* A **116** 9878
[3] Kim K, KIM J, Lee J and Ihee H 1986 *Structural Dynamics* **1** 011301
[4] Vankó G *et al* 2015 *J. Phys. Chem.* C **119** 5888
[5] Als-Nielsen J and McMorrow D 2011 *Elements of Modern X-ray Physics* 2nd ed (Hoboken, NJ: Wiley)
[6] https://code.google.com/p/debyer/ , accessed June 1st, 2015
[7] Humphrey W, Dalke A and Schulten K 1996 *J. Molec. Graphics* **14** 33
[8] Levine B G, Stone J E and Kohlmeyer A 2011 *J. Comput. Phys.* **230** 3556
[9] Zernike F and Prins J A 1927 *Zeitschrift Für Physik* **41** 184
[10] McQuarrie D A 1976 *Statistical Mechanics* (London: Harper & Row)
[11] Gingrich N S and Warren B E 1934 *Phys. Rev.* **46** 248
[12] Warren B E 1990 *X-Ray Diffraction* (Mineola, NY: Dover Publications)
[13] Gingrich N S 1943 *Rev. Mod. Phys.* **15** 90
[14] Klug H P and Alexander L E 1974 *X-ray Diffraction Procedures: For Polycrystalline and Amorphous Materials* 2nd ed (Hoboken, NJ: Wiley) ISBN 978-0-471-49369-3
[15] Kruh R F 1962 *Chemical Review* **62** 319
[16] Narten A H and Levy H A 1972 *The Physics and Physical Chemistry of Water* **1** 311
[17] Sorenson J M, Hura G, Glaeser R M and Head-Gordon T 2000 *J. Chem. Phys.* **113** 9149
[18] Head-Gordon T and Hura G 2002 *Chem. Rev.* **102** 2651

[19] Kim T K *et al* 2006 *Proc. Nat. Acad. Sci.* **103** 9410
[20] Lin Z and Zhigilei L V 2006 *Phys. Rev.* B **73** 184113
[21] Gutiérrez G and Johansson B 2002 *Phys. Rev.* B **65** 104202
[22] Penfold T J, Tavernelli I, Abela R, Chergui M and Rothlisberger U 2012 *New J. Phys.* **14** 113002
[23] Köfinger J and Hummer G 2013 *Phys. Rev.* E **87** 052712
[24] Møller K B and Henriksen N E 2012 *Structure and Bonding* **142** 185
[25] Livet F 2006 *Acta Cryst.* A **63** 87
[26] Coppens P 1992 *Ann. Rev. Phys. Chem.* **43** 663
[27] Northey T, Zotev N and Kirrander A 2014 *J. Chem. Theory Comput.* **10** 4911
[28] Haldrup K, Christensen M and Nielsen M M 2010 *Acta Crystallogr.* A **66** 261
[29] Haldrup K and Nielsen M 2014 *Measuring and Understanding Ultrafast Phenomena using X-rays* (*NATO Science for Peace and Security Series A: Chemistry and Biology*) (Springer Science+Business Media B.V.) 91–113 ISBN 978-94-017-8549-5
[30] Henriksen N E and Møller K B 2008 *J. Phys. Chem.* B **112** 558
[31] Lorenz U, Møller K B and Henriksen N E 2010 *New J. Phys.* **12** 113022
[32] Baskin J S and Zewail A H 2005 *ChemPhysChem* **6** 226
[33] Cromer D T and Mann J B 1968 *Acta. Crystallogr.* A **24** 321
[34] Grübel G and Zontone F 2004 *J. Alloys Compd.* **362** 3
[35] Dierker S 1997 *Light Scattering and Photon Correlation Spectroscopy* (*NATO ASI Series* vol. 40) ed E Pike and J Abbiss (Netherlands: Springer) 65–78 ISBN 978-94-010-6355-5
[36] Abernathy D L, Grübel G, Brauer S, McNulty I, Stephenson G B, Mochrie S G J, Sandy A R, Mulders N and Sutton M 1998 *J. Synchrotron Radiat.* **5** 37
[37] Beutier G, Marty A, Livet F, van der Laan G, Stanescu S and Bencok P 2007 *Rev. Sci. Instrum.* **78** 093901
[38] Nugent K A 2009 *Adv. Phys.* **59** 1
[39] Hruszkewycz S O *et al* 2012 *Phys. Rev. Lett.* **109** 185502
[40] Dohn A O, Jónsson E O, Kjær K S, van Driel T B, Nielsen M M, Jacobsen K W, Henriksen N E and Møller K B 2014 *J. Phys. Chem. Lett.* **5** 2414
[41] Canton S E *et al* 2015 *Nat. Commun.* **6** 6359
[42] Narten A H, Venkatesh C G and Rice S A 1976 *J. Chem. Phys.* **64** 1106
[43] Peterson P F, Božin E S, Proffen T and Billinge S J L 2003 *Applied Crystallogr.* **36** 53
[44] Lee J H, Kim K H, Kim T K, Lee Y and Ihee H 2006 *J. Chem. Phys.* **125** 174504
[45] Skinner L B, Huang C, Schlesinger D, Pettersson L G M, Nilsson A and Benmore C J 2013 *J. Chem. Phys.* **138** 074506
[46] Horn H W, Swope W C, Pitera J W, Madura J D, Dick T J, Hura G L and Head-Gordon T 2004 *J. Chem. Phys.* **120** 9665
[47] Hura G, Sorenson J M, Glaeser R M and Head-Gordon T 2000 *J. Chem. Phys.* **113** 9140
[48] Hura G L, Russo D, Glaeser M, Head-Gordon T, Krack M and Parrinello M 2003 *PysChemChemPhys.* **5** 1981
[49] Kong Q, Kim J, Lorenc M, Kim T K, Ihee H and Wulff M 2005 *J. Phys. Chem.* A **109** 10451–8

IOP Publishing Journal of Physics B: Atomic, Molecular and Optical Physics
J. Phys. B: At. Mol. Opt. Phys. **49** (2016) 059501 (1pp) doi:10.1088/0953-4075/49/5/059501

Corrigendum: On the calculation of x-ray scattering signals from pairwise radial distribution functions (2015 *J. Phys. B: At. Mol. Opt. Phys.* 48 244010)

Asmus O Dohn[1], Elisa Biasin[2], Kristoffer Haldrup[2], Martin M Nielsen[2], Niels E Henriksen[1] and Klaus B Møller[1]

[1] Department of Chemistry, Technical University of Denmark, Kemitorvet 207, DK-2800, Kgs. Lyngby, Denmark
[2] Department of Physics, Technical University of Denmark, Fysikvej 307, DK-2800, Kgs. Lyngby, Denmark

E-mail: asod@kemi.dtu.dk and kbmo@kemi.dtu.dk

When we in equation (20) split up the scattering signal into contributions from solvent-solvent terms, solute-solvent (cross) terms, and solute-solute terms, each atom (type) belongs to either the solvent or the solute. Hence, the scattering signal contribution form the solute-solvent (cross) terms, equation (20*b*), should read:

$$S_c(q) = 2\sum_{l}^{u}\sum_{m}^{v} f_l(q) f_m(q) \frac{N_l N_m}{V} 4\pi \times \int_0^{R_{box}} r^2 \left[g_{l,m}(r) - 1 \right] \frac{\sin(qr)}{qr} \mathrm{d}r. \qquad (20b)$$

Paper II

Faraday Discussions

Cite this: *Faraday Discuss.*, 2015, **177**, 443

PAPER

View Article Online
View Journal | View Issue

Disentangling detector data in XFEL studies of temporally resolved solution state chemistry

Tim Brandt van Driel,[a] Kasper Skov Kjær,[ab] Elisa Biasin,[a] Kristoffer Haldrup,[a] Henrik Till Lemke[c] and Martin Meedom Nielsen*[a]

Received 14th October 2014, Accepted 5th November 2014
DOI: 10.1039/c4fd00203b

With the arrival of X-ray Free Electron Lasers (XFELs), 2D area detectors with a large dynamic range for detection of hard X-rays with fast readout rates are required for many types of experiments. Extracting the desired information from these detectors has been challenging due to unpredicted fluctuations in the measured images. For techniques such as time-resolved X-ray Diffuse Scattering (XDS), small differences in signal intensity are the starting point for analysis. Fluctuations in the total detected signal remain in the differences under investigation, obfuscating the signal. To correct such artefacts, Singular Value Decomposition (SVD) can be used to identify and characterize the observed detector fluctuations and assist in assigning some of them to variations in physical parameters such as X-ray energy and X-ray intensity. This paper presents a methodology for robustly identifying, separating and correcting fluctuations on area detectors based on XFEL beam characteristics, to enable the study of temporally resolved solution state chemistry on the femtosecond timescale.

1. Introduction

The introduction of X-ray Free Electron Lasers (XFELs) has brought many X-ray techniques into a new regime. Unprecedented X-ray peak brilliance and exceptionally short pulse lengths make it possible to use X-rays to study many new phenomena, such as those occurring on time-scales shorter than atomic movement,[1] measure processes before heat effects and radiation-damage set in,[2] as well as using exceptional transverse coherence to probe nanoparticles.[3]

Along with new X-ray source and beam characteristics come a number of new challenges that have to be addressed. Among these challenges is the design and use of area detectors capable of operating at high readout rates as well as accurately

[a]*Molecular Movies, Department of Physics, Technical University of Denmark, 2800 Kgs. Lyngby, Denmark. E-mail: mmee@fysik.dtu.dk; Tel: +45 25 32 26*
[b]*Chemical Physics Department, Lund University, PO Box 124, S-22100 Lund, Sweden*
[c]*LCLS, SLAC National Laboratory, Menlo Park, California 94025, USA*

measuring X-rays in a large dynamic range for each individual X-ray pulse. The stochastic nature of the Self-Amplified Spontaneous Emission (SASE) process in XFELs results in significant pulse-to-pulse variation in both intensity, energy and time. Here, we present time-resolved X-ray diffuse scattering (XDS) from one of the first XDS experiments at the Linac Coherent Light Source (LCLS), measured with the first version of the Cornell-SLAC Pixel Array Detector (CSPAD), at the X-ray pump–probe beamline (XPP) at the LCLS. Upon analyzing XDS of solution samples measured with the CSPAD it was realized that the quality of the measurements was not limited by counting statistics, but instead limited by a number of fluctuating artefacts present in the measured scattering signals. Several different approaches to sort and filter the data have been applied with some success[4,5] but have not made it possible to model or explain the observed artefacts until now.

Here, we present a method to identify and remove some of these fluctuations. The method relies on using singular value decomposition (SVD) on a large number of reference images measured during typical XDS experiments. From such a subset of the measured data it is possible to use SVD to identify particular, characteristic, fluctuations in the detector signal. Further, these fluctuations can be directly correlated with variations in beam parameters such as X-ray energy and pulse intensity, which are measured simultaneously with the scattering data. Based on this analysis it is shown how the identified correlation between the observed fluctuations and the beam-parameter variations can be utilized to efficiently correct scattering images on an image-to-image basis prior to analysis.

2. XDS experiments

This paper is based on a typical pump–probe XDS experiment at the XPP beamline at LCLS. A liquid water sample is pumped through a sapphire nozzle producing a 100 μm liquid sheet that is continuously renewed and returned to a sample reservoir. The liquid jet ensures fresh sample for every pump–probe event in the interaction volume where the pump laser and probe X-rays are overlapped in time and space. The sample was repeatedly pumped with 1950 nm laser pulses, and probed with the XFEL X-ray pulses at 120 Hz. A series of time-delays were measured to study the temporal response of water-heating on ultra-fast time-scales by collecting the diffuse scattering on an area detector (seen in Fig. 1).

Subtracting the un-pumped scattering images from the pumped results in difference-scattering images that can be azimuthally integrated to create 1D difference scattering curves $\Delta S(Q)$, where $Q = \frac{4\pi \sin(\theta)}{\lambda}$, 2θ is the scattering angle and λ is the wavelength. These curves can then be used to analyse the photo-induced structural changes in the sample. The procedure for conducting a full structural analysis of the XDS data is covered elsewhere.[6,7] Here we present a methodology to identify undesired signal fluctuations and create corrections, that, when applied to the individual images, yield a corrected dataset suitable for analysis.

3. The 2D CSPAD

Many X-ray experiments require 2D area detectors in order to measure scattering or dispersed spectral signals.[8] These 2D detectors need a large dynamic range to

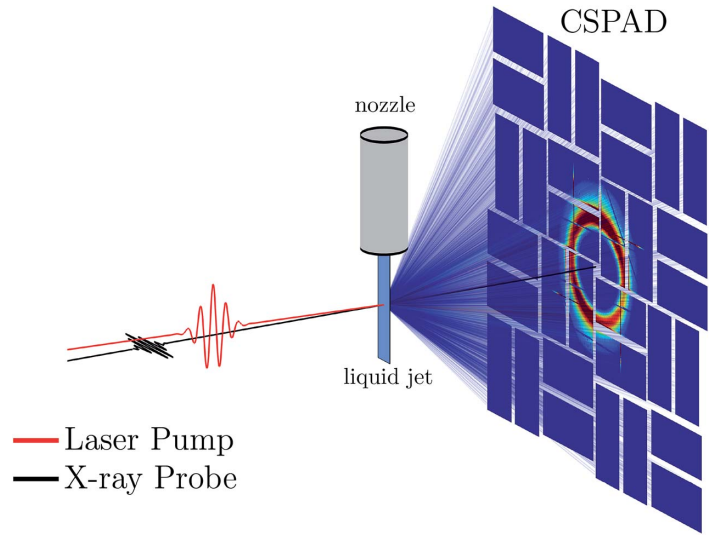

Fig. 1 A schematic of the experimental time-resolved XDS setup at XPP. The CSPAD is mounted downstream from the liquid jet, covering scattering angles up to 45°. Additionally the beam path and sample environment is mounted in a He filled chamber reducing the unwanted air scattering background as well as protecting the sample.

meet the requirements for many different techniques; from single photon detection[9–11] to many integrated photons/pixel,[12] in an energy range extending from soft to hard X-rays. At LCLS, the CSPAD[13] was constructed to satisfy these requirements for the Coherent X-ray Imaging (CXI) and XPP beamlines. Table 1 shows some of the technical specifications.

This 14 bit, 16 384 Analogue to Digital Units (ADU) detector has two different gain modes changing the sensitivity by a factor of 7. For XDS experiments using the full polychromatic X-ray beam, the low gain mode is necessary in order to avoid saturation. The large area detector shown in Fig. 1 consists of ~2.3 million

Table 1 Specifications of the CSPAD. Adapted from (ref. 12). The ADU/photon and readout noise are extracted from histograms of single photon counting on the CSPAD

Single ASIC	185 × 194 pixels	
Single tile	185 × 388 pixels	
Large 32 tile CSPAD	1516 × 1516 pixels	2.3 megapixel
Pixel size	110 × 110 μm	
Detector area	18.5 × 18.5 cm	
Frame rate	120 Hz	
	High Gain	**Low Gain**
Pixel saturation	350 photons	2700 photons
ADU/Photon@8 keV	~40 ADU	~5 ADU
Readout noise	~20 ADU	~5 ADU

silicon diodes arranged on 32 individual detector tiles. The diodes on each half-tile are read out by individual Application Specific Integrated Circuits (ASICs). The CSPAD tiles are arranged in a square, divided into 4 different quadrants. The centre of the detector has a hole, allowing the direct beam to pass through. Fig. 2 (a) shows a typical raw X-ray scattering image from water as recorded on the CSPAD. This raw image consists of the scattered intensity on top of a background. This background, sometimes called the dark image or dark current, is given by the intensity measured on the detector without incident X-rays. It can be measured independently and subsequently subtracted from the raw images prior to analysis.

In Fig. 2 the pixel intensities are plotted in the lab space coordinates and the gaps between the tiles as well as the central hole are evident from the lack of pixels. From the raw image (a), the dark image (b) containing the background intensities measured with no incident X-rays is subtracted. This contribution accounts for ~1800 ADU per pixel, reducing the dynamic range of the 14 bit detector by ~10% when subtracted. The standard deviation of 1000 dark images can be seen in (c) showing the tile-wise variation in readout noise. A mask (d) is necessary to remove unreliable pixels. In the early measurements, a grid of metal wires was placed on the CSPAD in an attempt to measure and correct for fluctuations. Pixels shadowed by this grid are also masked out, as are pixels that show significant deviations in total intensity, fluctuations or signal-to-noise between consecutive, nominally identical, measurements. After masking the image and subtracting the dark image, the XDS image shows a characteristic liquid ring on a weak background as seen in (e). Azimuthal integration of such isotropic XDS images reduces the data to 1D scattering curves $S(Q)$ without loss of information (f).

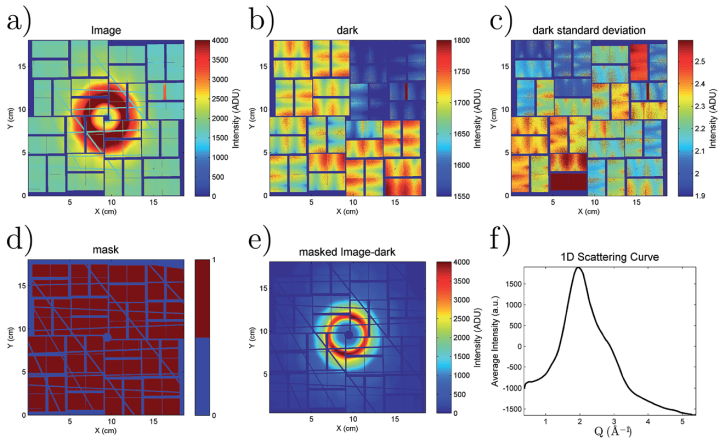

Fig. 2 CSPAD images showing: (a) Raw XDS image, (b) dark image, (c) standard deviation of 1000 dark images, (d) mask, (e) dark subtracted and masked XDS image of water and (f) azimuthally integrated scattering curve.

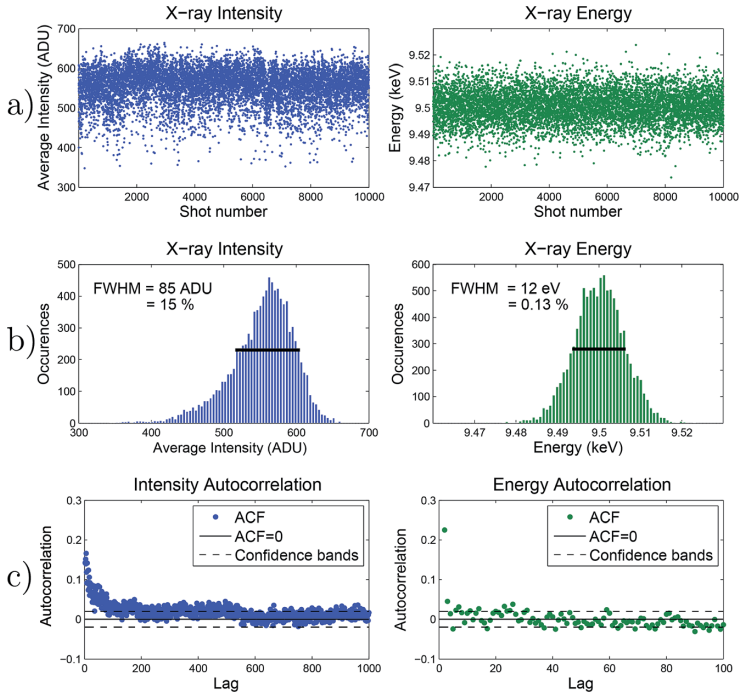

Fig. 3 The X-ray intensity and energy are measured for each X-ray shot (a). Histograms of the readout values allow for determining the FWHM of the intensity and energy distribution (b). The autocorrelation function of the intensity and energy show the time correlation of consecutive shots, confidence bands are added to evaluate when a significant autocorrelation is no longer present.

4. X-ray free electron lasers

The LCLS utilizes Self-Amplified Spontaneous Emission (SASE) to produce short bursts of intense X-rays at 120 Hz. The typical pulse has a duration of tens of fs with up to 2×10^{12} photons/pulse, which is many orders of magnitude higher in peak-brilliance than synchrotron X-ray pulses.[14] Due to the stochastic nature of the SASE process[15] the resulting XFEL pulses fluctuate in pulse intensity and X-ray energy. Furthermore, significant fluctuations have been identified in the pump–probe arrival time. The X-ray energy, intensity and timing fluctuations are discussed in more detail in the following and are shown in Fig. 3 and 4.

4.1. X-ray intensity

The X-ray intensity is measured as the integrated intensity on the CSPAD. Intensity Position Monitors (IPMs) are also available along the beam path, but require non-linear diode corrections.[16] The intensity fluctuations of the full polychromatic beam can be seen in Fig. 3 (a–c) where the average intensity is observed to fluctuate with 78 ADU (FWHM) corresponding to 14%.

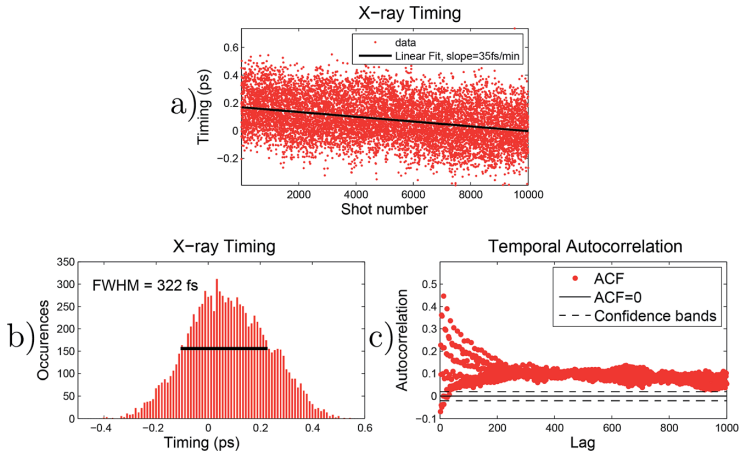

Fig. 4 The timing jitter is read out for each X-ray/laser shot (a) and the long term drift is fit with a linear slope of 35 fs min^{-1}. Histograms of the readout values allows for determining the FWHM of the timing jitter (b). The autocorrelation function of the timing shows the time correlation of consecutive shots, confidence bands are added to evaluate when a significant autocorrelation is no longer present. The autocorrelation of the timing shows significant autocorrelation as well as long term drifts.

The Autocorrelation Function (ACF) measures the correlation between observations at different times as a function of separation distance, or lag.[17]

As seen in Fig. 3 panel (c) the ACF of the X-ray intensity decays rapidly, approaching zero within 100 lags. However, the autocorrelation still remains larger than the confidence bands at late lags, thereby showing some correlation between intensity measurements with significant separation (several seconds) in time.

4.2. X-ray energy

As opposed to the X-ray undulator spectrum at a synchrotron, the XFEL SASE spectrum is narrow-band and exhibits spiky features with significant shot-to-shot variation. Detection schemes are currently being developed for determining the X-ray spectrum on a pulse to pulse basis.[18] Until such is available it is possible to estimate the pulse-to-pulse centre of mass X-ray energy from the electron beam energy. The energy histogram in Fig. 3 has a 12 eV FWHM corresponding to a 0.13% bandwidth at the nominal energy of 9.5 keV. The ACF of the X-ray energy shows no significant autocorrelation after a few lags, in contrast to the long-lived autocorrelation of the X-ray intensity.

4.3. X-ray timing

Both the X-ray and optical laser produce pulses at a 120 Hz frequency, in the following we describe the time jitter, which is the pulse-to-pulse deviation in actual pump–probe time difference from the nominal time difference Δt. The

effective time resolution of the ~50 fs X-ray duration and ~70 fs laser duration is decreased by a large temporal jitter. The X-ray/laser time jitter is the combined jitter of both X-ray and laser pulse arrival time and was a significant challenge for the first time-resolved XFEL experiments. This has been solved at LCLS with the implementation of a timing tool.[1,19,20] The timing tool determines the arrival time of the X-ray with respect to the optical laser. Fig. 4 shows the time jitter for 10.000 shots and quantifies the variation similarly to the X-ray intensity and energy in Fig. 3. The time-jitter is 322 fs at FWHM and the timing tool allows us to measure the delay with ~15 fs accuracy.[1] The autocorrelation of the timing displays complicated behaviour, but the general trends can be separated into two different time-scales. The autocorrelation reflects the laser timing feedback loop giving a systematic correlation/anti-correlation between close shots, seen for the first 200 lags. Additionally the long term time drift results in a positive autocorrelation throughout the plot. A linear fit to the long time drift results in a drift of 35 fs min^{-1} corresponding to a timing drift of 2.1 ps $hour^{-1}$.

The data presented here are measured with the implemented timing tool[1] which will not be covered further in this paper.

4.4. Other parameters

In addition to the three parameters described above, others may also vary. From experience it has been established that the X-ray position fluctuates up to 20 μm. For the presented XDS experiment this is not a concern as the sample is a liquid sheet, homogeneous on distances much larger than the position fluctuations, as well as 20 μm being significantly smaller than the dimensions of the pixels of the detector.

5. Detector fluctuations

As described below, the CSPAD displays a number of different fluctuations. Among these, tiles and quadrants exhibit so called common-mode fluctuations, where a common offset in intensity is measured in a particular well-defined part of the detector such as a tile or quadrant. Additionally each tile on the detector shows some spatial dependence in the noise behaviour, as shown above in the standard deviation of the dark measurements, see Fig. 2.

A linear area detector can in most cases be calibrated by subtracting a pixel-resolved dark background and measuring the individual pixel gain. The dark background provides a constant intensity offset when no X-rays are incident, and the individual pixel gain must be corrected, ensuring that each pixel has the same absolute scaling. This is described by eqn (1), where I is the pixel intensity.

$$I_{\text{corrected}} = (I_{\text{measured}} - I_{\text{dark}}) \times \text{gain} \quad (1)$$

This description does not account for the observed fluctuations, but the observed fluctuations can be quantified as a deviation from this equation.

In the following sections we address fluctuations due to variations in X-ray energy and intensity. Plotting the X-ray energy against the X-ray intensity (see Fig. 5) shows that these two beam parameters are uncorrelated. Any fluctuations caused by either of these individual parameters can therefore be considered independently, making them easier to identify and separate.

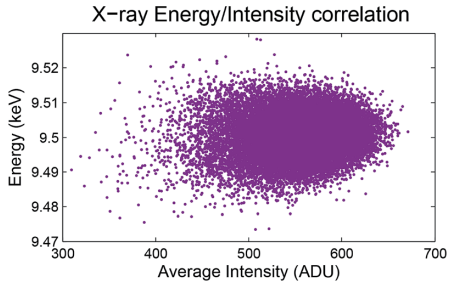

Fig. 5 X-ray beam energy plotted as a function of average intensity measured on the CSPAD for 23 000 shots. No correlation between these two beam parameters is evident.

In the following we investigate the relationships between variations in beam parameters and fluctuations in the signal observed on the CSPAD. Towards this goal we use Singular Value Decomposition (SVD)[21] as a tool to separate and identify characteristic detector fluctuations. In the case of non-linear/non-proportional detector behaviour, energy and intensity dependent signal fluctuations can conceivably be removed if a parametric model for the detector response as a function of X-ray intensity or energy can be established. Eqn (2) describes a detector correction scheme based on identified relationships between beam parameters and detector response.

$$I_{\text{corrected}} = I_{\text{measured}} - I_{\text{dark}} - \sum_i f_i(I) I_i^{\text{SVD}} - \sum_e f_e(E) I_e^{\text{SVD}} \quad (2)$$

By using SVD to identify fluctuating components (I^{SVD}) in combination with analysis of the relationship between each such component and key beam parameters, it may be possible to assign some of these to X-ray intensity variation (I_i^{SVD}) and some to variation in X-ray energy (I_e^{SVD}). Further, by establishing the parametric models $f_i(I)$ and $f_e(E)$ for the relationship between beam variations (E, I) and detector response (I_i^{SVD}, I_e^{SVD}), it is possible to correct for the undesired intensity and energy dependent behaviour solely based on the beam parameters, resulting in the corrected scattering $I_{\text{corrected}}$.

6. Singular value decomposition

SVD is a powerful tool to decompose a 2D matrix into orthogonal components. It is often used to extract the principal components as well as their kinetics from a time-series of spectra.[22] The large set of images acquired during an XDS experiment can be reshaped into such a 2D matrix. Fig. 2 shows how a set of acquired detector images can be recast as a 2D matrix amenable to SVD analysis. This is done by reorganizing each image into a vector of pixels and placing each image vector in a new column of the resulting [Data] matrix as shown in Fig. 6. Using SVD, the [Data] matrix is then decomposed into the product of U, an $m \times m$ set of orthonormal basis vectors, S, an $m \times n$ rectangular diagonal matrix and V^{T}, an $n \times n$ unitary matrix.

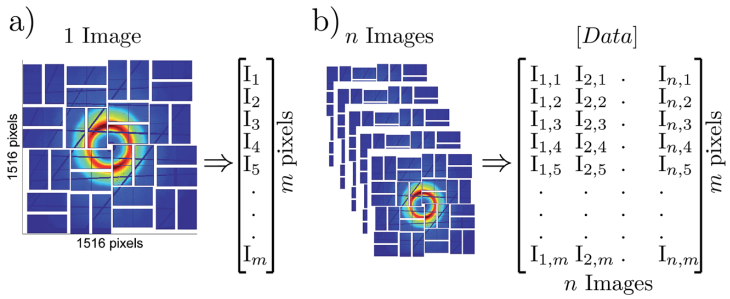

Fig. 6 (a) The individual images containing 2 296 960 pixels are reorganized into long vectors and (b) multiple images are reorganized into a large [Data] matrix.

$$[\mathrm{Data}] = USV^{\mathrm{T}} \tag{3}$$

The images contained in [Data] are decomposed into a number of significant image components, contained in the columns of U. The corresponding amplitude of each component in the different images, is given by SV^{T}. For typical XFEL XDS experiments n and m are of the order of 10^4 and 10^6, respectively, making the construction of [Data] and the SVD analysis computationally quite intensive. However, as the columns of U contain the orthonormal components in decreasing order of $S(i, i)$, it is possible to select a cutoff i_{r} after which the contribution of the following components is judged to be sufficiently small. This reduced-rank approximation of the data limits the calculation to a "thin" SVD decomposition, where only the first r components are computed. The thin SVD limits the size of the resulting U, S and V^{T} to $m \times r$, $r \times r$ and $r \times n$, greatly reducing the computational cost and size of the decomposed matrix.

Still, the SVD computation requires the entire [Data]-matrix to be present in computer memory. Even though the thin SVD reduces the size of the resulting U, S, V, the size of the [Data]-matrix makes the thin SVD infeasible on a normal PC. However, it is possible to calculate a thin low-rank SVD from a subset of [Data] and update it incrementally[23] using MATLAB® code implemented by D. Wingate,[24] as briefly described here. Given the SVD of $[X]$, a subset of the columns in the [Data]-matrix,

$$[X] = USV^{\mathrm{T}} \tag{4}$$

$[X]$ can be updated to include a further partition of the columns in the [Data]-matrix, $[A]$, to yield updated U, S and V, denoted U_{p}, S_{p} and $V_{\mathrm{p}}^{\mathrm{T}}$ such that

$$[XA] = U_{\mathrm{p}}S_{\mathrm{p}}V_{\mathrm{p}}^{\mathrm{T}}. \tag{5}$$

This makes it possible to iteratively process the entire dataset in smaller partitions.

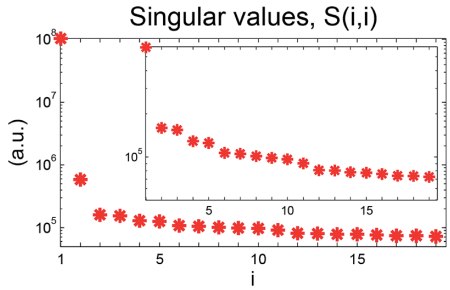

Fig. 7 The singular values of the diagonal $S(i, i)$ from the thin SVD of rank 20, for i 1–20. The inset shows a zoom of i 2–20.

7. Singular value decomposition of CSPAD data

In order to characterise the detector, a set of steady-state (un-pumped), dark-subtracted and masked images is used. These steady-state images are nominally identical measurements regularly inter-spaced in the data acquisition sequence, and thus contain the same detector fluctuations present in the time-resolved data. Usually, every 2nd–10th acquired image is such a reference, yielding a total of $\sim 10^4$ such reference images for a typical data acquisition. This set of reference data acquired with no laser excitation of the sample can be utilized as a separate dataset probing the detector response under the exact same experimental conditions as the time-resolved part of the acquisition sequence.

For the dataset described in this article, every fifth image was acquired with no laser pulse arriving at the sample. Following dark-subtraction and masking, these images were utilized in the detector characterization described in detail in the following. Here, we present the result of the thin SVD of those $\sim$5000 reference images of neat water. The rank cutoff was set to 20, and as Fig. 7 shows, the relative contribution of the components of rank greater than 10 are more than three orders of magnitude less than the primary component. Based on this observation, we consider a cutoff of 20 to be quite conservative and observe that the total contribution of excluded components account for less than 1×10^{-5} percent of the full dataset. We thus regard this reduced representation of the acquired data as fully adequate to describe all salient parts of the detector response.

Fig. 8–11 characterize the first 8 components of U as obtained from the SVD decomposition. Turning first to panel (a) of Fig. 8, this shows the components in U re-plotted onto the detector coordinates. The left column contains the first component, and shows a reassuringly close likeness to the dark-subtracted image in Fig. 2. Turning next to the right-hand column of Fig. 8 as a representative example of these rather complex datasets, panel (a) shows the second SVD component, column two of U. Referring to Fig. 7, this second component accounts for about 1% of the signal in the series of reference images. Panel (b) shows the azimuthal integration of this component compared to the azimuthal integration of the averaged images. Panels (c) and (d) show plots of the amplitude

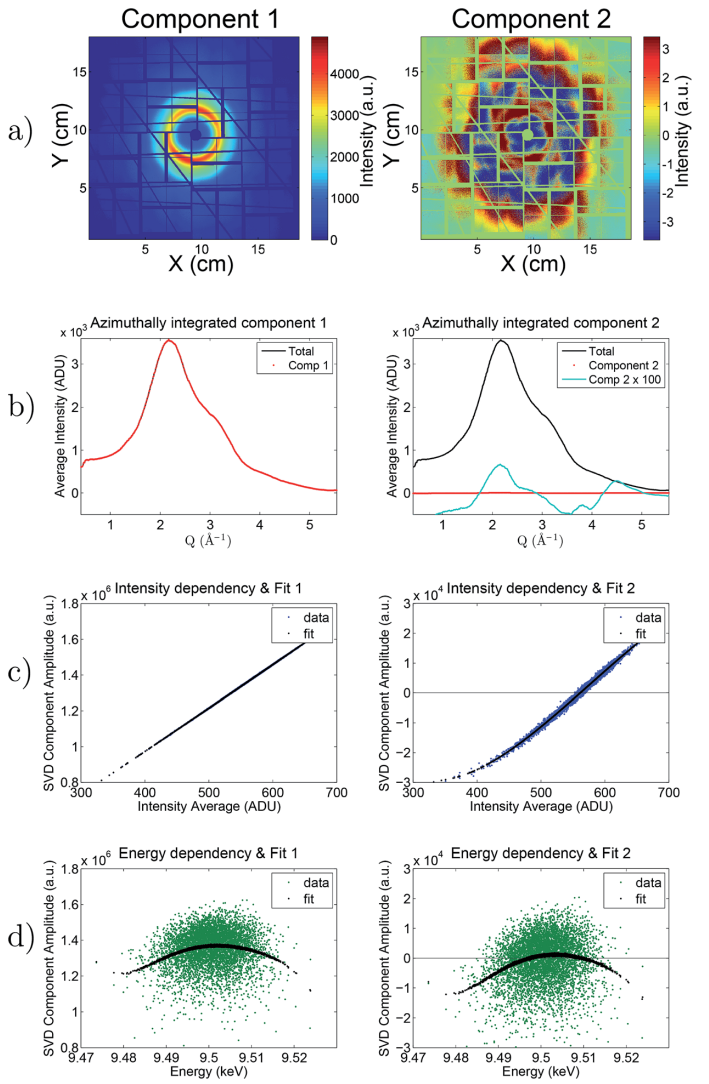

Fig. 8 Results of the SVD analysis of the data matrix, showing the first two components and their amplitude *versus* X-ray pulse intensity and X-ray pulse energy. The *U* components multiplied by their mean absolute amplitude have been mapped to the detector geometry in (a). Panel (b) shows the azimuthal integration of the image in (a) (red trace), compared with the azimuthal integration of the average image (black trace). Cyan trace shows the red trace scaled up for visibility. Panel (c) shows the amplitude of the *U* component plotted against X-ray pulse intensity, and panel (d) shows the amplitude of the *U* component plotted against X-ray pulse energy. Component 1 represents the linear response of the CSPAD seen from the linear intensity dependency. Component 2 describes a non-linear intensity dependency, as seen from panel (c).

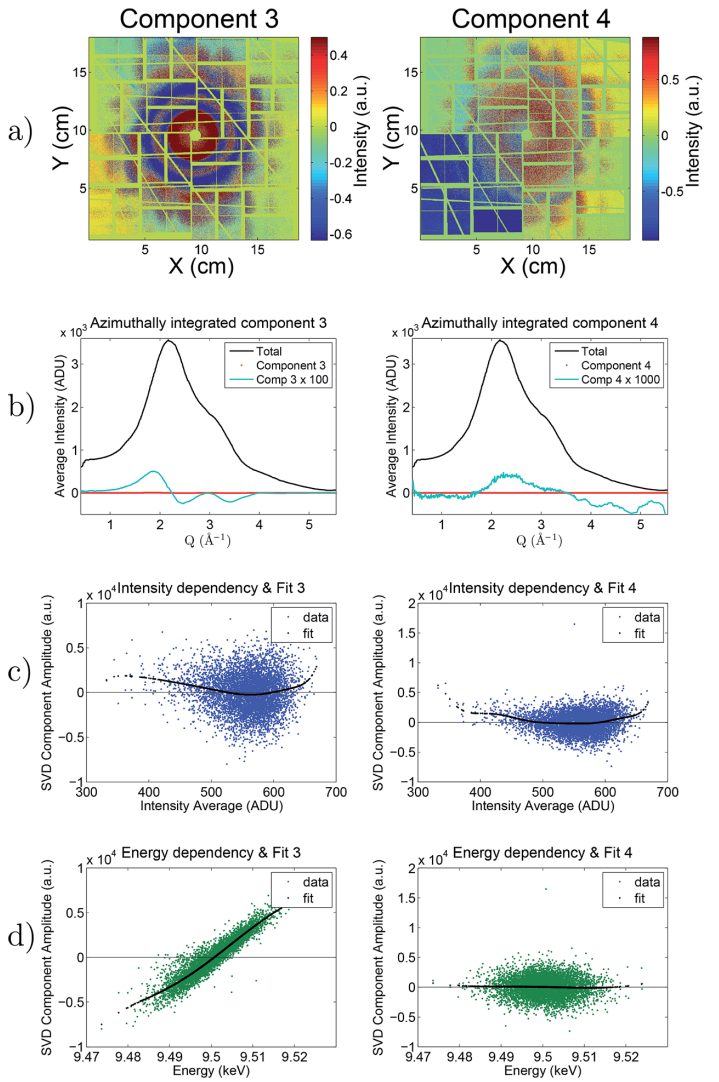

Fig. 9 Results of the SVD analysis of the data matrix, showing components 3 and 4 and their amplitude *versus* X-ray pulse intensity and X-ray pulse energy. The *U* components multiplied by their mean absolute amplitude have been mapped to the detector geometry in (a). Panel (b) shows the azimuthal integration of the image in (a) (red trace), compared with the azimuthal integration of the average image (black trace). Cyan trace shows the red trace scaled up for visibility. Panel (c) shows the amplitude of the *U* component plotted against X-ray pulse intensity, and panel (d) shows the amplitude of the *U* component plotted against X-ray pulse energy. Component 3 describes the X-ray energy dependency of the detector, seen from panel (d). Component 4 describes a random quadrant fluctuation and correlates poorly with X-ray intensity and energy.

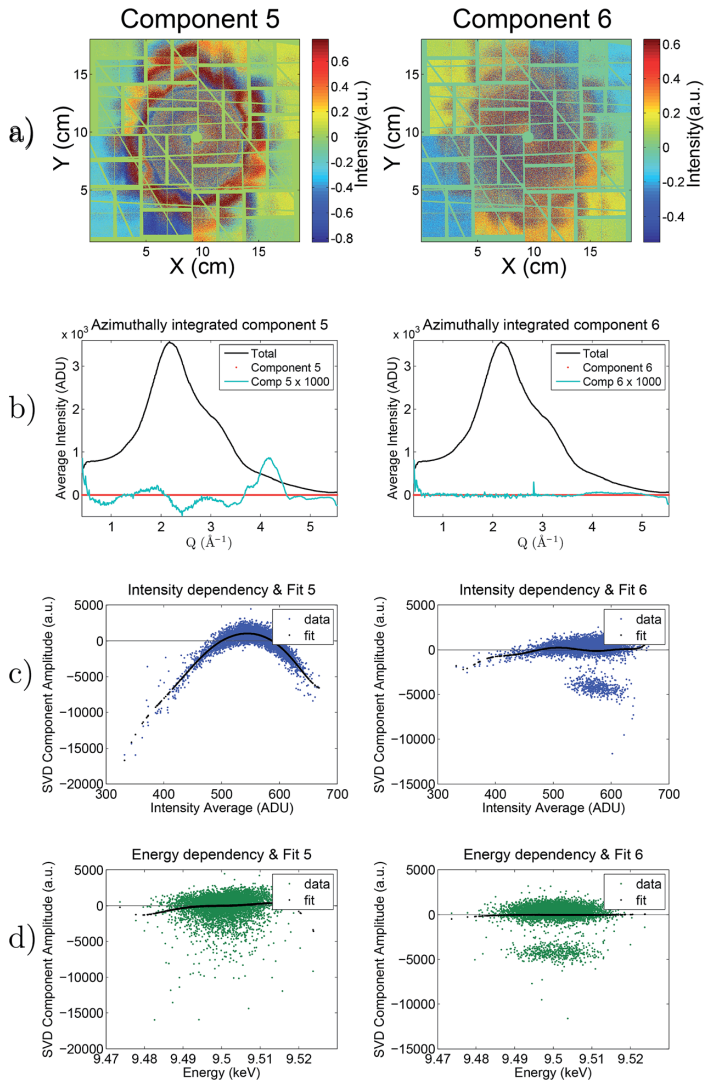

Fig. 10 Results of the SVD analysis of the data matrix, showing components 5 and 6 and their amplitude *versus* X-ray pulse intensity and X-ray pulse energy. The *U* components multiplied by their mean absolute amplitude have been mapped to the detector geometry in (a). Panel (b) shows the azimuthal integration of the image in (a) (red trace), compared with the azimuthal integration of the average image (black trace). Cyan trace shows the red trace scaled up for visibility. Panel (c) shows the amplitude of the *U* component plotted against X-ray pulse intensity, and panel (d) shows the amplitude of the *U* component plotted against X-ray pulse energy. Component 5 correlates with the pulse intensity and together with component 2 it describes the non-linear intensity response. Component 6 shows no clear intensity or energy dependency and resembles common-mode tile fluctuations, as seen in panel (a).

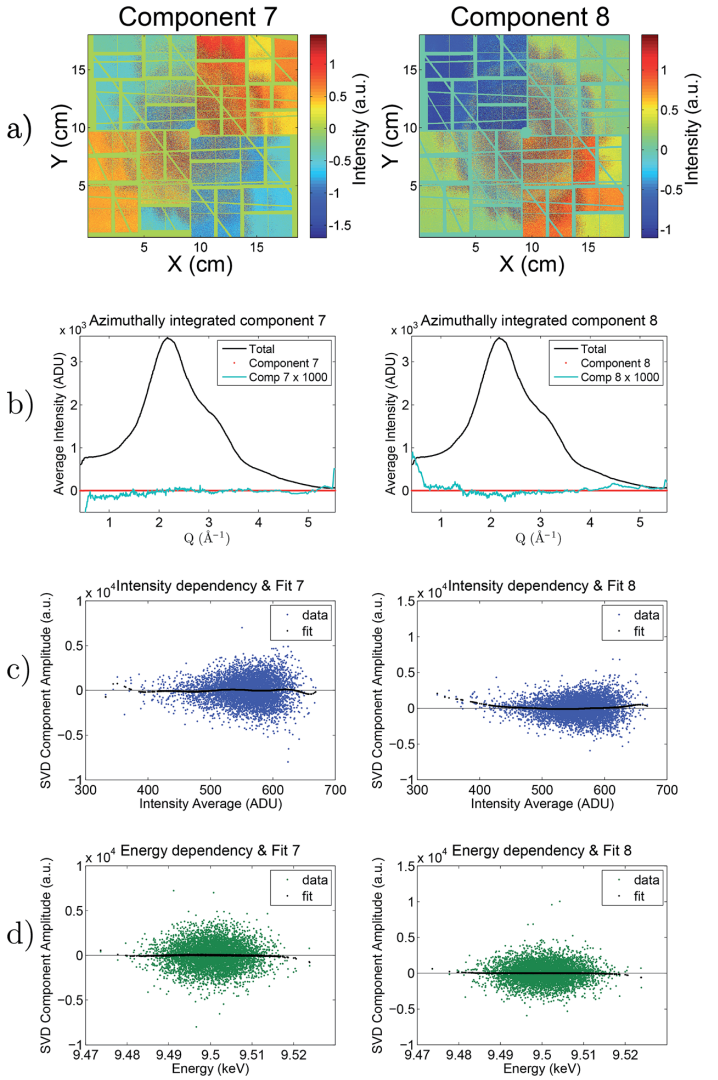

Fig. 11 Results of the SVD analysis of the data matrix, showing components 7 and 8 and their amplitude *versus* X-ray pulse intensity and X-ray pulse energy. The *U* components multiplied by their mean absolute amplitude have been mapped to the detector geometry in (a). Panel (b) shows the azimuthal integration of the image in (a) (red trace), compared with the azimuthal integration of the average image (black trace). Cyan trace shows the red trace scaled up for visibility. Panel (c) shows the amplitude of the *U* component plotted against X-ray pulse intensity, and panel (d) shows the amplitude of the *U* component plotted against X-ray pulse energy. Components 7 and 8 show no clear intensity or energy dependency and resemble common-mode fluctuations of a similar nature to components 4 and 6, as seen in panel (a).

of this component against the X-ray intensity and the X-ray energy for every image in the series of reference images. Panel (d) shows no correlation between the X-ray energy and the amplitude of component 2. Panel (c), on the other hand, shows a clear intensity dependency. The black points in this plot represent a polynomial fit to the data points, thus providing a parametric description of the magnitude of this component, I_2^{SVD} as a function of X-ray beam intensity. The polynomium describes $f_2(I)$ in eqn (2), identifying and characterizing a non-linear intensity dependency in the CSPAD response.

Continuing to component 3, shown in the left hand column of Fig. 9, panel (a) again maps the component onto the detector coordinates. Panel (b) shows the same component, azimuthally integrated. Component 3 does not correlate with the intensity (panel (c)) but has a clear correlation with the X-ray beam energy (panel (d)) and again the black points represent a polynomium describing the dependency of this component on the X-ray energy. We note that the shape of the azimuthally integrated curve corresponds to a shift in Q of the scattering signal, further supporting the connection between this characteristic variation in the set of reference images and the X-ray beam energy.

Referring next to component 4 shown in Fig. 9, panel (b) shows a component predominantly localised on the lower left quadrant. This component does not correlate with the incoming intensity or energy and therefore cannot be corrected based on the X-ray intensity or energy.

7.1. Intensity and energy dependent components

In general, a component I_k^{SVD} is considered to be significantly correlated with either X-ray beam energy or X-ray beam intensity if either $f_k(I)$ or $f_k(E)$ can be described (fitted) by a p-order polynomial. In the analysis of the present dataset, $p = 9$ and the goodness of fit is determined by an R^2-measure. Which is based on inspection of typical fits and corresponding R^2 values for correlated components.

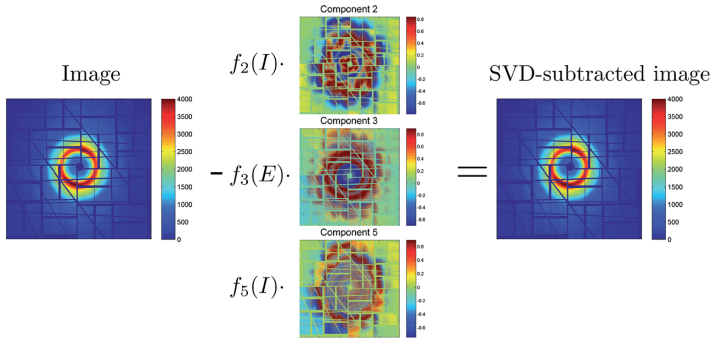

Fig. 12 Graphical representation of the correction of a single image. As discussed in the main text, three fluctuating components can be removed based on their individual intensity (I) and energy (E) dependencies, $f_2(I)$, $f_3(E)$ and $f_5(E)$. The effect of the ~1% corrections can be hard to see on the resulting image, but becomes highly evident when difference signals are calculated, as seen in Fig. 14.

Applying these criteria, we find that components 1, 2, 3 and 5 are significantly correlated with the beam parameters as follows.

The most significant SVD component, which is seen in Fig. 8, is observed to be directly proportional to the X-ray intensity, as expected if the incident X-ray intensity is fluctuating and the detector has a fully linear response. This component comprises 99% of the signal.

Component 2 accounts for 0.5% of the average signal, as seen from the ratio of the singular values for component 1 and 2 in Fig. 7. It can be seen from panel (c) that the amplitude of component 2 has a clear intensity dependency. Component 5 is likewise observed to have an intensity dependency. Thus components 2 and 5 describe a non-linear intensity response of the CSPAD. In order to correct for this behaviour, eqn (2) can be used where I_2^{SVD} and I_5^{SVD} are the second and fifth components in the columns of U and $f_2(I)$ and $f_5(I)$ are the polynomial fits to the intensity dependency of the two components, respectively.

The amplitude of component 3 is observed to be strongly correlated with the X-ray energy. Thus, the energy dependency described by component 3 can be corrected using I_3^{SVD} and $f_3(E)$ in eqn (2).

7.2. Other components

The remaining fluctuations described by components 4, 6, 7 and 8 contain clear contributions from common-mode behaviour in either quadrants or tiles. These components appear random in time and do not correlate with the incoming intensity or energy and therefore cannot be corrected based on the measured beam parameters. The remaining components 9–20 (not shown) describe similar apparently random common-mode fluctuations.

The lower left quadrant and especially one of the tiles in this quadrant often contribute significantly to these common-mode fluctuations. This matches the observation that the tiles in this quadrant also exhibit the largest fluctuations in the standard deviation of the dark images in Fig. 2. To reduce some of the observed fluctuations this specific tile and quadrant could be masked out, at the cost of counting statistics.

8. Image corrections

The detector correction is constructed based on the 3 intensity- or energy-correlated components 2, 3 and 5, resulting in a specific correction equation for this dataset based on eqn (2).

$$I_{\mathrm{corrected}} = I_{\mathrm{measured}} - I_{\mathrm{dark}} - \sum_{i=\{2,5\}} f_i(I) I_i^{\mathrm{SVD}} - \sum_{e=\{3\}} f_e(E) I_e^{\mathrm{SVD}} \quad (6)$$

where each image is corrected by subtracting the 3 individual contributions I^{SVD} weighted by their individual intensity and energy dependent correlation fits $f_i(I)$ and $f_e(E)$. This of course relies on knowing the X-ray beam energy and intensity for each image acquired in the measurement, but as discussed above this information is provided as part of the standard data stream at LCLS.

Fig. 12 shows the example correction of an image, where the three corrections are subtracted. The corrections are small compared to the total scattering, however these fluctuations become clear when studying small differences. In the

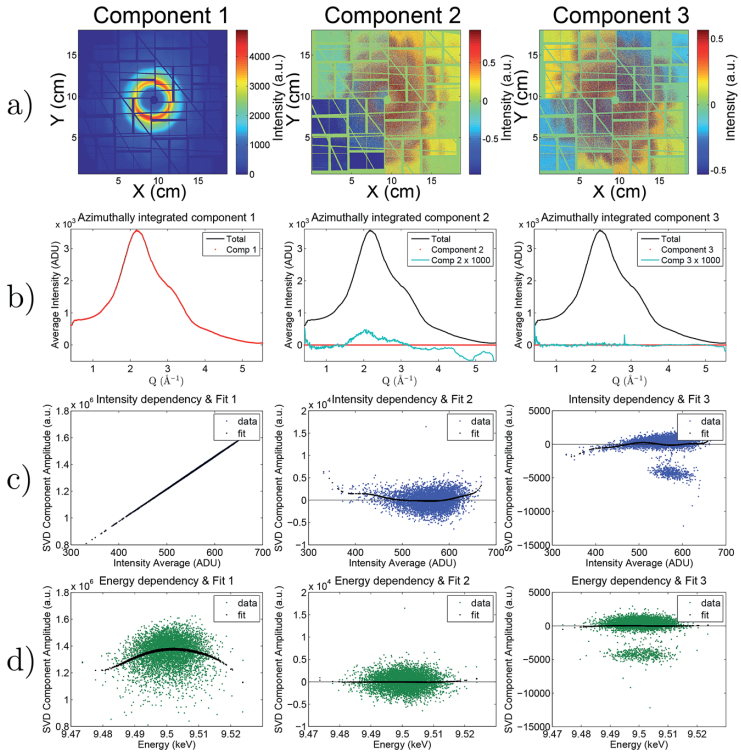

Fig. 13 Results of a second SVD analysis of the data matrix after subtracting artefacts based on the initial SVD analysis. The figure shows the first three components and their amplitude *versus* X-ray pulse intensity and X-ray pulse energy. The *U* components multiplied by their mean absolute amplitude have been mapped to the detector geometry in (a). Panel (b) shows the azimuthal integration of the image in (a) (red trace), compared with the azimuthal integration of the average image (black trace). Cyan trace shows the red trace scaled up for visibility. Panel (c) shows the amplitude of the *U* component plotted against X-ray pulse intensity, and panel (d) shows the amplitude of the *U* component plotted against X-ray pulse energy. The linear intensity dependency is described by component 1, where components 2 and 3 are the most significant remaining detector fluctuations. These two components are similar to components 4 and 6 seen in Fig. 9 and 10, respectively.

exemplified corrections in Fig. 12 the image has an average intensity of 554 ADU/pixel and the corrections account for an average of 0.6, 0.9 and 0.4 ADU/pixel for components 2, 3 and 5 respectively.

The successful correction of a given dataset can be verified by applying the corrections to the set of reference images and subsequently recalculating the singular value decomposition.

In Fig. 13 the resulting components from a second SVD are shown. The first component remains, and the second and third components resemble component

4 and 6 in the initial SVD, respectively. This shows the effective removal of the intensity- and energy-correlated components. After applying the corrections the observed fluctuations in the set of reference images is ten-fold smaller, with the most significant component accounting for only 0.1% of the variation. We note that in contrast to an effective, but ad-hoc method reported previously,[4] the artefact subtraction presented here allows for analysis of the underlying causes and additionally retains the full 2D images, allowing for analysis of anisotropic scattering signals.[25]

9. Artefact-subtracted difference signals

Typical time-resolved XDS investigations rely on analyzing difference scattering signals, obtained by subtracting unpumped scattering images from laser-pumped scattering images. As a starting point for such analysis, the acquired images are masked and corrected for setup specific effects such as X-ray polarization and X-ray absorption through the liquid sheet, as well as solid angle covered by each detector pixel. The images are then azimuthally integrated and scaled to produce 1D scattering curves. The difference scattering curves are then generated by subtracting an average of the two nearest references from each scattering curve.

Fig. 14 shows the output of this XDS data reduction scheme applied to the presented dataset, (a) without and (b) with the artefact subtraction introduced in the sections above. The full set of difference scattering curves (in total 20.000 individual pump–probe events) have had outliers removed[26] and are binned in ~10 fs steps to produce averaged difference scattering curves for each time delay,

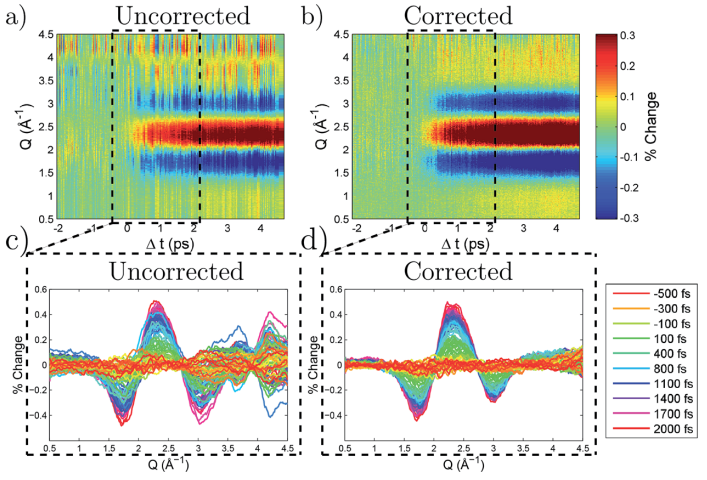

Fig. 14 Azimuthally integrated difference scattering curves as a function of time (a) following the established procedure for XDS data reduction.[27] (b) As the previous panel with the applied 2D corrections presented herein. Panels (c) and (d) show a zoom of −0.5 ps to 2 ps showing the 1D difference scattering curves of the uncorrected and corrected data. The 1D curves in (c) and (d) are smoothed with a 1%-wide moving-average filter.

$\Delta S(Q, \Delta t)$. Each bin contains 50 difference scattering curves. Apart from the artefact subtraction, the data in the two figures have been treated identically. Panels (c) and (d) show the individual difference scattering curves from −0.5 ps to 2 ps delays.

In comparison with Fig. 12, the effect of applying the SVD-based corrections is now highly evident. The artefact subtraction removes a large part of the fluctuations clearly evident in panel (a) and effectively makes it possible to analyse the signal in individual time-delay bins. This is prerequisite for robustly analyzing the sub ps signals from typical XDS experiments.

10. Gain correction

The corrections presented so far aim to correct the area detector down to a fully linear response. However, it is not a given that each of the millions of individual pixels making up the CSPAD all have the same slope of the response function. This slope represents the gain of each pixel, and they may be individually calibrated by extending eqn (2) with a pixel-to-pixel gain:

$$I_{\text{corrected}} = \left[I_{\text{measured}} - I_{\text{dark}} - \sum_i f_i(I) I_i^{\text{SVD}} - \sum_e f_e(E) I_e^{\text{SVD}}\right] \times \text{gain} \qquad (7)$$

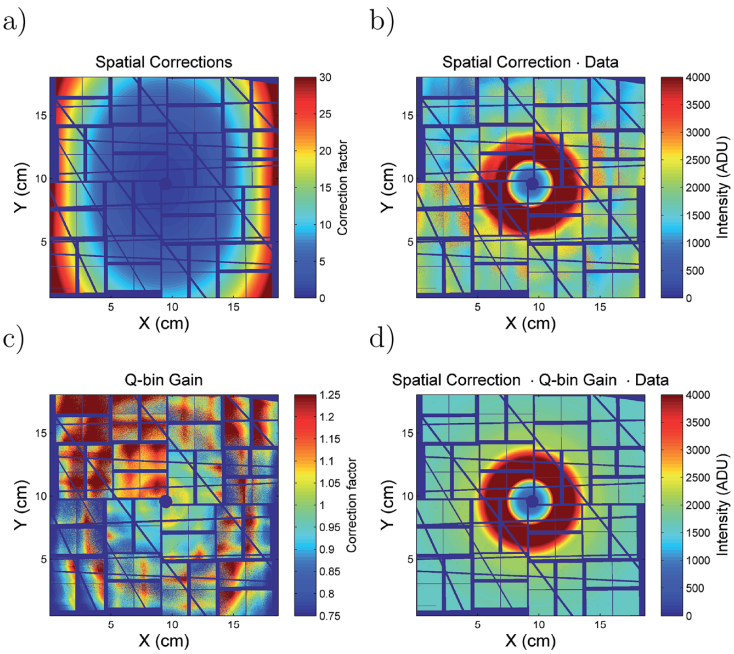

Fig. 15 (a) Calculated spatial corrections for polarisation, absorption through the liquid sheet and solid angle coverage. (b) The corrected data. (c) The Q correction resulting from enforcing azimuthal isotropy. (d) The resulting gain corrected isotropic scattering image.

In order to identify the gain for each pixel we suppose that the steady-state scattering is azimuthally isotropic after spatial corrections have been applied. Assuming this, each pixel value in a given Q-bin can be individually scaled to yield the mean of all the pixels in that Q-bin, and the scaling value determined in this way represents the pixel-resolved gain function for the detector. This will not change the 1D $\Delta S(Q)$-curves resulting from the azimuthal integration, but the 2D images will show smaller pixel-to-pixel variation and correct for spatial, tile dependent effects.

Fig. 15 shows the procedure for such a Q-bin gain correction. Panel (a) shows the spatial/geometry corrections applicable for this particular experimental setup and panel (b) shows the data after applying this correction. Panel (c) shows the resulting Q-bin gain correction following the assumption that the scattering signal is isotropic and panel (d) shows the pixel-resolved gain-function applied to the data. The Q-bin gain correction is robust and yields the correct gain for each pixel, if both the average gain correction of the detector and the geometry corrections are correct. As an alternative, for an absolute gain correction, the pixels in each Q-bin can instead be scaled to the signal from reference measurements of the studied sample.[28]

11. Discussion and outlook

In this paper, we have presented a method for robustly removing detector fluctuations that can be correlated with changes in beam parameters such as pulse intensities and X-ray energy. This approach is specifically applicable to XDS measurements at XFEL sources, where small differences are measured on a large background and where the beam properties can vary very significantly, both pulse-to-pulse and over time.

Since the method removes fluctuations described by their dependency on physical parameters, the approach can be implemented robustly without danger of over-filtering the data. The method can also be used to identify and quantify other fluctuations which may be present in the data, such as those relating to the detector electronics or changes in air scattering. The use of this method during an experiment can help identify unwanted fluctuations, and their sources *e.g.* stray scattering hitting the detector.

Previous approaches to filtering XFEL XDS data,[4] operating directly on 1D difference scattering curves, require a good model description of the expected difference signal. The methodology presented in this work requires no *a priori* knowledge of the expected difference signal and in contrast to the 1D-approach, the 2D-nature of the artefacts may be revealed and utilized to identify the underlying causes of such artefacts. For the data presented here, we find that the main contributors to signal fluctuations are changes in X-ray energy and intensity. A further strength of the presented approach is that correlation of fluctuations with additional parameters (*e.g.* X-ray beam position) can easily be tested for, making it a flexible tool for characterizing detectors.

Continued development of the CSPAD has significantly reduced many of the fluctuations described in this work. However, the energy dependent fluctuations are not a detector artefact but instead a result of the shot-to-shot energy variation of the XFEL pulses. The energy variation can be significantly reduced by using a monochromator[29] or self seeding scheme[30] at the cost of X-ray flux. In pink-beam

mode, the energy variation can be addressed by assigning new Q vectors to each pixel, based on the incident energy. Implementing this method of correcting for the energy variation, yields qualitatively similar results to the energy-dependent "artefact" subtraction.

The method presented in this paper was developed to address problems arising from the transition of XDS experiments from synchrotrons to XFELs, in particular detector problems associated with fast readout speeds and shot-to-shot variations of the XFEL pulses. Current construction of the European XFEL as well as the LCLS-II upgrade includes an additional increase in repetition rate by 2 orders of magnitude, and thus requires even faster detector readout speeds. These upcoming facilities are currently developing new detectors to meet these requirements. Such new detectors may present similar challenges as encountered with the synchrotron to XFEL transition and we believe the methodology presented here can provide valuable feedback on detector performance.

Acknowledgements

The authors acknowledge support from DANSCATT and wish to thank the detector group at SLAC National Accelerator Laboratory for discussions and feedback. Authors TBvD and MMN acknowledge support from the ReLiable project (Project no. 11-116792) funded by the Danish Council for Strategic Research Programme Commission on Sustainable Energy and Environment. Portions of this research were carried out at the Linac Coherent Light Source (LCLS) at the SLAC National Accelerator Laboratory. LCLS is an Office of Science User Facility operated for the U.S. Department of Energy Office of Science by Stanford University.

References

1 M. Harmand, R. Coffee, M. R. Bionta, M. Chollet, D. French, D. Zhu, D. M. Fritz, H. T. Lemke, N. Medvedev, B. Ziaja, S. Toleikis and M. Cammarata, *Nat. Photonics*, 2013, 7, 215–218.

2 H. N. Chapman, P. Fromme, A. Barty, T. a. White, R. a. Kirian, A. Aquila, M. S. Hunter, J. Schulz, D. P. DePonte, U. Weierstall, R. B. Doak, F. R. N. C. Maia, A. V. Martin, I. Schlichting, L. Lomb, N. Coppola, R. L. Shoeman, S. W. Epp, R. Hartmann, D. Rolles, A. Rudenko, L. Foucar, N. Kimmel, G. Weidenspointner, P. Holl, M. Liang, M. Barthelmess, C. Caleman, S. Boutet, M. J. Bogan, J. Krzywinski, C. Bostedt, S. Bajt, L. Gumprecht, B. Rudek, B. Erk, C. Schmidt, A. Hömke, C. Reich, D. Pietschner, L. Strüder, G. Hauser, H. Gorke, J. Ullrich, S. Herrmann, G. Schaller, F. Schopper, H. Soltau, K.-U. Kühnel, M. Messerschmidt, J. D. Bozek, S. P. Hau-Riege, M. Frank, C. Y. Hampton, R. G. Sierra, D. Starodub, G. J. Williams, J. Hajdu, N. Timneanu, M. M. Seibert, J. Andreasson, A. Rocker, O. Jönsson, M. Svenda, S. Stern, K. Nass, R. Andritschke, C.-D. Schröter, F. Krasniqi, M. Bott, K. E. Schmidt, X. Wang, I. Grotjohann, J. M. Holton, T. R. M. Barends, R. Neutze and S. Marchesini, *Nature*, 2011, **470**, 73–77.

3 S. Lee, W. Roseker, C. Gutt and B. Fischer, *Opt. Express*, 2013, **21**, 2037–2041.

4 K. Haldrup, *Philos. Trans. R. Soc., B*, 2014, **369**, 20130336.

5 S. Canton, K. S. Kjær, G. Vanko, T. van Driel, S.-i. Adachi, A. Bordage, C. Bressler, P. Chabera, M. Christensen, A. Dohn, A. Galler, W. Gawelda, D. Gosztola, K. Haldrup, T. Harlang, Y. Liu, K. Møller, Z. Nemeth, S. Nozawa, M. P`apai, T. Sato, K. Suarez-Alcantara, T. Togashi, K. Tono, J. Uhlig, D. Amarasinghe Vithanage, K. Wärnmark, M. Yabashi, J. Zhang, V. Sundström and M. Nielsen, *Nat. Commun.,* (accepted).

6 K. Haldrup, M. Christensen, M. Cammarata, Q. Y. Kong, M. Wulff, S. O. Mariager, K. Bechgaard, R. Feidenhans'l, N. Harrit and M. M. Nielsen, *Angew. Chem., Int. Ed.*, 2009, **48**, 4180–4184.

7 K. Haldrup, M. Christensen and M. M. Nielsen, *Acta Crystallogr., Sect. A: Found. Crystallogr.*, 2010, **66**, 261–269.

8 R. Alonso-Mori, J. Kern, D. Sokaras, T.-C. Weng, D. Nordlund, R. Tran, P. Montanez, J. Delor, V. K. Yachandra, J. Yano and U. Bergmann, *Rev. Sci. Instrum.*, 2012, **83**, 073114.

9 R. Alonso-Mori, J. Kern, R. J. Gildea, D. Sokaras, T.-C. Weng, B. Lassalle-Kaiser, R. Tran, J. Hattne, H. Laksmono, J. Hellmich, C. Glöckner, N. Echols, R. G. Sierra, D. W. Schafer, J. Sellberg, C. Kenney, R. Herbst, J. Pines, P. Hart, S. Herrmann, R. W. Grosse-Kunstleve, M. J. Latimer, A. R. Fry, M. M. Messerschmidt, A. Miahnahri, M. M. Seibert, P. H. Zwart, W. E. White, P. D. Adams, M. J. Bogan, S. Boutet, G. J. Williams, A. Zouni, J. Messinger, P. Glatzel, N. K. Sauter, V. K. Yachandra, J. Yano and U. Bergmann, *Proc. Natl. Acad. Sci. U. S. A.*, 2012, **109**, 19103–19107.

10 S. Herrmann, S. Boutet, B. Duda, D. Fritz, G. Haller, P. Hart, R. Herbst, C. Kenney, H. Lemke, M. Messerschmidt, J. Pines, A. Robert, M. Sikorski and G. Williams, *Nucl. Instrum. Methods Phys. Res., Sect. A*, 2013, **718**, 550–553.

11 W. Zhang, R. Alonso-Mori, U. Bergmann, C. Bressler, M. Chollet, A. Galler, W. Gawelda, R. G. Hadt, R. W. Hartsock, T. Kroll, K. S. Kjær, K. Kubiček, H. T. Lemke, H. W. Liang, D. a. Meyer, M. M. Nielsen, C. Purser, J. S. Robinson, E. I. Solomon, Z. Sun, D. Sokaras, T. B. van Driel, G. Vankó, T.-C. Weng, D. Zhu and K. J. Gaffney, *Nature*, 2014, **509**, 345–348.

12 D. Arnlund, L. C. Johansson, C. Wickstrand, A. Barty, G. J. Williams, E. Malmerberg, J. Davidsson, D. Milathianaki, D. P. DePonte, R. L. Shoeman, D. Wang, D. James, G. Katona, S. Westenhoff, T. a. White, A. Aquila, S. Bari, P. Berntsen, M. Bogan, T. B. van Driel, R. B. Doak, K. S. Kjær, M. Frank, R. Fromme, I. Grotjohann, R. Henning, M. S. Hunter, R. a. Kirian, I. Kosheleva, C. Kupitz, M. Liang, A. V. Martin, M. M. Nielsen, M. Messerschmidt, M. M. Seibert, J. Sjöhamn, F. Stellato, U. Weierstall, N. a. Zatsepin, J. C. H. Spence, P. Fromme, I. Schlichting, S. Boutet, G. Groenhof, H. N. Chapman and R. Neutze, *Nat. Methods*, 2014, **11**, 923–926.

13 H. T. Philipp, M. W. Tate and S. M. Gruner, *J. Instrum.*, 2011, **6**, C11006.

14 S. Boutet and G. J. Williams, *New J. Phys.*, 2010, **12**, 035024.

15 P. R. Ribic and G. Margaritondo, *J. Phys. D: Appl. Phys.*, 2012, **45**, 213001.

16 H. T. Lemke, C. Bressler, L. X. Chen, D. M. Fritz, K. J. Gaffney, A. Galler, W. Gawelda, K. Haldrup, R. W. Hartsock, H. Ihee, J. Kim, K. H. Kim, J. H. Lee, M. M. Nielsen, A. B. Stickrath, W. Zhang, D. Zhu and M. Cammarata, *J. Phys. Chem. A*, 2013, **117**, 735–740.

17 G. E. Box, G. M. Jenkins and G. C. Reinsel, *Time series analysis: Forecasting and control*, Wiley, 2008, p. 746 s.

18 D. Zhu, M. Cammarata, J. Feldkamp, D. M. Fritz, J. Hastings, S. Lee, H. T. Lemke, A. Robert, J. Turner and Y. Feng, *J. Phys.: Conf. Ser.*, 2013, **425**, 052033.
19 M. R. Bionta, H. T. Lemke, J. P. Cryan, J. M. Glownia, C. Bostedt, M. Cammarata, J.-C. Castagna, Y. Ding, D. M. Fritz, a. R. Fry, J. Krzywinski, M. Messerschmidt, S. Schorb, M. L. Swiggers and R. N. Coffee, *Opt. Express*, 2011, **19**, 21855–21865.
20 H. T. Lemke, M. Weaver, M. Chollet, J. Robinson, J. M. Glownia, D. Zhu, M. R. Bionta, M. Cammarata, M. Harmand, R. N. Coffee and D. M. Fritz, *Proc. SPIE*, 2013, **8778**, 87780S.
21 W. Press, B. Flannery, S. Teukolsky and W. Vetterling, *Numerical Recipes - The Art of Scientific Computing.*, Cambridge University Press, 1986.
22 R. W. Hendler and R. I. Shrager, *J. Biochem. Biophys. Methods*, 1994, **28**, 1–33.
23 M. Brand, *Linear Algebra Appl.*, 2006, **415**, 20–30.
24 D. Wingate, http://www.mit.edu/wingated/resources.html, 2007.
25 U. Lorenz, K. B. Mller and N. E. Henriksen, *New J. Phys.*, 2010, **12**, 113022.
26 M. Christensen, K. Haldrup, K. Bechgaard, R. Feidenhans'l, Q. Y. Kong, M. Cammarata, M. Lo Russo, M. Wulff, N. Harrit and M. M. Nielsen, *J. Am. Chem. Soc.*, 2009, **131**, 502–508.
27 K. Haldrup, T. Harlang, M. Christensen, A. Dohn, T. B. van Driel, K. S. Kjær, N. Harrit, J. Vibenholt, L. Guerin, M. Wulff and M. M. Nielsen, *Inorg. Chem.*, 2011, **50**, 9329–9336.
28 K. Haldrup, *et al.*, in preparation.
29 D. Zhu, Y. Feng, S. Stoupin, S. a. Terentyev, H. T. Lemke, D. M. Fritz, M. Chollet, J. M. Glownia, R. Alonso-Mori, M. Sikorski, S. Song, T. B. van Driel, G. J. Williams, M. Messerschmidt, S. Boutet, V. D. Blank, Y. V. Shvyd'ko and A. Robert, *Rev. Sci. Instrum.*, 2014, **85**, 063106.
30 J. Amann, W. Berg, V. Blank, F. J. Decker, Y. Ding, P. Emma, Y. Feng, J. Frisch, D. Fritz, J. Hastings, Z. Huang, J. Krzywinski, R. Lindberg, H. Loos, A. Lutman, H. D. Nuhn, D. Ratner, J. Rzepiela, D. Shu, Y. Shvyd'ko, S. Spampinati, S. Stoupin, S. Terentyev, E. Trakhtenberg, D. Walz, J. Welch, J. Wu, A. Zholents and D. Zhu, *Nat. Photonics*, 2012, **6**, 693–698.

Paper III

PRL 117, 013002 (2016) PHYSICAL REVIEW LETTERS week ending 1 JULY 2016

Femtosecond X-Ray Scattering Study of Ultrafast Photoinduced Structural Dynamics in Solvated $[Co(terpy)_2]^{2+}$

Elisa Biasin,[1] Tim Brandt van Driel,[1] Kasper S. Kjær,[1,2,3] Asmus O. Dohn,[4] Morten Christensen,[1] Tobias Harlang,[2] Pavel Chabera,[2] Yizhu Liu,[2,5] Jens Uhlig,[2] Mátyás Pápai,[4,6] Zoltán Németh,[6] Robert Hartsock,[3] Winnie Liang,[3] Jianxin Zhang,[7] Roberto Alonso-Mori,[8] Matthieu Chollet,[8] James M. Glownia,[8] Silke Nelson,[8] Dimosthenis Sokaras,[8] Tadesse A. Assefa,[9] Alexander Britz,[9] Andreas Galler,[9] Wojciech Gawelda,[9,10] Christian Bressler,[9] Kelly J. Gaffney,[3] Henrik T. Lemke,[8,11] Klaus B. Møller,[4] Martin M. Nielsen,[1] Villy Sundström,[2] György Vankó,[6] Kenneth Wärnmark,[5] Sophie E. Canton,[12,13] and Kristoffer Haldrup[1,*]

[1]*Department of Physics, Technical University of Denmark, Fysikvej 307, DK-2800 Kongens Lyngby, Denmark*
[2]*Department of Chemical Physics, Lund University, Box 118, S-22100 Lund, Sweden*
[3]*PULSE Institute, SLAC National Accelerator Laboratory, Menlo Park, California 94025, USA*
[4]*Department of Chemistry, Technical University of Denmark, Kemitorvet 207, DK-2800 Kongens Lyngby, Denmark*
[5]*Centre for Analysis and Synthesis, Department of Chemistry, Lund University, Box 124, Lund SE-22100, Sweden*
[6]*Wigner Research Centre for Physics, Hungarian Academy Sciences, H-1525 Budapest, Hungary*
[7]*School of Environmental and Chemical Engineering, Tianjin Polytechnic University, Tianjin 300387, China*
[8]*LCLS, SLAC National Accelerator Laboratory, Menlo Park, California 94025, USA*
[9]*European XFEL GmbH, Albert-Einstein-Ring 19, D-22761 Hamburg, Germany*
[10]*Institute of Physics, Jan Kochanowski University, 25-406 Kielce, Poland*
[11]*SwissFEL, Paul Scherrer Institut, 5232 Villigen PSI, Switzerland*
[12]*IFG Structural Dynamics of (Bio)chemical Systems, Max Planck Institute for Biophysical Chemistry, Am Fassberg 11, D-37077 Goettingen, Germany*
[13]*FS-SCS, Structural Dynamics with Ultra-short Pulsed X-rays, Deutsches Elektronen-Synchrotron (DESY), Notkestrasse 85, D-22607 Hamburg, Germany*

(Received 5 February 2016; published 30 June 2016)

We study the structural dynamics of photoexcited $[Co(terpy)_2]^{2+}$ in an aqueous solution with ultrafast x-ray diffuse scattering experiments conducted at the Linac Coherent Light Source. Through direct comparisons with density functional theory calculations, our analysis shows that the photoexcitation event leads to elongation of the Co-N bonds, followed by coherent Co-N bond length oscillations arising from the impulsive excitation of a vibrational mode dominated by the symmetrical stretch of all six Co-N bonds. This mode has a period of 0.33 ps and decays on a subpicosecond time scale. We find that the equilibrium bond-elongated structure of the high spin state is established on a single-picosecond time scale and that this state has a lifetime of ~7 ps.

DOI: 10.1103/PhysRevLett.117.013002

Several Co(II) compounds are known to transition between their low spin (LS) and high spin (HS) electronic states [1–3]. Such transitions can be induced by temperature increase, excitation by light, or high magnetic fields [4], and they are accompanied by distinct changes in magnetic and structural properties that may be exploited in the design of display and memory devices [5,6] and in single-molecule spintronic applications [7]. The realization of exploitable spin-state transitions (SSTs) in Co(II) compounds is more challenging than in the corresponding Fe(II) complexes, which have been investigated in great detail during the last decades [8–15]. These challenges stem from the partial occupation of the antibonding e_g^* orbitals in the ground state, which leads to smaller structural changes arising from the SST phenomenon; the corresponding smaller energy barriers between the potential surfaces of the HS and LS Co(II) states result in faster dynamics [1], as well as a high sensitivity to the crystalline environment or to the solvent properties [2]. The key structural parameters for the SSTs are the Co-N bond lengths [8], but the time scales and the dynamics of the LS-HS transitions have remained unclear for Co compounds. Time-resolved x-ray scattering can be used to monitor such structural changes and dynamics if the time resolution of the experiment is sufficiently high. X-ray free electron lasers (XFELs) provide ultrashort (~30 fs) x-ray pulses and high flux allowing the nuclear dynamics following photoexcitation to be recorded at the required femtosecond time scales [16,17]. Here, we report, for the first time, direct measurements of the excited-state structure and the ultrafast structural dynamics of a solvated Co(II) complex upon a photoinduced SST.

Figure 1 shows the molecular structure of $[Co(terpy)_2]^{2+}$ (terpy $= 2,2':6',2''-$terpyridine). In this six-coordinated complex, the d^7 Co center can be either a LS doublet state or a HS quartet state [2,18]. In solid-state samples, the relative populations of both spin states depend strongly on the

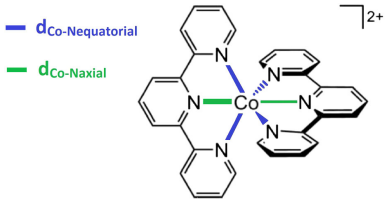

FIG. 1. Schematic representation of the structure of $[Co(terpy)_2]^{2+}$. The LS → HS transition can be induced by photoexcitation with a 530 nm laser pulse and is characterized by an anisotropic expansion of the metal-ligand bonds. Axial and equatorial Co-N bonds are highlighted in different colors.

temperature and on the crystalline environment [19–21]. In crystallographic studies the compound was observed to be compressed in the LS state (short axial and long equatorial Co-N bonds), due mostly to the geometrical constraints of the coordinating tridentate ligands, and may also exhibit asymmetry, with one ligand being closer to the Co center than the other due to a pseudo–Jahn-Teller effect [20,22]. Upon LS → HS transition in solid-state samples, the axial bond length has been observed to increase by up to 0.21 Å and the equatorial by 0.07 Å, depending on the anion and the degree of hybridization [23]. As reported by Vargas *et al.* [22], density functional theory (DFT) calculations in the gas phase also predict an anisotropic increase of the Co-N bonds upon the LS → HS spin change (an increase of 0.16 and 0.05 Å for the axial and equatorial bonds, respectively). A few studies on the properties of $[Co(terpy)_2]^{2+}$ in solution also exist [2,3,18,24]. Kremer *et al.* [18] report that solvated $[Co(terpy)_2]^{2+}$ is predominantly LS at room temperature, and Enachescu *et al.* demonstrated that photoexcitation in the visible range populates the metal to ligand charge transfer (MLCT) state from which the HS state is populated [3]. Very little information is available regarding the excited-state decay pathways and the HS → LS relaxation time is currently only known to be less than 2 ns [24].

In this work, we utilized x-ray diffuse scattering (XDS) laser pump–x-ray probe experiments to study the formation, structure, and decay of the HS state of aqueous $[Co(terpy)_2]^{2+}$. The measurements were conducted at the x-ray pump-probe (XPP) instrument at the Linac Coherent Light Source (LCLS) XFEL facility [17]. A 20 mM aqueous solution of $[Co(terpy)_2]^{2+}$ was pumped trough a nozzle producing a 100 μm liquid sheet flowing in the vertical direction at a flow rate sufficient to fully replace the sample between successive pump-probe events. The photocycle was initiated by 70 μJ laser pulses at 530 nm and with a 70 fs pulse width (FWHM) focused onto a spot of 150 μm (FWHM). The 8.3 keV x-ray probe pulses overlapped with the pump laser at the sample position. The time delay t between the laser and the x-ray pulses was determined for every pump-probe event with ∼10 fs (FWHM) resolution using the XPP timing tool [25]. The scattered x-rays were detected by a Cornell-SLAC pixel array detector [26] 70 mm after the sample, covering scattering vectors Q up to 3.5 $Å^{-1}$.

Following detector corrections [27], the scattering signal was scaled to the liquid unit cell reflecting the stoichiometry of the sample [28], yielding the acquired signal in electron units per solute molecule (e.u./molec). Individual 2D difference scattering patterns were obtained by subtracting images where the pump laser was dropped before the sample from those where the pump laser had interacted

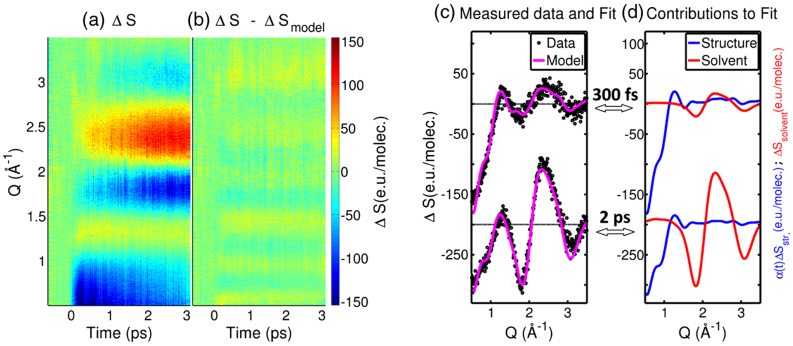

FIG. 2. (a) Measured difference scattering signal (ΔS) of photoexcited $[Co(terpy)_2]^{2+}$ in water. (b) Residuals obtained by subtracting the model (ΔS_{model}) from the experimental data. (c),(d) Fit of the 1D difference scattering curves at 300 fs and 2 ps. (c) The modeled difference signal (the magenta line) overlaid over the experimental data (the black points). (d) The contributions to the model from the structural changes (solute and cage, the blue line) and from the bulk solvent (the red line).

with the sample. The patterns were then time sorted and averaged in ~23 fs wide bins. Finally, 1D isotropic and anisotropic difference scattering signals were extracted [29]. Figure 2(a) shows the measured isotropic difference signals $\Delta S(Q,t)$ in a 2D representation.

$\Delta S(Q,t)$ can be considered as arising from three contributions [30]: the structural changes in the solute molecules (ΔS_{solute}), the local changes in geometry and rearrangements of the solvent molecules in close proximity to the solute (ΔS_{cage}), and the temperature and density changes in the bulk solvent following energy deposition ($\Delta S_{\text{solvent}}$).

$\Delta S_{\text{solute}}(Q)$ can be directly calculated from putative structural models of the molecule through the Debye equation [Eq. (S2) in the Supplemental Material (SM) [31]]. As a starting point for the present analysis, the difference scattering signal expected upon the photoexcitation was calculated from the LS and HS DFT-optimized geometries of $[\text{Co(terpy)}_2]^{2+}$:

$$\Delta S_{\text{solute}}(Q) = S_{\text{HS}}(Q) - S_{\text{LS}}(Q). \quad (1)$$

The DFT calculations were carried out as detailed in the SM [31], and Table I reports the key DFT-calculated structural parameters. Upon the LS → HS transition, the Co-N bonds expand ~0.16 and ~0.08 Å along the axial and the equatorial directions, respectively, in good agreement with the earlier study by Vargas *et al.* [22]. The ratio between the axial and the equatorial Co-N disatnce is defined as η. In the LS state the average η is 0.91 (0.88 and 0.92 for the two ligands, with the difference due to the Jahn-Teller effect), while in the HS state η increases to 0.95 (for both ligands).

The cage contribution $\Delta S_{\text{cage}}(Q)$ to the simulated signal was calculated from the radial distribution functions of the solute-solvent atom pairs [43] determined through classical molecular dynamics (MD) simulations [31]. The contribution from changes in the solute structure and the solvation cage are related 1:1 and can therefore be combined under the term "structure", $\Delta S_{\text{str.}}(Q)$, such that

$$\Delta S_{\text{str.}}(Q) = \Delta S_{\text{solute}}(Q) + \Delta S_{\text{cage}}(Q). \quad (2)$$

Finally, the bulk-solvent term $\Delta S_{\text{solvent}}(Q)$ has been shown to be very well described by a linear combination of solvent difference signals, $(\partial S(Q)/\partial T)|_\rho$ and $(\partial S(Q)/\partial \rho)|_T$, which can be measured in separate experiments [44,45]:

$$\Delta S(Q,t)_{\text{solvent}} = \Delta T(t)\left.\frac{\partial S(Q)}{\partial T}\right|_\rho + \Delta\rho(t)\left.\frac{\partial S(Q)}{\partial \rho}\right|_T, \quad (3)$$

where ΔT and $\Delta\rho$ are the changes in temperature and density, respectively. Such solvent differentials for XDS experiments are archived for a range of solvents [45,46] and are used in the present work. In contrast to earlier experiments on Fe SST compounds [30], we observe no density change above our detection limit of 0.05 kg/m^3 [Fig. S1(b) of the SM [31]], and this term was thus excluded from the analysis.

From visual inspection of the measured difference signal in Fig. 2(a), we qualitatively observe a very fast rise of a negative feature at low Q ($Q < 1$ Å^{-1}) which gradually decays over the course of several picoseconds. Such a low-Q feature is characteristic of an increase in the solute size. On the few picosecond time scale, a distinct signal around $Q = 2$ Å^{-1} grows in. This feature is identified as the characteristic difference signal arising from a temperature increase of the aqueous solvent. In the low-Q region, oscillatory features as a function of time can be observed and indicate structural dynamics along the main coordinate of the structural changes; in the present case, the Co-N bond lengths ($d_{\text{Co-N}}$). The latter is therefore introduced as a time-dependent parameter in Eq. (1):

$$S_{\text{HS}}(Q,t) = S_{\text{HS}}(Q, d_{\text{Co-N}}(t)). \quad (4)$$

Specifically, $d_{\text{Co-Naxial}}$ of the HS structure was allowed to vary ±0.1 Å from the value reported in Table I, while the ratio η, through which $d_{\text{Co-Nequatorial}}$ can be calculated and included in the structural modeling, was kept fixed to 0.95 in the analysis. Thus, all six Co-N bond length changes are parametrized through the single structural parameter $d_{\text{Co-Naxial}}$.

Based on the considerations outlined above, the full model applied to fit and interpret the measured difference signal is thus:

$$\Delta S_{\text{model}}(Q,t) = \alpha(t)\Delta S_{\text{str.}}(Q,t) + \Delta T(t)\left.\frac{\partial S(Q)}{\partial T}\right|_\rho, \quad (5)$$

where $\alpha(t)$ describes the time-dependent excitation fraction of the solute, which, in the context of the present analysis, is assumed to be described by an exponential decay starting at t_0, i.e., the arrival time of the laser pump. The time resolution of the experiment is included by convolution with the (Gaussian) instrument response function (IRF) to yield the following expression for $\alpha(t)$:

$$\alpha(t) = \text{IRF}(\sigma_{\text{IRF}}, t) \otimes H(t - t_0)Ae^{-(t-t_0/\tau)}, \quad (6)$$

TABLE I. Structural parameters of the DFT-calculated LS and HS structures of $[\text{Co(terpy)}_2]^{2+}$ obtained in the present study. $d_{\text{Co-Naxial}}$ and $d_{\text{Co-Nequatorial}}$ are averages over the two axial and the four equatorial metal-ligand bond distances, respectively, and $\eta = (d_{\text{Co-Naxial}}/d_{\text{Co-Nequatorial}})$. The change of each parameter upon the LS → HS spin transition is also reported and compared with the values obtained from the measured data.

	LS	HS		DFT	Measured
$d_{\text{Co-Naxial}}$ (Å)	1.902	2.058	$\Delta d_{\text{Co-Naxial}}$ (Å)	0.16	0.13
$d_{\text{Co-Nequatorial}}$ (Å)	2.08	2.16	$\Delta d_{\text{Co-Nequatorial}}$ (Å)	0.08	0.06
η	0.91	0.95			

where σ_{IRF} is the width of the IRF; A and τ are the amplitude and the lifetime of the exponential function representing, respectively, the initial excitation fraction and the lifetime of the bond-elongated excited state; and H is the Heaviside step function centered at t_0 [as detailed in Eq. (S3) of the SM [31]]. We note that assuming the excited-state population to be given by the integral of a Gaussian envelope of the excitation pulse is an approximation—especially given the high intensity of the optical excitation, as discussed in further detail below. σ_{IRF} and t_0 were determined from the transient solvent contribution to the anisotropic part of the difference scattering signal (Fig. S4 of the SM [31]), from which we find $\sigma_{IRF} = 0.05$ ps ± 0.03 ps. Furthermore, we estimated the lifetime of the HS state from a single set of measurements out to 20 ps. The analysis of this data set is presented in the SM and yields $\tau = 6.8$ ps ± 0.8 ps [Fig. S8(a) of the SM [31]], allowing us to constrain this parameter in Eq. (6).

From these considerations, the number of free parameters in the model described by Eq. (5) is reduced to three: A, $d_{Co\text{-}Naxial}$, and ΔT. The model was fitted to the acquired difference signal $\Delta S(Q)$ for all time delays simultaneously within a standard χ^2 [Eq. (S6) of the SM [31]] minimization framework [47]. Good fits were observed for all time delays, and Fig. 2(b) shows the residuals after subtracting the model from the measured data. Figures 2(c) and 2(d) show examples of the fitting results at two time delays, 300 fs and 2 ps.

From the kinetics part of the fit of our model to the acquired data, the initial excitation fraction A was found to be $34\% \pm 2\%$. Regarding the difference signal arising from solvent heating: the analysis of $\Delta T(t)$ is discussed in detail in the SM [Figs. S3 and S8(b) [31]], but, stated briefly, it is found to be well described by a broadened double exponential dominated ($> 90\%$) by a response with a grow-in time constant of 4.0 ps $\pm$ 0.6 ps. A total solvent temperature increase of $\Delta T = 0.8$ K is found, which is 0.4 K more than the amount of energy expected to be released through nonradiative decay processes after single-photon excitation of the solute. As detailed in the SM [31], this extra heat can be ascribed to multiphoton absorption due to the relatively high excitation laser intensity and short pulse length. A direct comparison with data taken at 3 times lower laser power (Fig. S10 of the SM [31]) shows that the multiphoton absorption has no discernible impact on the structural response of the solute molecules.

Turning to the key results of this Letter, Fig. 3 shows the best-fit result for the changes in $d_{Co\text{-}Naxial}$ from the ground to the excited state as a function of time (the black data points). Following excitation, the axial Co-N bond increases by $\Delta d_{Co\text{-}Naxial} = 0.14$ Å and exhibits oscillations. On the 1 ps time scale, the axial Co-N bond length of the excited-state ensemble decreases by $\sim$0.01 Å and then remains constant over the $\sim$7 ps lifetime of the HS state. Thus, $d_{Co\text{-}Naxial}$ and $d_{Co\text{-}Nequatorial}$ are found to be, respectively, 0.13 and 0.06 Å longer in the HS state than in the LS state, distance changes which are slightly smaller than the DFT predictions (Table I). The rise time of the solvent heating signal indicates that full thermal equilibration with the surrounding solvent takes place in about 4 ps.

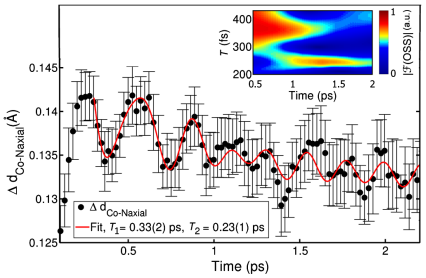

FIG. 3. Time evolution of the Co-N bond lengths (black dots) upon photoexcitation, smoothed with 4-point ($\sim$100 fs) moving average filter. The insert shows a time-resolved Fourier transform of the oscillatory part of the difference scattering signal (Fig. 2(a) and Fig. S6 [31]), indicating sequential activation of two vibrational modes. The red line shows a heuristic fit, incorporating sequential activation of first a $T_1 \sim 0.33$ ps mode and then a $T_2 \sim 0.23$ ps mode identified as, respectively, breathing- and pincerlike by direct comparison with our DFT calculations.

The inset of Fig. 3 shows a time-dependent Fourier transform ($\mathcal{F}$) of the oscillatory structural signal contained in ΔS and calculated as detailed in the SM [31]. From this, we observe two distinct components: one mode which appears within the time resolution of our experiment and decays on a $\sim$1 ps time scale, and one mode which grows in after 1 ps. The red line in Fig. 3 illustrates the fit of a heuristic model to the data after the initial lengthening of the Co-N axial bond. The model is comprised of two sinusoidals [Eq. (S4) of the SM [31]], the first one being damped and driving the second. Both sinusoidals are broadened by the IRF and superimposed on an exponentially decaying background with a time constant of 0.7 ps $\pm$ 0.1 ps. From this fit, we find that the period T_1 of the main oscillation is 0.33 ps $\pm$ 0.03 ps and that the damping time is 0.4 ps $\pm$ 0.1 ps. On the same time scale, we observe the growing of the second oscillation with a period of $T_2 = 0.23$ ps $\pm$ 0.01 ps. In the framework of this analysis and by direct comparison with the DFT-calculated vibrational modes of the HS state, we assign the first component to a breathinglike mode (movie S1 of the SM [31]) with synchronous stretching of all six Co-N bonds, whereas the second, weaker component is assigned to arise from a pincerlike movement of the tridentate ligands (movie S2 of the SM [31]). The assignment of these modes is in good agreement with the recent work on related Fe(II) complexes [10,48,49], where the immediately excited stretching modes were quickly damped as energy

was dissipated into other degrees of freedom. Future experiments utilizing higher x-ray energies to access a larger region of momentum space should facilitate detailed studies of the structural degrees of freedom [as recently demonstrated for $[Fe(terpy)_2]^{2+}$ on synchrotron time scales (100 ps) [12,50,51]] involved in the structural relaxation of the electronically excited state. Such studies may be fruitfully combined with *ab initio* MD [52], thus going beyond the classical-mechanics description of the combined DFT-MD simulations used in the present analysis.

Returning to the solute dynamics, by assuming that the excited-state potential is well approximated by a harmonic potential and if the population of this state is nearly instantaneous, one would expect the ensemble mean of the Co-N bond length to reach its maximum value one half period (~0.17 ps) after excitation. From Fig. 3, we find this point to be reached only after 0.25 ps. By singular value decomposition of the structural contribution to ΔS (Figs. S4 and S5 of the SM [31]), we find this observation of a delayed structural transition to be model independent and further find that the delayed onset is well described by an exponential grow-in ($\tau = 0.06$ ps $\pm$ 0.01 ps) of the signal with a 0.08 ps $\pm$ 0.02 ps phase shift of the oscillations. These observations are consistent with the excited-state structural dynamics taking place on several potential surfaces: photoexcitation produces a MLCT excited state, while bond elongation is believed to occur predominantly in the metal-centered HS excited state. Referring back to the discussion of Eq. (6), we note that this expression is only strictly applicable in a regime of linear response and that, therefore, the ~100 fs delay in bond elongation can be considered only a coarse, structural measure of the time scale involved in the electronic processes of intersystem crossing and internal conversion that eventually leads to formation of the HS state. This delay, while sufficiently fast to launch the observed synchronous Co-N stretch mode, leads to a significant broadening of the HS population in terms of the Co-N bond lengths. This in turn leads to the observed phase shift and the comparatively low amplitude of the observed oscillations.

These results demonstrate how time-resolved x-ray scattering with solution-state samples can be utilized to accurately characterize femtosecond structural dynamics as photoexcited molecules traverse the potential energy landscape of the excited state(s). We believe the results and methodology presented here to be broadly applicable, and we envision that these types of experiments will have a significant impact on our understanding of the fundamental mechanisms at work in SST systems and in both natural and artificial photosensitizers, where the redistribution of energy to different and strongly coupled internal degrees of freedom (both electronic and structural) are of key importance.

The DTU-affiliated authors would like to gratefully acknowledge DANSCATT for funding the beam time efforts. M. M. N., K. B. M., K. H., A. D., E. B., K. S. K., and T. B. V. D. acknowledge support from Det Frie Forskningsråd (DFF), and the Lundbeck Foundation. S. E. C acknowledges funding from SFB 1073. This project was also supported by the European Research Council via Contract No. ERC-StG-259709, the Hungarian Scientific Research Fund (OTKA) under Contract No. K29724 and the Lendület (Momentum) Program of the Hungarian Academy of Sciences (LP2013-59). Z. N. acknowledges support from the Bolyai Fellowship of the Hungarian Academy of Sciences. M. P. acknowledges support from the People Programme (Marie Curie Actions) of the European Union's Seventh Framework Programme (FP7 2007–2013) under REA Grant Agreement No. 609405 (COFUNDPostdocDTU). J. U. gratefully acknowledges the continued funding from the Knut and Alice Wallenberg Foundation. J. Z. greatly acknowledges support from NSFC (21302138) and the Tianjin High School Science and Technology Fund Planning Project (20130504). R. W. H., H. W. L., and K. J. G. acknowledge support from the AMOS program within the Chemical Science, Geosciences and Biosciences Division of the Office of Basic Energy Sciences, Office of Science, U.S. Department of Energy. T. A., A. B., W. G., A. G., and C. B. acknowledge funding from the German Science Foundation (DFG) via SFB925 and from the Centre of Ultrafast Imaging (CUI). Use of the Linac Coherent Light Source (LCLS), SLAC National Accelerator Laboratory, is supported by the U.S. Department of Energy, Office of Science, Office of Basic Energy Sciences under Contract No. DE-AC02-76SF00515.

*Corresponding author.
hald@fysik.dtu.dk

[1] H. A. Goodwin, Top. Curr. Chem. **234**, 23 (2004).
[2] I. Krivokapic, M. Zerara, M. L. Daku, A. Vargas, C. Enachescu, C. Ambrus, P. Tregenna-Piggott, N. Amstutz, E. Krausz, and A. Hauser, Coord. Chem. Rev. **251**, 364 (2007).
[3] C. Enachescu, I. Krivokapic, M. Zerara, J. A. Real, N. Amstutz, and A. Hauser, Inorg. Chim. Acta **360**, 3945 (2007).
[4] A. Bousseksou, K. Boukheddaden, M. Goiran, C. Consejo, M.-L. Boillot, and J.-P. Tuchagues, Phys. Rev. B **65**, 172412 (2002).
[5] O. Kahn and C. J. Martinez, Science **279**, 44 (1998).
[6] G. Molnár, L. Salmon, W. Nicolazzi, F. Terki, and A. Bousseksou, J. Mater. Chem. C **2**, 1360 (2014).
[7] E. Ruiz, Phys. Chem. Chem. Phys. **16**, 14 (2014).
[8] P. Gütlich and H. A. Goodwin, Top. Curr. Chem. **233**, 1 (2004).
[9] M. Chergui, in *Spin-Crossover Materials*, edited by M. A. Halcrow (John Wiley & Sons, New York, 2013), p. 405.
[10] M. Cammarata, R. Bertoni, M. Lorenc, H. Cailleau, S. Di Matteo, C. Mauriac, S. F. Matar, H. Lemke, M. Chollet, S. Ravy *et al.*, Phys. Rev. Lett. **113**, 227402 (2014).
[11] G. Vankó, T. Neisius, G. Molnár, F. Renz, S. Kárpáti, A. Shukla, and F. M. F. de Groot, J. Phys. Chem. B **110**, 11647 (2006).

[12] S. E. Canton, X. Zhang, L. M. Lawson Daku, A. L. Smeigh, J. Zhang, Y. Liu, C.-J. Wallentin, K. Attenkofer, G. Jennings, C. A. Kurtz *et al.*, J. Phys. Chem. C **118**, 4536 (2014).

[13] J. Nance, D. N. Bowman, S. Mukherjee, C. T. Kelley, and E. Jakubikova, Inorg. Chem. **54**, 11259 (2015).

[14] K. Haldrup *et al.*, J. Phys. Chem. B **120**, 1158 (2016).

[15] H. Lemke *et al.*, arXiv:1511.01294.

[16] H. T. Lemke, C. Bressler, L. X. Chen, D. M. Fritz, K. J. Gaffney, A. Galler, W. Gawelda, K. Haldrup, R. W. Hartsock, H. Ihee, J. Kim, K. H. Kim, J. H. Lee, M. M. Nielsen, A. B. Stickrath, W. Zhang, D. Zhu, and M. Cammarata, J. Phys. Chem. A **117**, 735 (2013).

[17] M. Chollet, R. Alonso-Mori, M. Cammarata, D. Damiani, J. Defever, J. T. Delor, Y. Feng, J. M. Glownia, J. B. Langton, S. Nelson, K. Ramsey, A. Robert, M. Sikorski, S. Song, D. Stefanescu, V. Srinivasan, D. Zhu, H. T. Lemke, and D. M. Fritz, J. Synchrotron Radiat. **22**, 503 (2015).

[18] S. Kremer, W. Henke, and D. Reinen, Inorg. Chem. **21**, 3013 (1982).

[19] J. S. Judge and W. Baker, Jr., Inorg. Chim. Acta **1**, 68 (1967).

[20] S. Hayami, Y. Komatsu, T. Shimizu, H. Kamihata, and Y. H. Lee, Coord. Chem. Rev. **255**, 1981 (2011).

[21] H. Oshio, H. Spiering, V. Ksenofontov, F. Renz, and P. Gütlich, Inorg. Chem. **40**, 1143 (2001).

[22] A. Vargas, I. Krivokapic, A. Hauser, and L. M. Lawson Daku, Phys. Chem. Chem. Phys. **15**, 3752 (2013).

[23] B. N. Figgis, E. S. Kucharski, and A. H. White, Australian Journal of Chemistry **36**, 1537 (1983).

[24] J. K. Beattie, R. A. Binstead, M. T. Kelso, P. Del Favero, T. G. Dewey, and D. H. Turner, Inorg. Chim. Acta **235**, 245 (1995).

[25] M. P. Minitti, J. S. Robinson, R. N. Coffee, S. Edstrom, S. Gilevich, J. M. Glownia, E. Granados, P. Hering, M. C. Hoffmann, A. Miahnahri *et al.*, J. Synchrotron Radiat. **22**, 526 (2015).

[26] H. T. Philipp, M. Hromalik, M. Tate, L. Koerner, and S. M. Gruner, Nucl. Instrum. Methods Phys. Res., Sect. A **649**, 67 (2011).

[27] T. B. van Driel, K. S. Kjaer, E. Biasin, K. Haldrup, H. T. Lemke, and M. M. Nielsen, Faraday Discuss. **177**, 443 (2015).

[28] K. Haldrup, M. Christensen, and M. Meedom Nielsen, Acta Crystallogr. Sect. A **66**, 261 (2010).

[29] U. Lorenz, K. B. Møller, and N. E. Henriksen, New J. Phys. **12**, 113022 (2010).

[30] K. Haldrup, G. Vankó, W. Gawelda, A. Galler, G. Doumy, A. M. March, E. P. Kanter, A. Bordage, A. Dohn, T. B. van Driel, K. S. Kjær, H. T. Lemke, S. E. Canton, J. Uhlig, V. Sundström, L. Young, S. H. Southworth, M. M. Nielsen, and C. Bressler, J. Phys. Chem. A **116**, 9878 (2012).

[31] See Supplemental Material at http://link.aps.org/supplemental/10.1103/PhysRevLett.117.013002, which includes Refs. [31–41], for full description of the fit procedure, a further analysis and discussion of the solvent and structural contribution to the difference scattering signal as a function of laser power and an extended description of the dynamics observed in the data, including movies S1 and S2 showing the identified vibrational modes. Details of the IRF-determination and MD simulations are also included.

[32] J. Als-Nielsen and D. McMorrow, *Elements of Modern X-ray Physics* (John Wiley & Sons, New York, 2011), p. 1.

[33] S. Palese, L. Schilling, R. J. D. Miller, P. R. Staver, and W. T. Lotshaw, J. Phys. Chem. **98**, 6308 (1994).

[34] H. W. Horn, W. C. Swope, J. W. Pitera, J. D. Madura, T. J. Dick, G. L. Hura, and T. Head-Gordon, J. Chem. Phys. **120**, 9665 (2004).

[35] W. L. Jorgensen, D. S. Maxwell, and J. Tirado-Rives, J. Am. Chem. Soc. **118**, 11225 (1996).

[36] G. J. Martyna, M. L. Klein, and M. Tuckerman, J. Chem. Phys. **97**, 2635 (1992).

[37] J. Neuefeind, C. J. Benmore, J. K. R. Weber, and D. Paschek, Mol. Phys. **109**, 279 (2011).

[38] F. Neese, Max-Planck-Institut für Chemische Energiekonversion, ORCA version 3.0.3, https://orcaforum.cec.mpg.de/.

[39] F. Neese, WIREs Comput. Mol. Sci. **2**, 73 (2012).

[40] A. D. Becke, Phys. Rev. A **38**, 3098 (1988).

[41] J. P. Perdew, Phys. Rev. B **33**, 8822 (1986).

[42] R. A. Binstead and J. K. Beattie, Inorg. Chem. **25**, 1481 (1986).

[43] A. Dohn, E. Biasin, K. Haldrup, M. M. Nielsen, N. E. Henriksen, and K. B. Møller, J. Phys. B **48**, 244010 (2015).

[44] M. Cammarata, M. Lorenc, T. Kim, J. Lee, Q. Kong, E. Pontecorvo, M. L. Russo, G. Schiro, A. Cupane, M. Wulff *et al.*, J. Chem. Phys. **124**, 124504 (2006).

[45] K. S. Kjaer, T. B. van Driel, J. Kehres, K. Haldrup, D. Khakhulin, K. Bechgaard, M. Cammarata, M. Wulff, T. J. Sørensen, and M. M. Nielsen, Phys. Chem. Chem. Phys. **15**, 15003 (2013).

[46] T. J. Sørensen and K. S. Kjær, https://sites.google.com/site/trwaxs/ (2013).

[47] S. Jun, J. H. Lee, J. Kim, J. Kim, K. H. Kim, Q. Kong, T. K. Kim, M. Lo Russo, M. Wulff, and H. Ihee, Phys. Chem. Chem. Phys. **12**, 11536 (2010).

[48] G. Auböck and M. Chergui, Nat. Chem. **7**, 629 (2015).

[49] C. Consani, M. Prémont-Schwarz, A. ElNahhas, C. Bressler, F. van Mourik, A. Cannizzo, and M. Chergui, Angew. Chem. **121**, 7320 (2009).

[50] G. Vankó *et al.*, J. Phys. Chem. C **119**, 5888 (2015).

[51] X. Zhang, M. L. Lawson Daku, J. Zhang, K. Suarez-Alcantara, G. Jennings, C. A. Kurtz, and S. E. Canton, J. Phys. Chem. C **119**, 3312 (2015).

[52] A. O. Dohn, E. Örn Jónsson, K. S. Kjær, T. B. van Driel, M. M. Nielsen, K. W. Jacobsen, N. E. Henriksen, and K. B. Møller, J. Phys. Chem. Lett. **5**, 2414 (2014).

Supplemental Material for: Femtosecond X-ray scattering study of ultrafast photoinduced structural dynamics in solvated $[Co(terpy)_2]^{2+}$

Elisa Biasin,[1] Tim Brandt van Driel,[1] Kasper S. Kjær,[1,2,3] Asmus O. Dohn,[4] Morten Christensen,[1] Tobias Harlang,[2] Pavel Chabera,[2] Yizhu Liu,[2,5] Jens Uhlig,[2] Mátyás Pápai,[4,6] Zoltán Németh,[6] Robert Hartsock,[3] Winnie Liang,[3] Jianxin Zhang,[7] Roberto Alonso-Mori,[8] Matthieu Chollet,[8] James M. Glownia,[8] Silke Nelson,[8] Dimosthenis Sokaras,[8] Tadesse A. Assefa,[9] Alexander Britz,[9] Andreas Galler,[9] Wojciech Gawelda,[9,10] Christian Bressler,[9] Kelly J. Gaffney,[3] Henrik T. Lemke,[8,11] Klaus B. Møller,[4] Martin M. Nielsen,[1] Villy Sundström,[2] György Vankó,[6] Kenneth Wärnmark,[5] Sophie E. Canton,[12,13] and Kristoffer Haldrup[1]

[1] *Technical University of Denmark, Department of Physics, Fysikvej 307, DK-2800 Kongens Lyngby, Denmark.*

[2] *Department of Chemical Physics, Lund University, Box 118, S-22100 Lund, Sweden.*

[3] *PULSE Institute, SLAC National Accelerator Laboratory, Menlo Park, CA 94025, USA.*

[4] *Technical University of Denmark, Department of Chemistry, Kemitorvet 207, DK-2800 Kongens Lyngby, Denmark.*

[5] *Centre for Analysis and Synthesis, Department of Chemistry, Lund University, Box 124, Lund SE-22100, Sweden.*

[6] *Wigner Research Centre for Physics, Hungarian Academy Sciences, H-1525 Budapest, Hungary.*

[7] *School of Environmental and Chemical Engineering, Tianjin Polytechnic University, Tianjin 300387, China*

[8] *LCLS, SLAC National Accelerator Laboratory, Menlo Park, CA 94025, USA.*

[9] *European XFEL GmbH, Albert-Einstein-Ring 19, D-22761 Hamburg, Germany.*

[10] *Institute of Physics, Jan Kochanowski University, 25-406 Kielce, Poland.*

[11] *SwissFEL, Paul Scherrer Institut, 5232 Villigen PSI, Switzerland.*

[12] *IFG Structural Dynamics of (Bio)chemical Systems, Max Planck Institute for Biophysical Chemistry, Am Fassberg 11, D-37077 Goettingen, Germany*

[13] *FS-SCS, Structural Dynamics with Ultra-short Pulsed X-rays,*
Deutsches Elektronen-Synchrotron (DESY),
Notkestrasse 85, D-22607 Hamburg, Germany

CONTENTS

I. MODEL AND FIT OF THE DATA

As described in the article, the measured difference scattering signal is modelled as

$$\Delta S_{model}(Q,\, t) = \alpha(t)\Delta S_{str.}(Q,\, t) + \Delta S_{solvent}(Q,t) \tag{S1}$$

where $\Delta S_{str.}(Q,\, t) = \Delta S_{solute}(Q,\, t) + \Delta S_{cage}(Q)$, arising from the structural response of the system, and $\Delta S_{solvent}(Q,t) = \Delta T(t)\frac{\partial S(Q)}{\partial T}\Big|_{\rho} + \Delta\rho(t)\frac{\partial S(Q)}{\partial \rho}\Big|_{T}$, describing the changes in X-ray scattering arising from the temperature increase and the density changes of the bulk solvent. In this expression, α represents the excitation fraction and ΔT and $\Delta\rho$ the increase in solvent temperature and density, respectively.

A. Bulk solvent contributions

Fig.S1(a) shows the solvent contributions to the difference scattering signal: $\left.\frac{\partial S(Q)}{\partial T}\right|_{\rho}$ and $\left.\frac{\partial S(Q)}{\partial \rho}\right|_{T}$ from [1, 2]. Fig. S1(b) shows ΔT and $\Delta\rho$ obtained as a function of time when using the expression in Eq. S1 to fit the experimental data presented in the article (Fig.2 (a)). We note that the solvent contribution to the recorded difference scattering signal is completely dominated by the change in scattering arising from the temperature increase, while the contribution from density changes is found to be negligible (less then 0.025 kg·m^{-3}). Therefore, only the former was used in the analysis (Eq.6).

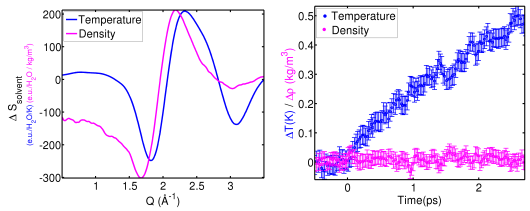

Figure S1. **a:** Measured solvent differentials for water describing the change in difference scattering signal arising from change in temperature (blue) and density (magenta), from [2]. **b:** Fit results for ΔT and $\Delta\rho$ obtained when fitting Eq. S1 to the experimental data in Fig.2(a).

B. Structure and excitation fraction

The scattering signal from the solute molecule (Eq.3) is calculated through the Debye equation:

$$S(Q) = \sum_{i}^{N} |f_i(Q)|^2 + 2\sum_{i<j}^{N} f_i(Q) f_j(Q) \frac{\sin(Q r_{ij})}{Q r_{ij}} \tag{S2}$$

where N is the number of atoms in the molecule, $f_i(Q)$ the atomic form factor for atom i and r_{ij} describe the inter-atomic distances [3].

As discussed in our previous work [4], a strong correlation is often found between the excitation fraction and the magnitude of the structural changes when expressions such as Eq. S1 are used to fit the acquired difference signals. In the present analysis, the simultaneous

determination of both the excitation fraction α and the structural parameter $d_{Co\text{-}N}$ in Eq.6 is significantly improved by assuming the temporal profile of α (Eq.7) and simultaneously optimizing the excited-state molecular structure in a 'global' framework that includes all time delays in the structural analysis [5].

With respect to Eq.7 in the main text, the full expression used to describe the temporal evolution of the the excitation fraction is:

$$\alpha(t) = \int_{-\infty}^{+\infty} \frac{1}{\sigma_{IRF}\sqrt{2\pi}} e^{\frac{-(t-y)^2}{2\sigma_{IRF}^2}} H(y - t_0) A e^{-\frac{y-t_0}{\tau}} dy \tag{S3}$$

where σ_{IRF} is the width of the Gaussian IRF, A and τ are the amplitude and the lifetime of the exponential function, describing respectively the initial amplitude (excitation fraction) and subsequent decay of the bond-elongated excited state, t_0 is the starting point of the exponential decay and y is the integration variable.

Fig.3 of the main article shows the changes in the axial Co-N distance after photoexcitation. The time evolution of this parameter is well described by two oscillations superimposed on an exponential decay, all convoluted with the Gaussian IRF of width σ_{IRF}:

$$\begin{aligned}\Delta d_{Co\text{-}Naxial}(t) = IRF(\sigma_{IRF}, t) \otimes [&E e^{-\frac{t-t_0}{\tau_R}} + B_1 e^{-\frac{t-t_0}{\tau_O}} \cos(\frac{2\pi(t-t_0)}{T_1} + f_1) + \\ &+ (1 - e^{-\frac{t-t_0}{\tau_O}}) B_2 \cos(\frac{2\pi(t-t_0)}{T_2} + f_2)] \cdot H(t - t_0) \\ = \int_{t_0}^{+\infty} \frac{1}{\sigma_{IRF}\sqrt{2\pi}} e^{-\frac{(t-y)^2}{2\sigma_{IRF}^2}} &[E e^{-\frac{y-t_0}{\tau_R}} + B_1 e^{-\frac{y-t_0}{\tau_O}} \cos(\frac{2\pi(y-t_0)}{T_1} + f_1) + \\ &+ (1 - e^{-\frac{y-t_0}{\tau_O}}) B_2 \cos(\frac{2\pi(y-t_0)}{T_2} + f_2)] dy\end{aligned} \tag{S4}$$

where E and τ_R are the amplitude and the lifetime of the exponential decay, B_1, T_1 and f_1 are, respectively, the amplitude, the period and the phase of the first oscillation, and B_2, T_2 and f_2 are, respectively, the amplitude, the period and the phase of the second oscillation. τ_O is the dampening time of the first oscillation as well as the grow-in time of the second one, and y is the integration variable. The best-fit parameters obtained by fitting this expression to $\Delta d_{Co\text{-}Naxial}$ are reported in Table S1. The (adjusted) R^2 is found 0.88. We note that E describes the difference between $d_{Co\text{-}Naxial}$ of the bond-elongated excited state at time zero and the average value of the same quantity after 2 ps. This latter value for $d_{Co\text{-}Naxial}$ is interpreted as the axial Co-N bond length of the HS structure and used in the fit of the long time range dataset (Section V).

σ_{IRF} (ps)	0.05 (fixed)
t_0 (ps)	-0.01 (fixed)
E (Å)	0.014 ± 0.002
τ_R (ps)	0.7 ± 0.1
B (Å)	0.03 ± 0.01
τ_O (ps)	0.4 ± 0.1
T (ps)	0.33 ± 0.03
f (a.u)	- 4.4 ± 0.4
B_2 (Å)	0.002 ± 0.003
T_2 (ps)	0.23 ± 0.01
f_2 (a.u)	0.7 ± 0.7

Table S1. Fit results (95 % confidence bounds) after fitting the expression in Eq. S4 to $\Delta d_{\text{Co-Naxial}}(t)$ (Fig.3).

C. Bulk solvent kinetics

Fig. S2 shows the temporal evolution of $\Delta T(t)$ (black points). The data are described through the expression:

$$\Delta T(t) = \mathrm{IRF}(\sigma_{\mathrm{IRF}}, t) \otimes H(t - t_0) \sum_{j=1}^{N} \gamma_j (1 - e^{-\frac{t-t_0}{\tau_j}}) \tag{S5}$$

$$= \int_{t_0}^{+\infty} \frac{1}{\sigma_{\mathrm{IRF}}\sqrt{2\pi}} e^{-\frac{(t-y)^2}{2\sigma_{\mathrm{IRF}}^2}} \sum_{j=1}^{N} \gamma_j (1 - e^{-\frac{y-t_0}{\tau_j}}) dy$$

where σ_{IRF} is the width of the Gaussian IRF, γ and τ are the amplitude and the lifetime of the N exponential functions and H is the Heaviside step function centered at t_0. Fig. S2 shows a comparison between using a single (N=1) or a double (N=2) exponential function to describe the short time range dataset and we find that the latter better describes the time evolution of ΔT in the first hundreds of femtoseconds. A single exponential grow-in is used to fit the long time range measurements (see Fig. S8). The parameters obtained for both datasets are reported in Tab. S2.

	short time range	long time range
σ_{IRF} (ps)	0.05 (fixed)	0.05 (fixed)
t_0 (ps)	-0.01 (fixed)	-0.01 (fixed)
γ_1 (K)	0.05 ± 0.2	/
τ_1 (ps)	0.01 ± 0.9	/
γ_2 (K)	0.8 ± 0.3	0.84 ± 0.02
τ_2 (ps)	3.5 ± 0.8	4.0 ± 0.6

Table S2. Fit results (95 % confidence bounds) after fitting the expression in Eq. S5 to ΔT(t) both in the short (Fig.S2) and the long (Fig. S8(b)) time range.

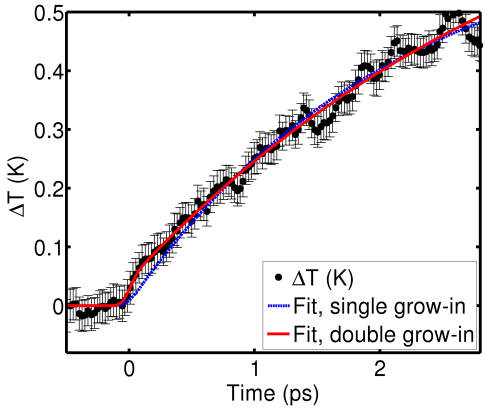

Figure S2. Time evolution of the temperature increase ΔT of the bulk-solvent modelled as a single (dashed blue) or a double (red) exponential grow-in (Eq. S5).

D. Error estimates

As utilized in our previous analysis of XDS data and described in detail in [4], the difference signal ΔS is known to be varying only slowly as a function of Q. We estimate the noise for each ΔS(Q,t) point from the high frequency fluctuations present in an interval around that point. Specifically, for every data point Q_p in the Q-range (with a total number

of $N = 500$ points), we fit a third-order polynomial to ΔS in a 50-point Q-interval around Q_p and estimate the noise σ at Q_p as the standard deviation of the residuals between data and polynomial fit in this interval.

The 'global' fitting procedure was implemented in Matlab®, utilizing constrained minimization of the standard χ^2 estimator:

$$\chi^2(\alpha, d_{\text{Co-Naxial}}, \Delta T) = \Big(\sum_{p=1}^{N} \frac{(\Delta S(Q_p)_{\text{model}} - \Delta S(Q_p)_{\text{meas.}})^2}{\sigma(Q_p)^2} \Big) \cdot \frac{1}{N - P - 1}. \qquad \text{(S6)}$$

where P is the number of free parameters.

The uncertainty estimates for $d_{\text{Co-Naxial}}$ and ΔT for each time point were calculated from the Hessian matrix returned by Matlab®. In the representation shown in Fig. 3 of the main article, $d_{\text{Co-Naxial}}$ was smoothed by a 4-point nearest neighbour filter (∼100 fs), reducing the estimated uncertainty on each point by a factor of two. The uncertainty on the initial excitation fraction A in Eq.7 was estimated as follows. A was allowed to range freely with the remaining fit parameters locked to their best-fit value, thus producing a 2D $\Delta S_{\text{model}}(Q,t)$ matrix for each value of the free parameter from which an average χ^2 could be computed by direct comparison with the measured data set through Eq. S6. These $\chi^2(A)$ curves were converted to a (relative) likelihood distribution $L(A)$ through $L = exp(-\chi^2/2)$ [5]. $L(A)$ was subsequently fitted with a Gaussian, and the error estimated as the σ of this Gaussian function [4].

II. ANISOTROPIC SIGNAL $\Delta S_{\text{ani.}}(Q,T)$ AND ESTIMATE OF σ_{IRF}

Fig. S3(a) shows the anisotropic contribution ($\Delta S_{\text{ani.}}$) to the total difference scattering signal, with the isotropic part (ΔS) shown in Fig. 2 and analysed in the main text. The two contributions were extracted from the 2D difference scattering patterns as detailed in [6]. As the excitation of the solute molecules have very little or no polarization dependence, the anisotropic component of the difference scattering signal arises from the almost instantaneous transient response of the water molecules to the electric field of the laser pulse (Kerr effect). The very fast nature of this response [7] allows us to use it to estimate the time resolution of the experiment. The response is found to be well described by the convolution of an exponential decay with a Gaussian IRF, and by fitting this model to the data we find σ_{IRF} = 0.05 ± 0.03 ps and t_0 = -0.01 ± 0.03 ps (see Fig. S3(b)). These values are assumed to

describe the IRF for the experiments presented in this work, and were kept fixed throughout the analysis described in the main text.

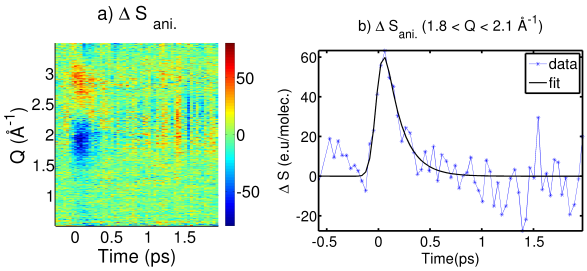

Figure S3. **a:** Anisotropic difference scattering signal $\Delta S_{ani.}(Q,t)$. **b:** Averaged value of $\Delta S_{ani.}$ in the interval 1.8 Å < Q < 2.1 Å, where the scattering signature of the transient alignment of water molecules with the polarized laser pulse appears is most dominant. The expression in Eq. S3 is used for the fit.

III. SVD ANALYSIS

Fig. S4(a) shows the difference scattering signal $\Delta S_{Solv\text{-}subtr.}$ obtained after subtracting the (fitted, see above and main text for details) solvent contribution from ΔS (Q,t) (Fig.2). It is dominated by the negative feature at low-Q, signature of the expansion of the Co-N bonds. Fig. S4(b, c and d) show the main results of a Singular Value Decomposition (SVD) of this signal. As indicated by the relative magnitude of the singular values shown in Fig. S4(b), a single component dominates the signal. This component and its amplitude as a function of time are shown in Fig. S4(c) and Fig. S4(d), respectively.

With respect to the latter, the time evolution arises from both the structural dynamics and the kinetics of the bond-elongated state. Fig.S5 shows that, up to 0.5 ps, this time evolution is well-described by a grow-in exponential function followed by an oscillation, all broadened by the IRF:

$$V_1^{\text{model}}(t) = \text{IRF}(\sigma_{\text{IRF}}, t) \otimes [R(1 - e^{-\frac{t-t_0}{\tau_G}}) + O\cos(\frac{2\pi(t-t_0)}{T} + f)] \cdot H(t-t_0) \qquad \text{(S7)}$$

$$= \int_{t_0}^{+\infty} \frac{1}{\sigma_{\text{IRF}}\sqrt{2\pi}} e^{-\frac{(t-y)^2}{2\sigma_{\text{IRF}}^2}} [R(1 - e^{-\frac{y-t_0}{\tau_G}}) + O\cos(\frac{2\pi(y-t_0)}{T} + f)]dy$$

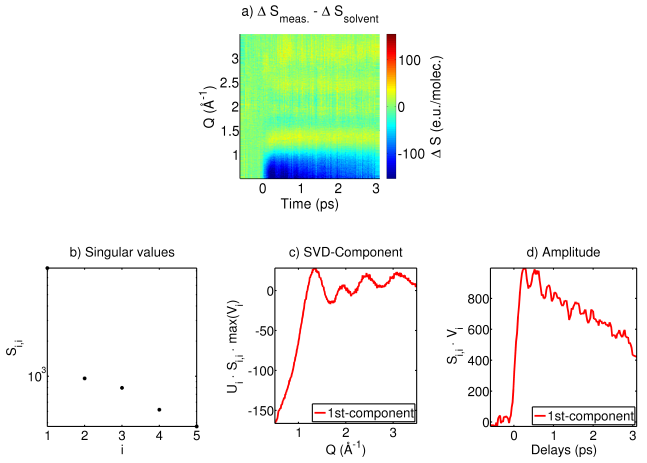

Figure S4. **a:** $\Delta S_{\text{Solv-subtr.}}$: difference scattering signal obtained by subtracting $\Delta S_{\text{solvent}}$ from the experimental data. **b-d:** Results of a SVD analysis of the data in **a**. $\Delta S_{\text{Solv-subtr.}} = U \cdot S \cdot V^{T}$. **b:** The singular values of the diagonal $S_{i,i}$. **c:** Q-profile of the first component ($U_1 \cdot S_{1,1} \cdot max(V_1)$). **d:** Temporal evolution of the first component ($S_{1,1} \cdot V_1$), smoothed by a 3-point nearest neighbour filter (∼75 fs).

where R and τ_G are the amplitude and the lifetime of the exponential, and O, T and f the amplitude, the period and the phase of the oscillation, respectively, and y is the integration variable. The values of both the fixed variables and the obtained parameters are reported in Tab. S3. The rise time of the structural signal is found to be 0.06 ps ± 0.01 ps and the phase shift of the oscillation, which has a period of ∼0.33 ps, is found to be 0.08 ps ± 0.02 ps. This is interpreted as an indication of the presence of one (or more) intermediate state(s) before the (electronic) population of the bond-elongated state, as further discussed in the main text.

σ_{IRF} (ps)	0.05 (fixed)
t_0 (ps)	-0.01 (fixed)
R (a.u.)	0.91 ± 0.03
τ_G (ps)	0.06 ± 0.01
O (a.u.)	0.09 ± 0.06
T (ps)	0.33 (fixed)
f (a.u.)	1.5 ± 0.4

Table S3. Fit results (95 % confidence bounds) after fitting the expression in Eq. S7 to the (normalized) amplitude of the first component after a SVD of $\Delta S_{\text{Solv-subtr.}}$ (Fig. S5).

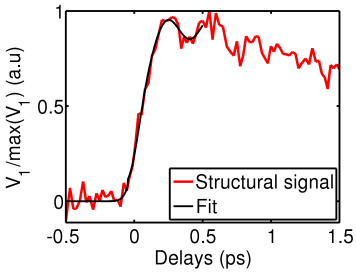

Figure S5. Temporal evolution of the (normalized) amplitude of the first component obtained from a SVD analysis of $\Delta S_{\text{Solv-subtr.}}$ (Fig. S4). We interpret this as the signal arising from primarily the change in the structure of the solute. The black line represents a fit to the data, utilizing a IRF-broadened exponential grow-in function with lifetime of 0.06 ps ± 0.01 ps followed by an oscillation of 0.33 ps period and with a 0.08 ps ± 0.02 ps phase shift.

IV. FOURIER TRANSFORM OF THE OSCILLATORY STRUCTURAL SIGNAL

Fig.S6(a) shows the temporal evolution of the structural contribution (red line) to the measured ΔS (see Fig. S4). This temporal evolution is described by a broadened exponential decay (black line). The residuals (blue line) between the data and the fit are here referred to as the oscillatory structural signal (OSS). Fig.S6(b) shows the Fourier Transform of the OSS for t > 0.3 ps: two main peaks are found at ∼0.23 ps and ∼0.34 ps. The inset of Fig.3

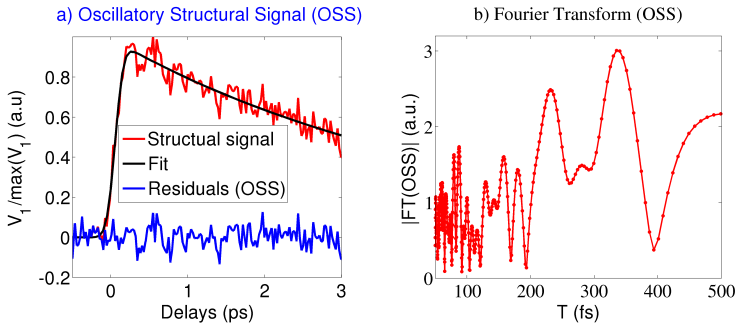

Figure S6. **a:** Amplitude of the first SVD component of $\Delta S_{Solv-subtr}$ (see Fig. S4) as a function of time (red). This represents the time evolution of the structural signal. An exponential decay broadened by a Gaussian function (black) is fitted to the data. Difference (blue) between the structural signal and the exponential fit. We refer to this as the oscillatory structural signal (OSS). **b:** Fourier Transform (FT) of the OSS for t > 0.3 ps, with the two main peaks at 220 fs and 340 fs.

in the main article shows the time dependent FT of the OSS obtained by sliding a 2 ps Hann window starting from a central value of 0.6 ps up to a central value of 2 ps.

V. LONG TIME RANGE MEASUREMENTS

Fig. S7(a) shows the isotropic difference scattering signals ΔS(Q, t) measured for time delays up to 20 ps. This dataset was binned in ∼300 fs bins, with 400 images in each bin. The following model was used to fit the data at each time delay:

$$\Delta S_{\mathrm{model}}(Q,\,t) = \alpha(t)\Delta S_{\mathrm{str.}}(Q) + \Delta T(t)\frac{\partial S(Q)}{\partial T}\bigg|_{\rho} \tag{S8}$$

with α and ΔT as free parameters and $\Delta S_{\mathrm{struc.}}$ calculated from the structure of $[Co(terpy)_2]^{2+}$ 2 ps after the photoexcitation (as obtained from the analysis of the short time range dataset). This model can describe the data at all time delays, as indicated by the low residuals in Fig. S7(b). The time evolution of the kinetic parameters, α and ΔT are reported in Fig. S8. A single exponential decay is used to fit the excitation fraction α after 2 ps (i.e. after the excited-state structure has relaxed), and a lifetime of 6.8 ps ± 0.8 ps is found. The

temporal evolution of the temperature increase is well-described by a single exponential grow-in function (Eq. S5) and the obtained parameters are reported in Tab. S2.

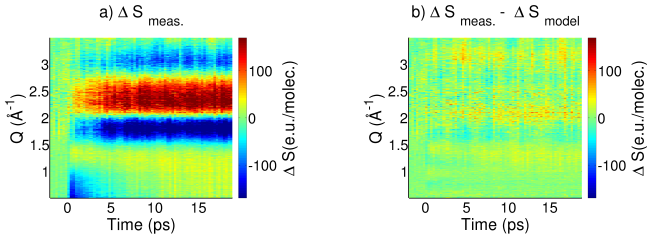

Figure S7. **a:** Measured difference scattering signal ($\Delta S_{meas.}(Q, t)$) of photoexcited $[Co(terpy)_2]^{2+}$ in aqueous solution (long time range dataset). **b:** Residuals obtained by subtracting the model (Eq. S8) from the experimental data.

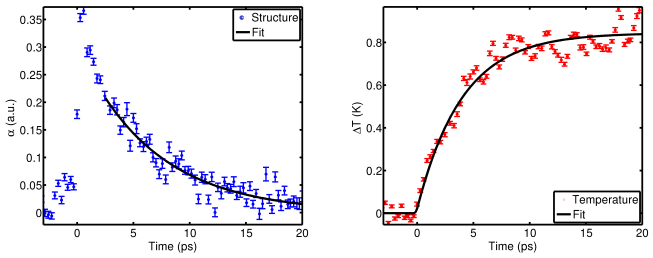

Figure S8. Kinetics obtained from the fit of the long time range dataset. **a:** Evolution of α, the magnitude of the structural component observed in the difference scattering signal (blue points). After 2 ps, it is well-described by an exponential decay with lifetime of 6.8 ps ± 0.8 ps (black line), interpreted as the lifetime of the bond-elongated HS excited state. **b:** Time evolution of the temperature increase ΔT of the solvent (red points). The temperature increase is well described by an exponential grow-in with a time constant of 4.0 ps ± 0.6 ps (Eq. S5).

VI. MD SIMULATIONS AND RDF ANALYSIS

The LS and HS structures of $[Co(terpy)_2]^{2+}$ were solvated in a cubic box (50 Å size) of water molecules using the TIP4P-Ew potential [8]. The bond lengths of the solute molecule were constrained and MD trajectories were calculated with OPLS2005 force field parameters [9] and a Nose-Hoover thermostat at 300 K [10]. The Radial Distribution Functions (RDFs) of the solute-solvent atom pairs were sampled in 0.1 Å radial bins and over 2000 individual simulation time steps over a total time interval of 2 ns. Fig. S9 shows the radial distribution functions (RDFs) g(r) of the oxygen (O) and hydrogen (H) atoms with respect to the Co atom, r being the distance from the Co, and the coordination number cn(r), the number of oxygens/hydrogens contained in a sphere of radius r, for both the LS and HS states of solvated $[Co(terpy)_2]^{2+}$. The first peak in the RDFs represents the first solvation shell. By inspection of $g_{CoO}(r)$ in Fig. S9(a), we note that the first peak slightly shifts (∼0.1 Å) towards smaller r values, decreases in amplitude and broadens upon the LS → HS spin transition on the Co centre. Considering the first minimum in the RDFs to be the limit of the first solvation shell, in the LS state it is found at 5.9 Å and, at this value, cn(r) is found to be ∼12 for both spin states. Similar considerations for $g_{CoH}(r)$ are shown in Fig. S9(b). This observation indicates that, upon the expansion of the Co-N bonds, the water molecules on average come closer (∼ 0.1 Å) to the Co-center but their total number in the first solvation shell remains constant. Finally, Fig. S9(c) shows that, relative to the H, the O come slightly closer to the positive Co centre in the HS spin with respect to the LS spin, representing a general rotation of the water molecules upon the spin transition.

VII. ENERGETICS

The laser pump energy absorbed by the solute molecules and the subsequent temperature increase of the solvent due to non-radiative relaxation of the solute can be estimated from experimental parameters, as detailed in [1]. Given a square X-ray spot size of $d_{X\text{-ray}} = 50\ \mu$m, a path length (through the 45 ° tilted liquid sheet) of $l = 140\ \mu$m and a sample concentration of $c = 20$mM, the number of molecules N_V in the probed volume can be calculated as:

$$N_V = c \cdot N_A \cdot d_{X\text{-ray}}^2 \cdot l = 4.2 \cdot 10^{12}$$

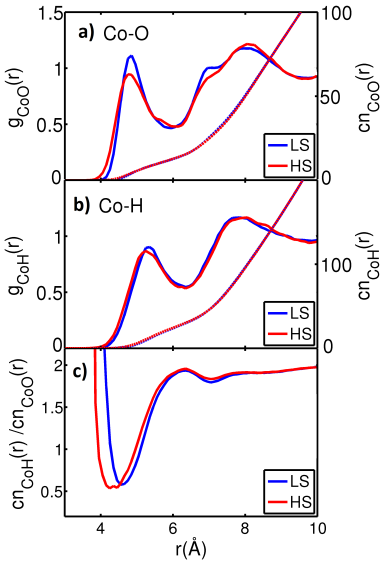

Figure S9. **a-b:** LS and HS RDFs g(r) of the water oxygen (**a**) and hydrogen (**b**) atoms with respect to the Co atom (solid line, left y-axis) and coordination number cn(r) (dashed lines, right y-axis) **c:** ratio of the Co-H to the Co-O coordination number in the LS and HS state, describing the orientation of the water molecules with respect to the Co center.

where N_A is Avogadro's number. Given an excitation fraction of 34 %, as found in our analysis, the number of excited molecule is then:

$$N_{\text{exc.}} = 0.34 \cdot N_V = 1.4 \cdot 10^{12}.$$

By assuming a linear regime such that each of these molecules absorbed one 530 nm photon (2.3 eV per photon), the energy per unit volume released to the solvent after non-radiative decay of the solute species would be:

$$E_{\text{dep.}} = \frac{N_{\text{exc.}} \cdot 2.3 \text{ eV}}{(50 \text{ cm})^2 \cdot l} = 1.5 \text{ J/cm}^3.$$

The specific heat capacity of water is $C_p = 4.18$ J$\cdot$ cm^{-3} $\cdot$ K^{-1} and the average temperature change in the volume probed by the X-ray would then be expected to be:

$$\Delta T = \frac{E_{\text{dep.}}}{C_p} = 0.38 \text{ K}$$

which is lower than the 0.84 K found from the analysis of the experimental dataset (Tab. S2). This we interpret as an indication that multi-photon excitation of the sample (solute and solvent) may be present and should be taken into account in the analysis. That such higher-order processes appear to be active is not surprising, as the excitation laser intensity is quite high. Given a laser pulse length of 70 fs and a laser pulse energy of 70 μJ focused on a spot of diameter of $d = 150$ μm (FHWM), the peak irradiance will be 3.5 TW/cm^2.

In order to further investigate the robustness of the results presented in the main article in the presence of multi-photon absorbtion, a second dataset with significantly lower laser power, 20 μJ (i.e. at a peak irradiance of 1 TW/cm^2), was subjected to the same analysis as that presented in the main text (Eq.5). For this dataset, we find an excitation fraction of 19 % and a 0.2 K temperature increase, as shown in Fig.S10(a). From the same energetics calculations as above, a temperature increase of 0.2 degrees indicates that the 20 μJ data set represents the response in the linear, one-photon excitation regime. Fig.S10(b) shows that the Co-N bond length dynamics results obtained from the analysis of the 20μJ dataset are essentially the same, but with more noise, than those obtained from the 70μJ dataset and presented in the main article.

As discussed in detail in our previously published LCLS studies, the presence of multi-photon excitation can result in very significant local heating of the solvent [11]. This may in turn lead to a breakdown in the assumption that the changes in scattering due to the temperature response of the aqueous solvent can be well described by a single, linearly scaled solvent differential. However, as also described in our recent work [11], the model describing the changes in solvent scattering can be readily extended to include a second-order term $\left.\frac{\partial^2 S\ (Q)}{\partial T^2}\right|_\rho$ which can be obtained from either MD modelling or from experiments [12]. Including this contribution in the full model, we found that it contributed at most 5 % of the measured difference signal and it was found to have no discernible impact on any of the results presented in this work. Including the second order solvent differential in the analysis of the 20 μJ indicated no contribution.

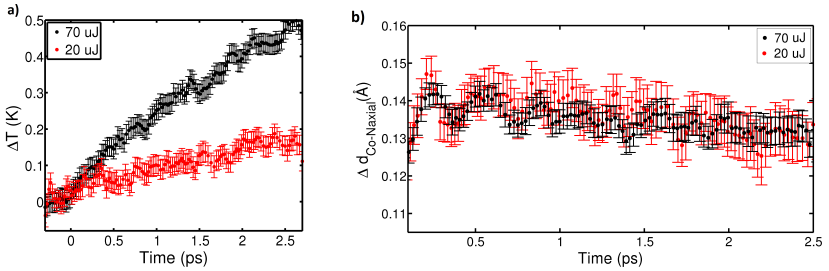

Figure S10. **a:** Time evolution of the temperature increase of the bulk-solvent after photoexcitation of the sample with a 20 μJ (red) or a 70 μJ (black) laser pulse. **b:** Time evolution of the changes in the Co-N bond length distance from the ground to the excited state after after photoexcitation with a 20 μJ (red) or a 70 μJ (black) laser pulse.

VIII. DFT CALCULATIONS

The DFT calculations were carried out with the ORCA program package [13, 14], utilizing the gradient-corrected BP86 exchange correlation functional [15, 16] in combination with the TZVP basis set. Solvent effects were approximated by the application of the conductor-like screening model (COSMO) using the relative permittivity of water ($\varepsilon = 80.4$). Vibrational frequencies were calculated as second derivatives of the electronic energy, and were all found to be positive, confirming that the optimized geometries at the BP86/TZVP level correspond to true minima of the corresponding potential energy surfaces (PES). Movie S1 shows the breathing mode of the HS state of $[Co(terpy)_2]^{2+}$, using the vectors and the frequency (92 cm^{-1}) obtained from DFT calculation. From the same calculation, Movie S2 shows the 'pincer-like' mode found at 146 cm^{-1}.

IX. EXPERIMENTAL SETUP AND DATA REDUCTION

The 20 mM aqueous solution of $Co(terpy)_2Cl_2$ was prepared according to the procedure given in [17]. Fig.S11 shows the absorption spectrum of $[Co(terpy)_2]^{2+}Cl_2$ in water. For the experiment, the solution was pumped through a sapphire nozzle producing a 100 µm flat liquid sheet flowing in the vertical direction and inclined at 45° to the (nearly) collinear

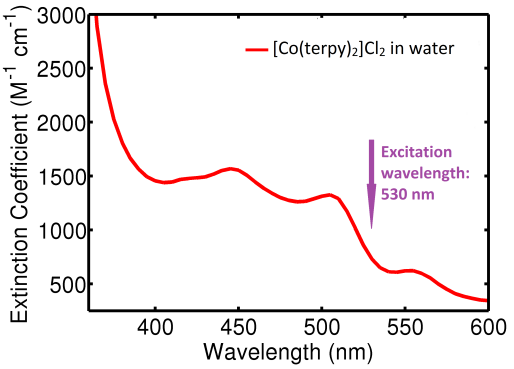

Figure S11. UV-Vis absorption spectrum of $[Co(terpy)_2]^{2+}$ in water.

co-propagating laser and X-ray beams. The flow rate (ca. 1 mm/ms) was sufficient to fully replace the sample between successive X-ray pulses at the 120 Hz repetition rate of the LCLS facility. The laser system produced 70 µJ pulses at 530 nm with 70 fs pulse width (FWHM) and 7.5 nm bandwidth (FWHM). It was focused onto a 150 µm diameter spot (via a CaF_2 lens with 750 mm focal length). The 8.3 keV X-ray probe pulses (with $\sim 10^{12}$ photons/pulse on average) were focused to a (50 µm)^2-size square spot and overlapped with the pump laser at the sample position. The laser excited the sample synchronously for every probing X-ray pulse, except for every 5th pulse, where the laser beam was dropped before the sample position, so that the static structure of the sample with only ground state species present could be repeatedly measured during the sequence of pump-probe XDS measurements. The acquired 2D scattering patterns were corrected for artefacts due to X-ray pulse energy and intensity shot-to-shot jitter following the procedure described by van Driel et al. [18]. The patterns were then corrected for X-ray polarization, solid-angle and absorption through the liquid sheet. The radially integrated scattering signal from each pattern was scaled to the total 1D scattering signal calculated in electron units for a liquid unit cell, which, in the present experiment, consists of one solute molecule, 2777 water molecules and two Cl atoms. The full Q range [0.5 - 3.5] Å^{-1} was used as scaling interval and the so-obtained scaling factor was then used to scale each 2D pattern. Individual 2D difference scattering images were obtained by subtracting the laser-off from the laser-on scattering patterns. In

order to extract the temporal behaviour during a time-delay scan between laser and X-ray pulses, the time-corrected images (using the XPP timing tool [19]) were sorted into ∼23 fs wide bins with 600 difference scattering patterns being averaged in each. 1D isotropic and anisotropic difference scattering signals were extracted from each of these averaged 2D difference patterns. For the set of measurements described here, the relative intensity of the difference signal was on the order of 0.1 % of the total scattering signal.

[1] K. S. Kjaer, T. B. van Driel, J. Kehres, K. Haldrup, D. Khakhulin, K. Bechgaard, M. Cammarata, M. Wulff, T. J. Sørensen, and M. M. Nielsen, Physical Chemistry Chemical Physics **15**, 15003 (2013).

[2] T. J. Sørensen and K. S. Kjær, (2013), https://sites.google.com/site/trwaxs/.

[3] J. Als-Nielsen and D. McMorrow, "X-rays and their interaction with matter," in *Elements of Modern X-ray Physics* (John Wiley and Sons, Inc., 2011) pp. 1–28.

[4] K. Haldrup, M. Christensen, and M. Meedom Nielsen, Acta Crystallographica Section A **66**, 261 (2010).

[5] S. Jun, J. H. Lee, J. Kim, J. Kim, K. H. Kim, Q. Kong, T. K. Kim, M. Lo Russo, M. Wulff, and H. Ihee, Physical Chemistry Chemical Physics **12**, 11536 (2010).

[6] U. Lorenz, K. B. Møller, and N. E. Henriksen, New Journal of Physics **12**, 113022 (2010).

[7] S. Palese, L. Schilling, R. J. D. Miller, P. R. Staver, and W. T. Lotshaw, The Journal of Physical Chemistry **98**, 6308 (1994).

[8] H. W. Horn, W. C. Swope, J. W. Pitera, J. D. Madura, T. J. Dick, G. L. Hura, and T. Head-Gordon, The Journal of Chemical Physics **120**, 9665 (2004).

[9] W. L. Jorgensen et al., Journal of the American Chemical Society **118**, 11225–11236 (1996).

[10] G. J. Martyna, M. L. Klein, and M. Tuckerman, The Journal of Chemical Physics **97**, 2635 (1992).

[11] K. Haldrup, W. Gawelda, R. Abela, R. Alonso-Mori, U. Bergmann, A. Bordage, M. Cammarata, S. Canton, A. Dohn, T. van Driel, D. Fritz, A. Galler, P. Glatzel, T. Harlang, K. Kjær, H. Lemke, K. Moller, Z. Németh, M. Pápai, N. Sas, J. Uhlig, D. Zhu, G. Vankó, V. Sundstrom, M. Nielsen, and C. Bressler, The Journal of Physical Chemistry B **120**, 1158 (2016).

[12] J. Neuefeind, C. J. Benmore, J. K. R. Weber, and D. Paschek, Molecular Physics **109**, 279 (2011).

[13] ORCA version 3.0.3, F. Neese, Max-Planck-Institut für Chemische Energiekonversion, https://orcaforum.cec.mpg.de/.

[14] F. Neese, WIREs Computational Molecular Science **2**, 73 (2012).

[15] A. D. Becke, Physical Review A **38**, 3098 (1988).

[16] J. P. Perdew, Physical Review B **33**, 8822 (1986).

[17] R. A. Binstead and J. K. Beattie, Inorganic Chemistry **25**, 1481 (1986).

[18] T. B. van Driel, K. S. Kjaer, E. Biasin, K. Haldrup, H. T. Lemke, and M. M. Nielsen, Faraday Discussions **177**, 443 (2015).

[19] M. P. Minitti, J. S. Robinson, R. N. Coffee, S. Edstrom, S. Gilevich, J. M. Glownia, E. Granados, P. Hering, M. C. Hoffmann, A. Miahnahri, and et al., Journal of Synchrotron Radiation **22**, 526 (2015).